Doctoral Thesis

Compositional and additive design for efficient and stable perovskite solar cells

Hanul Min

School of Energy and Chemical Engineering

(Energy Engineering)

Ulsan National Institute of Science and Technology

2021

Compositional and additive design for efficient and stable perovskite solar cells

Hanul Min

School of Energy and Chemical Engineering

(Energy Engineering)

Ulsan National Institute of Science and Technology

Compositional and additive design for efficient and stable perovskite solar cells

A thesis/dissertation submitted to
Ulsan National Institute of Science and Technology
in partial fulfillment of the
requirements for the degree of
Doctor of Philosophy

05.10.2021 of submission

Approved by

Advisor
Sang Il Seok

Compositional and additive design for efficient and stable perovskite solar cells

Hanul Min

This certifies that the thesis/dissertation of Hanul Min is approved.

05.10.2021 of submission

Signature

Advisor: Sang Il Seok

Signature

Jin Young Kim: Thesis Committee member #1

Signature

Jun Hee Lee: Thesis Committee member #2

Signature

Sung-Yeon Jang: Thesis Committee member #3

Signature

Kyoung-Jin Choi: Thesis Committee member #4

Abstract

Crystalline silicon solar cells, which are most commonly deployed, have high performance with power conversion efficiency (PCE) of 26.7% in the lab. However, since a large amount of energy is required to manufacture high purity silicon, the price is high, and due to the nature of the material, it is not flexible. As next-generation solar cells to solve these shortcomings, organic and dye-sensitized solar cells have been studied, but it is still difficult to commercialize due to low efficiency. More recently, metal halide perovskite materials (represented by the general chemical formula ABX_3, where A denotes an organic ammonium or inorganic cation such as methylammonium (MA^+), formamidinium (FA^+), or Cs^+; B denotes a metal cation such as Pb^{2+}, or Sn^{2+}; and X denotes a halide (I^-, Br^-, and Cl^-)) have recently emerged as a highly promising class of electrical functional materials. The exceptional structural tunability enables these materials to possess three- (3D), two- (2D), one- (1D), and zero-dimensional (0D) structures at the molecular level. Each category of these materials has its unique physical and chemical properties with a variety of applications such as transistors, light emitting iodides (LEDs), x-ray detector, and solar cells. In particular, perovskite solar cells (PSCs) display unique promise to satisfy low costs, flexibility, and high efficiency. Currently, PSCs have already obtained comparable PCE to silicon in the lab, of 25.5%, with low manufacturing cost compared to silicon solar cells.

During my Ph.D., I focused on improving efficiency and stability of PSCs by designing composition, additive, and device. PSCs are mainly fabricated by solution process so the properties of precursor solution are important as it can greatly affect the resulting device's properties and performance. I identified the cause of the phenomenon that the properties of the halide perovskite precursor solution change over time and minimized the problem by adding a certain amount of elemental sulfur. This work was published in *Advanced Energy Materials* and selected as a cover picture. Subsequently, the research was conducted to improve the efficiency and stability of PSCs. High-performance PSCs exceeding 22% of efficiency are fabricated by using $FAPbI_3$ as a light absorbing layer due to its suitable bandgap and relatively higher thermal stability. However, $FAPbI_3$ readily transforms from the desired trigonal black α-phase into the undesired wide-bandgap δ-phase with hexagonal symmetry under ambient conditions at room temperature. The method mainly used to suppress this drawback was to stabilize the phase of $FAPbI_3$ by adding some amount of $MAPbBr_3$. However, MA is highly volatile and week to heat, and Br cause undesired blue-shift of bandgap. In the point of this view, I successfully conducted research on the introduction of a very new additive (methylenediammonium dichloride, $MDACl_2$) to stabilize the α-phase while minimizing the bandgap variation of $FAPbI_3$. By using this new composition, we achieved world's highest certified current density (J_{SC}) and efficiency based on the date of publication and the results was published in the journal *Science*. Also, I published another *Science* paper that

significantly increase the efficiency and stability of PSCs by reducing lattice strain while maintaining the α-phase of $FAPbI_3$. And I also conducted research on morphology control of all-inorganic perovskite, $CsPbI_3$ which can be used top-cell of tandem device with silicon or narrow-bandgap perovskites and achieved the world's highest efficiency and published in *Joule*.

Currently, research on reducing the external strain of perovskite thin films has been conducted and manuscripts are being prepared. Furthermore, the results of the world's highest efficiency which currently included *National Renewable Energy Laboratory (NREL) chart* are under evaluation in high impact journal.

Contents

List of Figures

Chapter 1

Chapter 2

Chapter 3

Chapter 4

Chapter 5

List of Tables

Chapter 2

Chapter 3

Chapter 1. Introduction

1.1 Needs for solar cells

It is indispensable to develop renewable energy sources for a sustainable future to replace fossil fuels, which are finite and emit greenhouse gases that contribute to climate change. The most abundant source among the renewable energy sources is solar energy **(Fig. 1.1)**. As of 2019, the world's energy consumption is 18 TWy, but the amount of energy from the sun on Earth's surface is 23,000 TWy.[1] Since energy consumption increases every year while fossil fuel reserves decline, it is very important to develop technologies that effectively convert the most abundant solar energy into other forms.

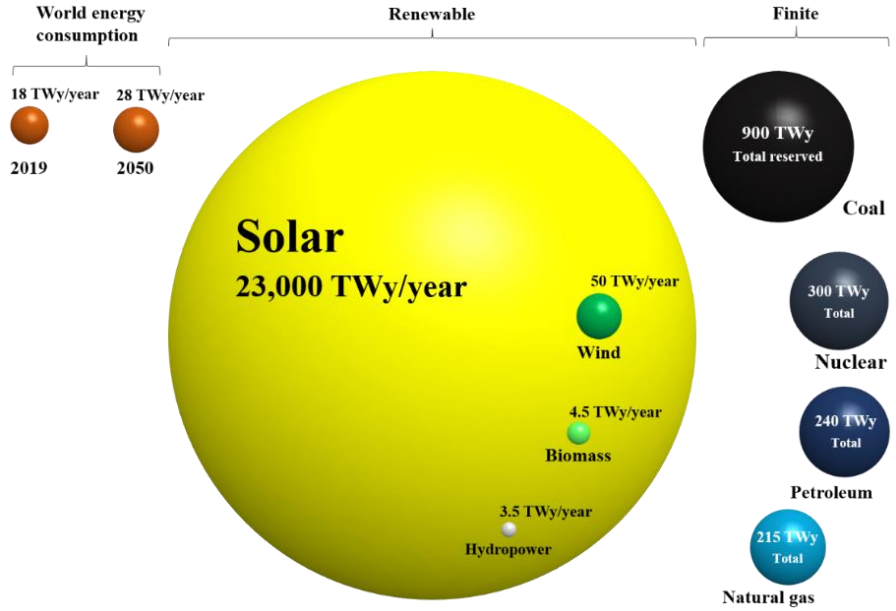

Fig. 1.1 A comparison of annual world energy consumption and renewable energy potential with the total recoverable reserves of finite resources.

As of 2019, the consumption of renewable energy is only 11% of the total energy consumption **(Fig. 1.2A)**.[2] And within that renewable energy portion, only 4% is from solar. Photovoltaics are the most efficient, and the only direct, way to convert solar energy into electricity. Historically, the cost of electricity from solar cells is expensive compared to other options **(Fig. 1.2B)**.[3] Recently, however, with the development of silicon solar cell manufacturing technology and efficiency increases, prices have fallen within the range of other renewable sources. The potential for further reductions is real, and therefore research on emerging solar cells one of the best options to allow photovoltaics to realize an increasing share of the renewable energy (and overall energy) ecosystem.

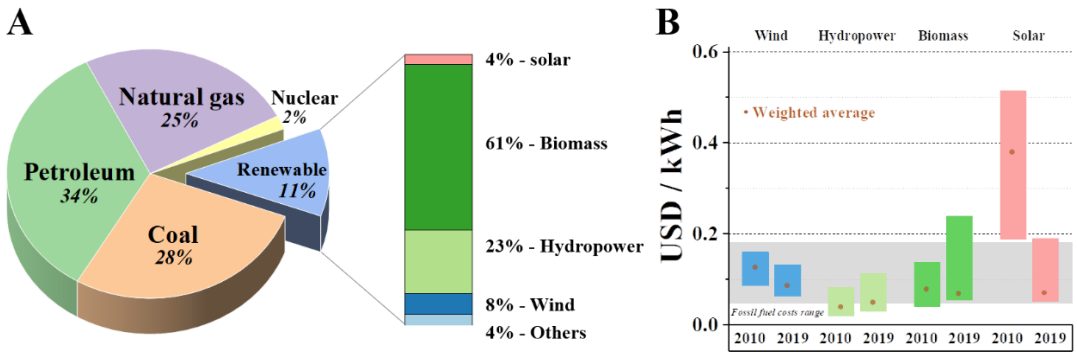

Fig. 1.2 (A) Global energy consumption breakdown, 2019. **(B)** Renewable power generation costs in 2010 and 2019, with the fossil fuel range represented by the grey band.

1.2 Perovskites: Emerging electrical functional materials

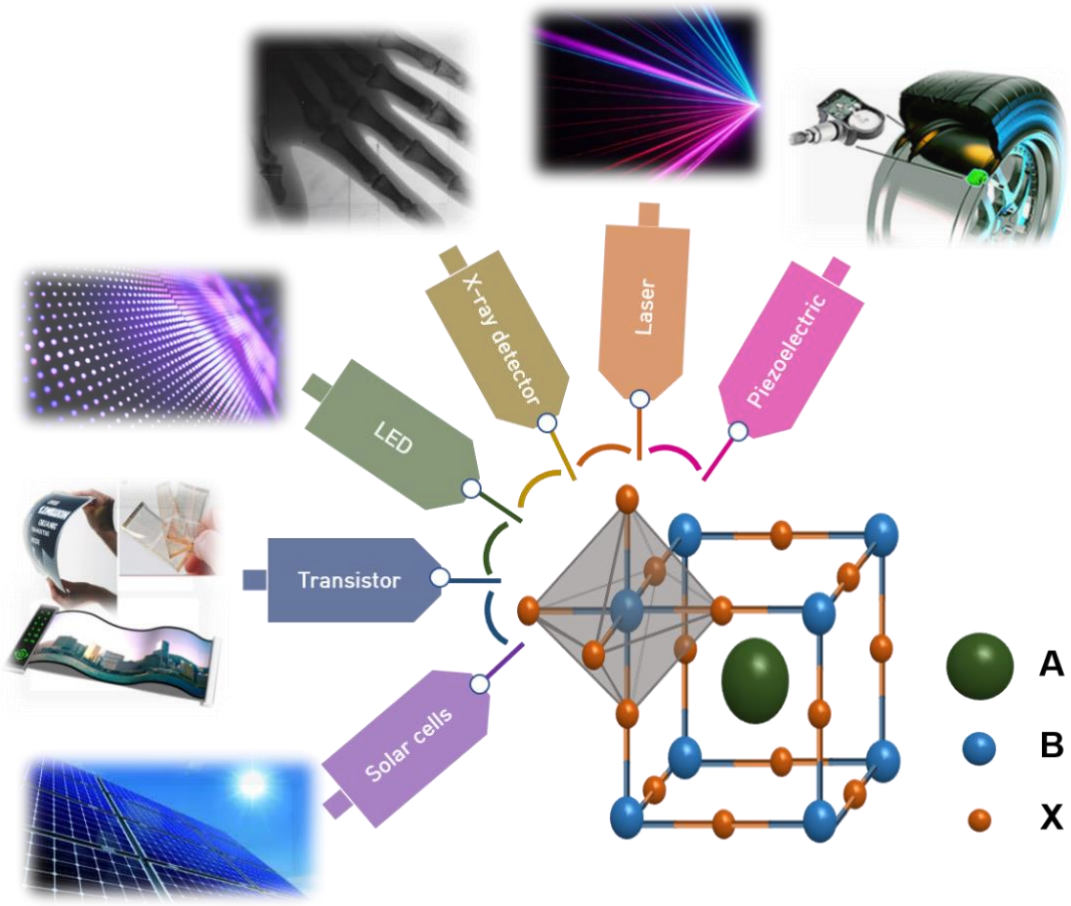

Fig. 1.3 Crystal structure of the perovskites and its various applications.

Inorganic-organic hybrid perovskites (represented by the general chemical formular ABX_3, where A denotes an organic ammonium or inorganic cation such as methylammonium (MA^+), formamidinium (FA^+), or Cs^+; B denotes a metal cation such as Pb^{2+}, or Sn^{2+}; and X denotes a halide (I^-, Br^-, or Cl^-)) have recently emerged as a highly promising class of functional materials. The exceptional structural tunability enables these materials to possess three- (3D), two- (2D), one- (1D), and zero-dimensional (0D) structures at the molecular level. Each category of these materials has its unique physical and chemical properties with a variety of applications such as transistors, light emitting diode (LED), X-ray detector, and solar cells **(Fig. 1.3)**.

1.3 Next-generation perovskite solar cells

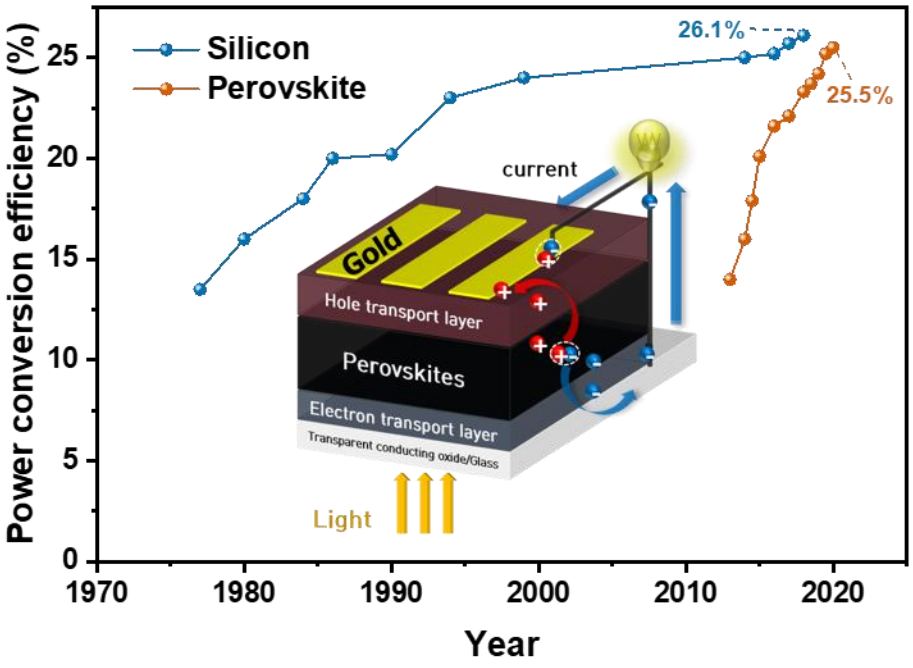

Fig. 1.4 The highest certified efficiency of crystalline silicon solar cells and perovskite solar cells and the device structure (inset) of representative solid state perovskite solar cells.

Crystalline silicon solar cells, which are most commonly deployed, have high performance with power conversion efficiency (PCE) of 26.1% in the lab (deployed modules feature cell PCE of 17-22%).[ref] However, since a large amount of energy is required to manufacture high purity silicon, the price is high, and due to the nature of the material, it is not flexible. As next-generation solar cells to solve these shortcomings, organic and dye-sensitized solar cells have been studied, but it is still difficult to commercialize due to low efficiency. More recently, metal halide perovskite materials display unique promise to satisfy low costs, flexibility, and high efficiency. Currently, perovskite solar cells (PSCs) have already obtained comparable PCE to silicon in the lab, of 25.5%,[4] with low manufacturing cost compared to silicon solar cells **(Fig. 1.4)**.

Chapter 2. Perovskite Precursor Solution

2.1 Solution processibility of perovskite solar cells

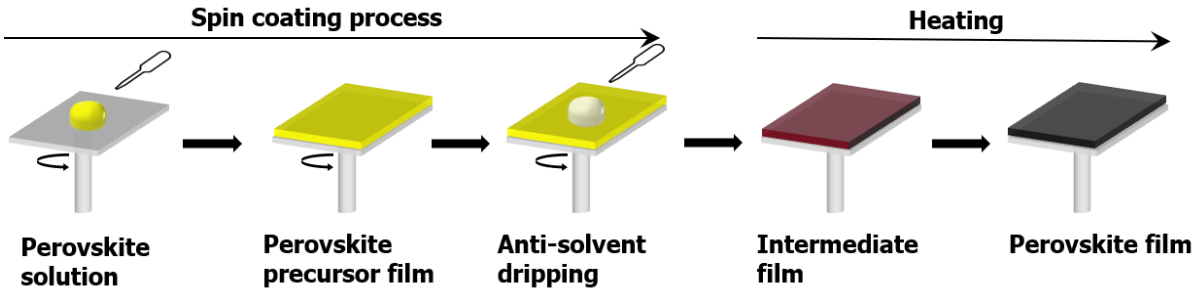

Fig. 2.1 Typical experimental procedure to synthesize perovskites onto thin film.

Solution processes including spin-coating, bar-coating, and printing techniques makes PSCs promising for the next-generation solar cells due to the scalability and compatibility with large-scale manufacturing processes. In particular, efficient PSCs are mainly fabricated by a solution coating processes **(Fig. 2.1)**. However, the efficiency of such devices varies significantly with the aging time of the precursor solution used to fabricate them, which includes a mixture of perovskite components, especially MA, and FA cations.

2.2 Properties of perovskite precursor solution

2.2.1 Iodoplumbates

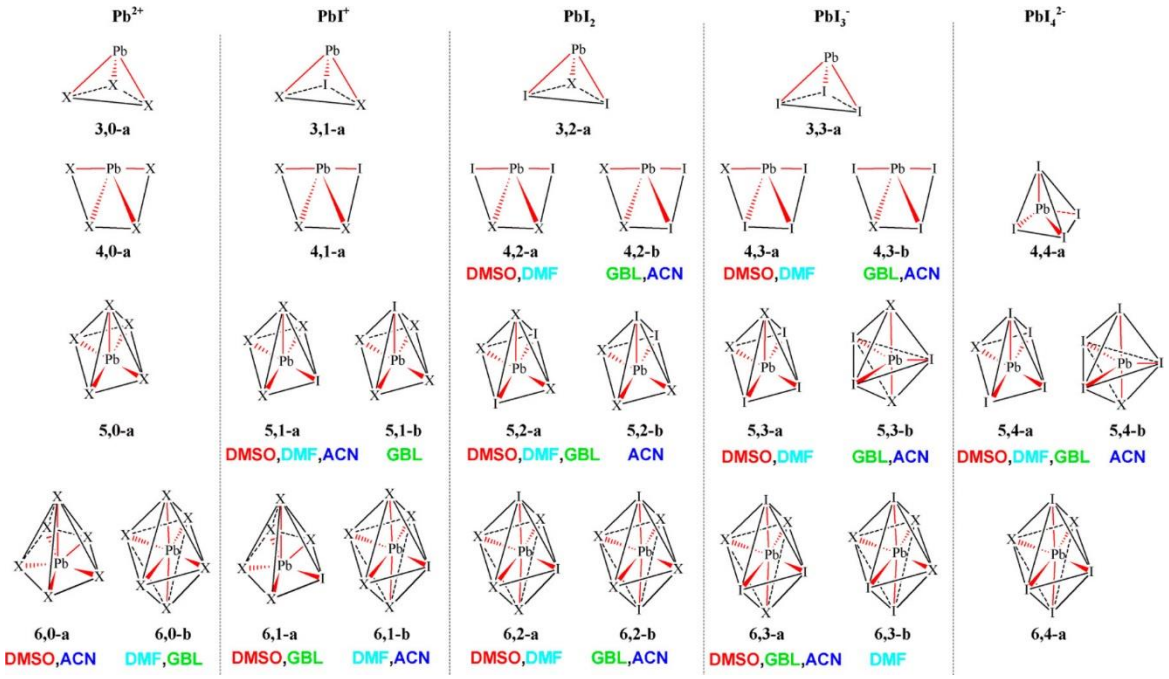

Fig. 2.2 Typical iodoplumbate species $[PbI_mX_n]^{2-m}$ (X = solvent) with most stable coordination. Reproduced with permission from ACS Appl. Energy Mater. 2019, 2, 5, 3400-3409.[5] Copyright 2019 American Chemical Society.

Precursor solution of lead halide perovskites (LHPs) contain various ions such as MA^+, FA^+, Cs^+, Cl^-, Br^-, I^-, and Pb^{2+} and those ions are not fully ionized in the solution. The intermediate complex structure of the iodoplumbate **(Fig. 2.2)**,[5] which is lead coordination with solvent and halide ions, varies depending on the kind and amount of ions that present in the solution, which eventually significantly influences the degradation or the crystallization of the perovskite materials and the formation of defects in the films **(Fig. 2.3)**.[6]

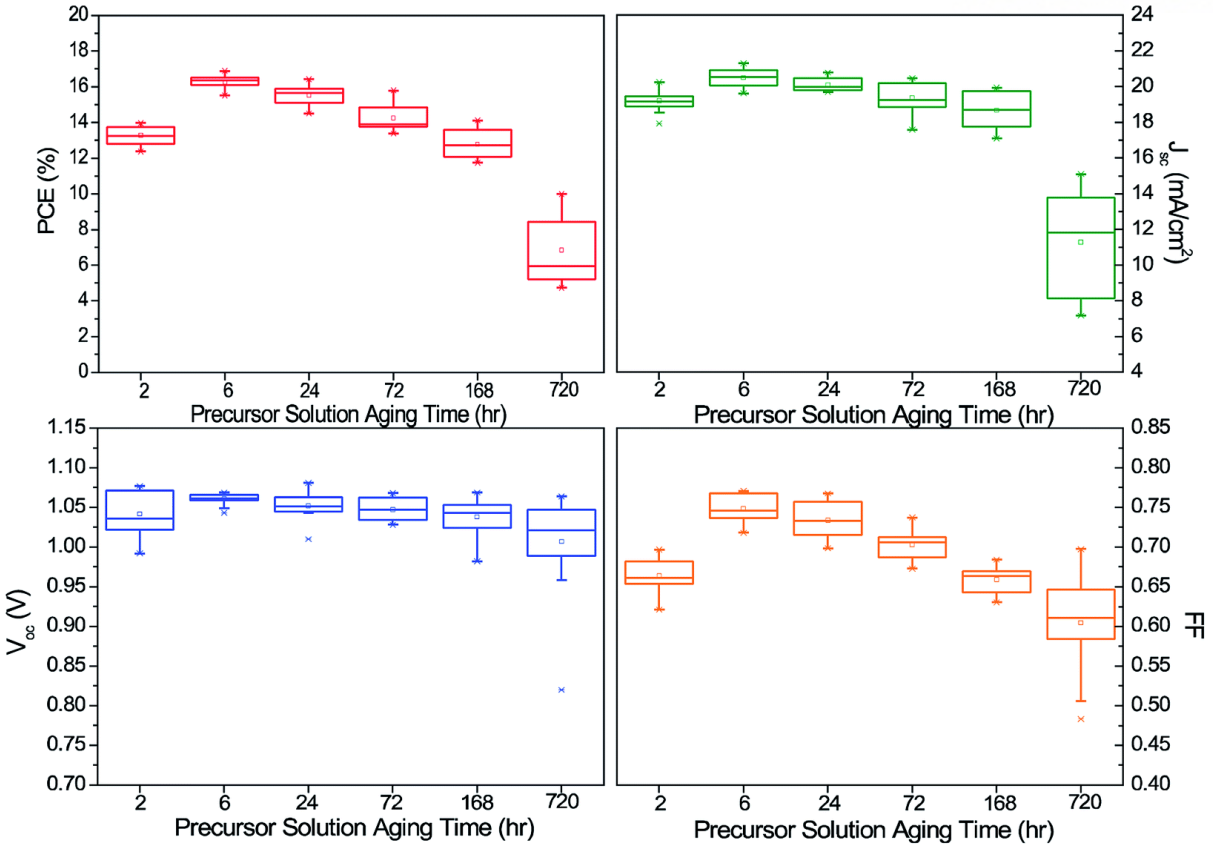

Fig. 2.3 An example of efficiency change depending on the aging time of the perovskite precursor solution. Reproduced with permission from RSC Adv., 2018, 8, 21551-21557.[6] Copyright 2018 The Royal Society of Chemistry.

2.2.2 Degradation of the solution

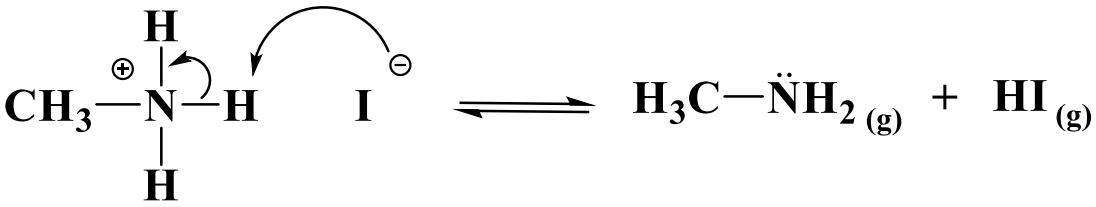

Fig. 2.4 Deprotonation of MA^+ in the dimethyl sulfoxide (DMSO).

Another factor that the properties of the perovskite precursor solution changes with time is the deprotonation of MA ions **(Fig. 2.4)**. Dou et al.[7] reported that the ration between the MA cations and Cs cations, which stabilize the $FAPbI_3$ phase, can vary with the aging time of the precursor solution. Heating a solution of the perovskite precursor salts in DMSO causes deprotonation of the MA cations to form volatile methylamine gas.[8, 9] However, no methods for stabilizing the MA cation have been proposed or no mechanisms responsible for the changes in the precursor solution with time have been elucidated. Therefore, it is important to develop methods and understand the underlying mechanisms for the long-term stabilization of the precursor solution containing organic cations, PbI_2, and $PbBr_2$ dissolved in dimethylformamide (DMF) and DMSO mixed solvent, to improve the reproducibility window of the processing of thin films from solution processes for fabricating efficient PSCs.

2.3 Stabilization of perovskite precursor solution

2.3.1 Elemental sulfur

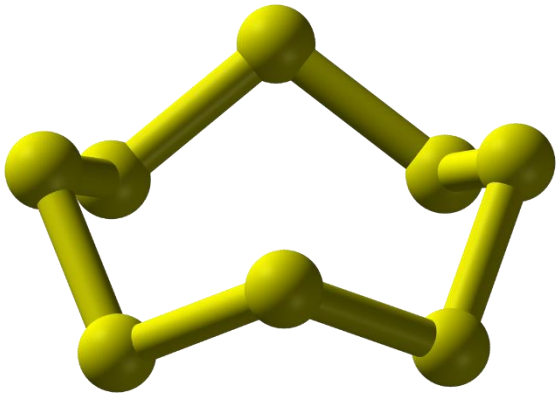

Fig. 2.5 Molecular configuration of elemental sulfur.

Elemental sulfur exists as very stable S_8 rings in its normal state with poor solubility and activity in most solvents.[10] The solvent used in our system, a mixture of DMF and DMSO, can dissolve up to 0.06 M. Cyclooctasulfur (S_8) can be in the form of ring-opened polysulfides (S_n^{X-}, n < 5). The sulfur dissolution processes in DMF have been proposed as its dissolution to smaller species ($S_8 \rightarrow 4S_2$), reduction ($2S_2 + 2e^- \rightarrow 2S_2^-$), and formation of anions ($2S_2^- \rightarrow S_4^{2-}$).[11] Similarly, the reduction of elemental sulfur in DMSO occurs as (i) reduction ($S_8 + 2e^- \rightarrow S_8^{2-}$), (ii) second reduction ($S_8^{2-} + 2e^- \rightarrow S_8^{4-}$), and (iii) formation of anions ($S_8^{4-} \rightarrow 2S_4^{2-}$).[12] Further, amine species readily react with it and induce the formation of free radicals of elemental sulfur.[13, 14] Nucleophilic attack of sulfur by nitrogen causes the ring-opening of S_8, resulting in an alkylammonium with an N-S bond: $R_2NH + S_8 \leftrightarrow R_2N^+H\text{-}S_8^-$. This complex reacts rapidly with other amines: $R_2N^+H\text{-}S_8^- + R_2NH \leftrightarrow R_2N^+H_2 + R_2N\text{-}S_8^-$ **(Fig. 2.6A)**. These reactions do not require a catalyst or free electron sources and can occur under mild conditions. In addition, this interaction between the amine groups and sulfur is easily deduced from the fact that sulfur is readily soluble in amine solvents such as methylamine solution, ethylenediamine, and MAI dissolved in DMF and DMSO. Thus, as postulated in chemical equilibrium reactions **(Fig. 2.6B)**, sulfur dissolved in the perovskite precursor solution forms a complex with methylamine and then inhibits its volatilization.

A

$$R_2NH + S_8 \leftrightarrow R_2N^+H - S_8^- \quad (1)$$

$$R_2N^+H - S_8^- + R_2NH \leftrightarrow R_2N^+H_2 + R_2N - S_8^- \quad (2)$$

(Alkylammonium N-polythioamine salt)

B

$$CH_3NH_2 + S_8 \leftrightarrow CH_3N^+H_2 - S_8^- \quad (1)$$

$$CH_3N^+H_2 - S_8^- + CH_3NH_2 \leftrightarrow CH_3N^+H_3 + CH_3NH - S_8^- \quad (2)$$

Fig. 2.6 (A) Mechanism of reaction between elemental sulfur and amine species. **(B)** Proposed mechanism of reaction between elemental sulfur and MA ions.

2.3.2 Results

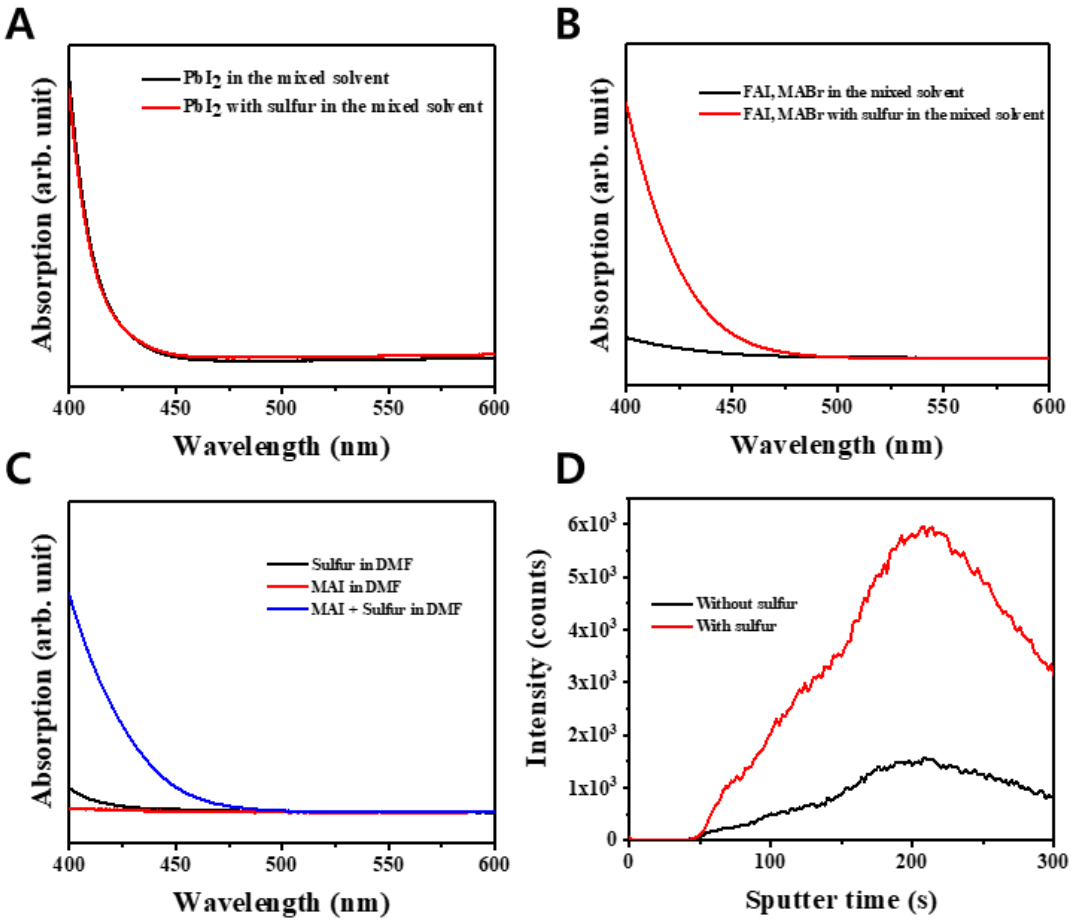

Fig. 2.7 Ultraviolet-visible (UV-vis) absorption spectra of **(A)** PbI_2 dissolved in DMF and DMSO; **(B)** FAI and MABr dissolved in DMF and DMSO; **(C)** MAI, sulfur, and a mixture of MAI and sulfur dissolved in DMF. **(D)** Depth profiling of S^- by time-of-flight secondary ion mass spectrometry (ToF-SIMS).

The easier formation of a complex with MA than with iodoplumbate dissolved in a precursor solution can be determined by comparing the differences in the absorbance caused by the addition of sulfur to a solution containing only PbI_2 or only MA. **Fig. 2.7A-C** shows the UV−vis absorption spectra obtained before and after adding sulfur to a solution containing only MA/FA and PbI_2. If elemental sulfur is ionized to sulfur species such as S^{2-}, S^{3-}, S^{4-}, S_4^{2-}, and S_8^{2-}, absorption bands are observed between 400 and 650 nm.[10] However, we could not observe these absorption bands in the UV−vis absorption spectra. The absorption noted for PbI_2 dissolved in sulfur containing DMF and DMSO (4:1 v/v) mixed solvent was the same as that for only PbI_2 dissolved in the mixed solvent without sulfur **(Fig. 2.7A)**. Furthermore, we could not observe the formation of PbS, which should be insoluble in our solvent

because if sulfur is ionized as free anions, it can readily react with the Pb cations to form PbS.[15] Therefore, elemental S may have been preferentially coordinated by MA, FA, or the solvent molecules without the formation of ionized species. The MAI-containing solution, however, showed a difference in the UV−vis absorption spectrum **(Fig. 2.7B)**. Compared with the solutions containing only MAI (5 mg mL^{-1}) and only elemental sulfur (1 mg mL^{-1}), the one with both MAI (5 mg mL^{-1}) and elemental sulfur (1 mg mL^{-1}) showed different absorption. FAI and MABr dissolved in the mixed solvent and in the perovskite precursor solution showed the same tendency as MAI in a DMF solution **(Fig. 2.7C)**. In addition, in the ToF-SIMS of **Fig. 2.7D**, we see that the perovskite layer obtained from the sulfur containing precursor solution is strongly enriched in sulfur relative to the pristine perovskite layer.

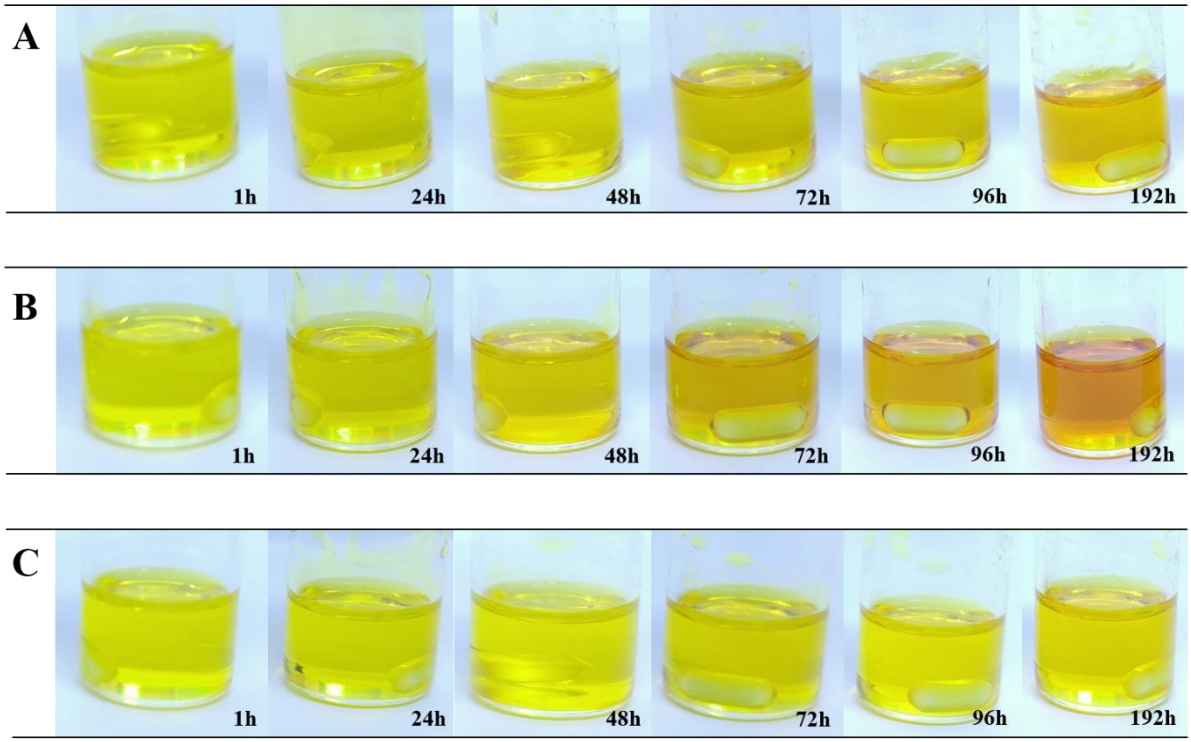

Fig. 2.8 Perovskite precursor solution color change depends on time. **(A)** $FAPbI_3$ black powder is dissolved in a mixed solvent of DMF/DMSO. **(B)** Conventional perovskite precursor solution wherein both $FAPbI_3$ and $MAPbBr_3$ powders are dissolved in the mixed solvent. **(C)** Elemental sulfur is added to the conventional solution.

In the solution state, we observed a visual difference between a solution of only $FAPbI_3$ in the DMF and DMSO (8:2 v/v) mixed solvent and the conventional $(FAPbI_3)_{0.95}(MAPbBr_3)_{0.05}$ perovskite precursor salts in the mixed solvent with and without sulfur, with progress in time **(Fig. 2.8)**. The hydroiodic acid (HI) solution changed its color from transparent to dark red with time because iodide

(I^-) was gradually oxidized to molecular iodine (I_2). Similarly, in the perovskite precursor solution without sulfur, volatile methylamine was lost with time, and excess HI was easily oxidized to I_2. The

color of the solution with only black $FAPbI_3$ powder dissolved in the mixed solvent changed slightly **(Fig. 2.8A)**. For the perovskite precursor solution without sulfur, the color change was more rapid **(Fig. 2.8B)**. In the case of sulfur added to the conventional perovskite precursor solution, the color change was not distinguishable **(Fig. 2.8C)**. This means that the added sulfur protects the methyl ammonium cation and stabilizes the iodide anion.

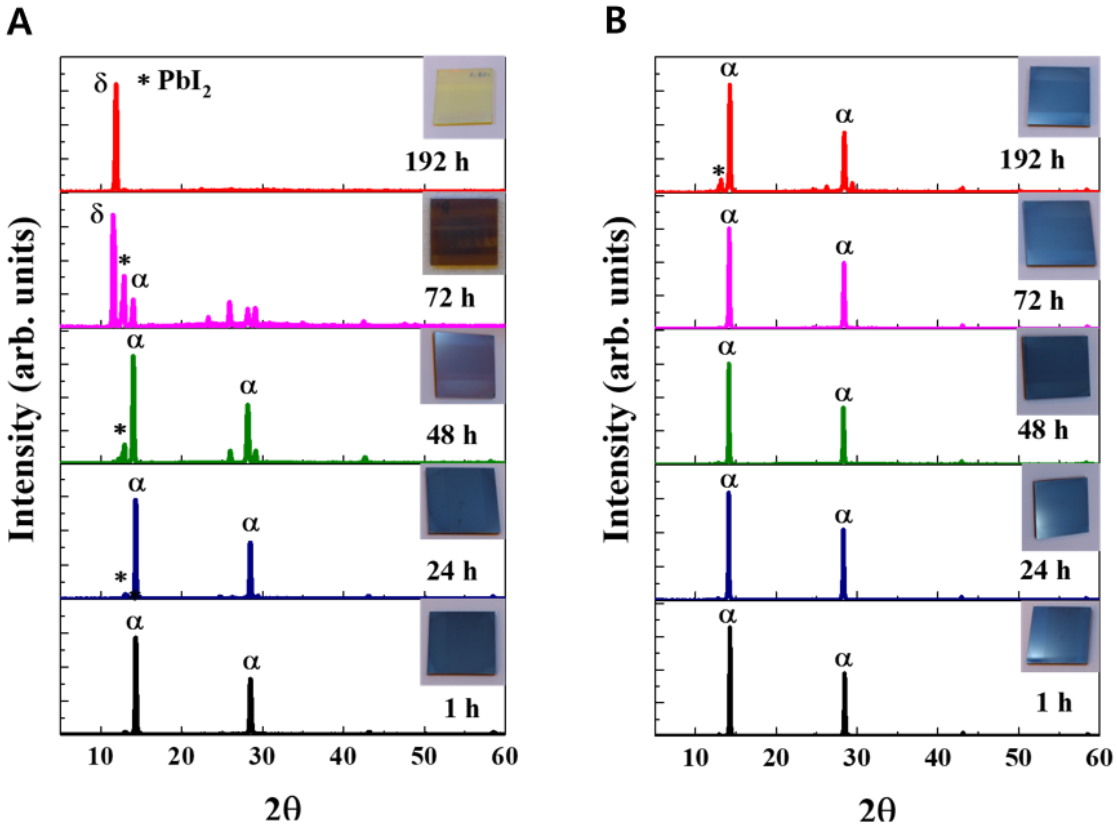

Fig. 2.9 X-ray diffraction (XRD) patterns and photographic images of films deposited from a precursor solution aged for times **(A)** without and **(B)** with sulfur.

The crystal structures of the films deposited from the precursor solutions with and without sulfur were analyzed by XRD, and the results are compared in **Fig. 2.9A, B** as a function of the aging time of the precursor solution. In the XRD patterns, the main XRD peaks of α-$FAPbI_3$, δ-$FAPbI_3$, and PbI_2 appear at 2θ = 13.9°, 11.8°, and 12.6°, respectively. PbI_2 peaks were observed when the precursor solution without the sulfur additive was aged for more than 24 h, and the intensities of these peaks increased with increasing aging time. In a thin film deposited with a precursor solution aged for 72 h, the δ-$FAPbI_3$

phase was observed. The appearance of PbI_2 and δ-$FAPbI_3$ in films obtained from aged precursor solutions is consistent with previously reported results.[16] Finally, in a film deposited from a solution aged for 192 h, all the α-$FAPbI_3$ was completely converted to δ-$FAPbI_3$ **(Fig. 2.9A)**. In contrast, films deposited with the sulfur-containing precursor solutions retained the α-$FAPbI_3$ phase without the appearance of δ-$FAPbI_3$ even after more than 1 week (192 h) of stirring the solution, whereas only a small amount of PbI_2 was produced **(Fig. 2.9B)**.

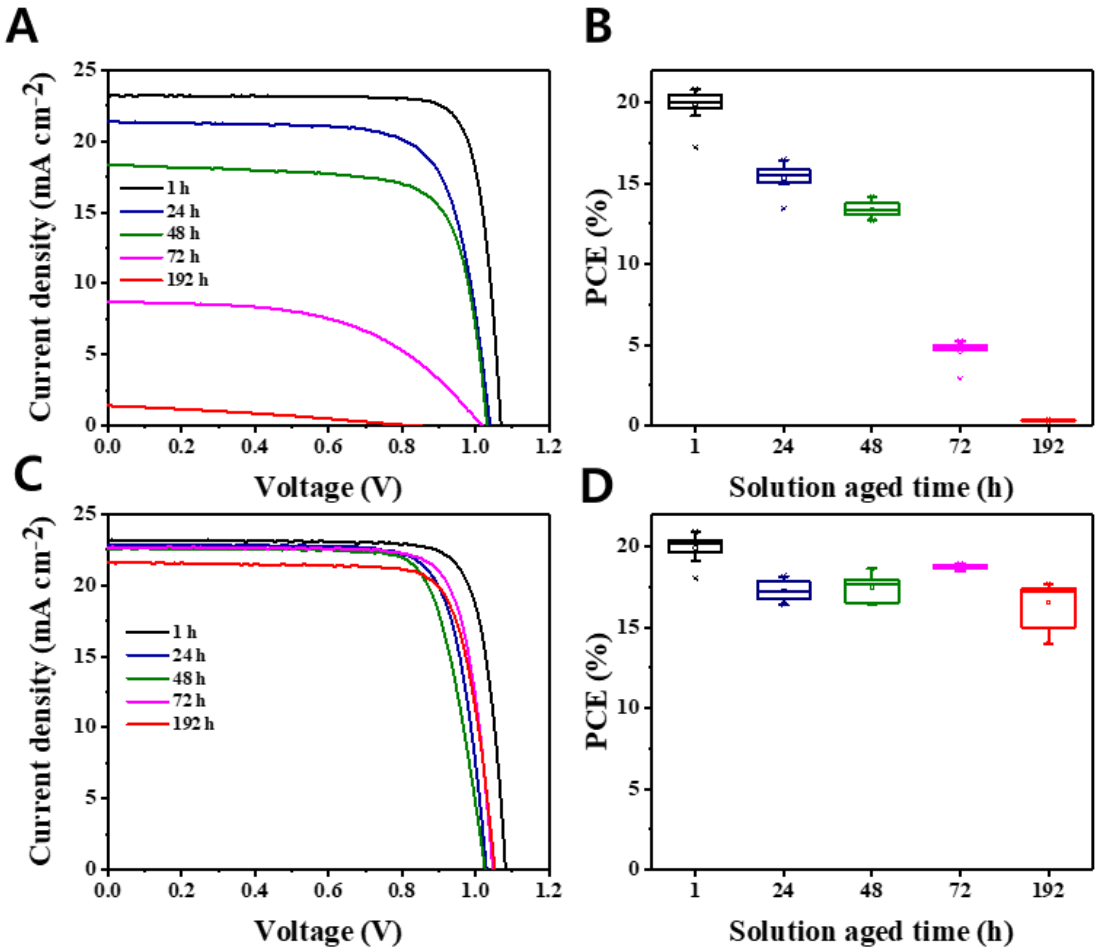

Fig. 2.10 J-V curves and distribution of power conversion efficiency (PCE) of PSCs fabricated as a function of the aging time of the precursor solutions **(A, B)** without and **(C, D)** with sulfur additive (0.03 M).

Fig. 2.10 shows the *J-V* curves and variation in the PCE of PSCs fabricated from perovskite precursor solutions without or with different amounts of the sulfur additive. Before spin-coating the perovskite layer, the perovskite precursor solution in the capped vial was maintained at 60 °C with stirring in a room lit with white light at 20%–35% humidity. After a certain aging time, the precursor solution was

spin-coated without cooling to room temperature. The *J–V* characteristics and distribution of the PCE of the solar cells depended on the aging time of the precursor solution. The PCE of PSCs fabricated from a perovskite precursor solution without the sulfur additive declined rapidly **(Fig. 2.10A, B)**; the PCE of the PSC (24 h) derived from a precursor solution aged for only 24 h dropped by 15% as compared to the PCE (20.82%) of a device (1h) fabricated from a freshly prepared precursor solution **(Fig. 2.10 C, D)**. For a PSC (72 h) derived from a solution aged for 72 h, the efficiency reduced to 75% of the initial value (20.82%). As shown in **Fig. 2.10A** and **Table 2.1**, the short-circuit current (J_{sc}), open-circuit voltage (V_{oc}), and fill factor, which determine the efficiency, decreased simultaneously, with the most dominant factor being J_{sc}. However, the PCE of the PSC derived from a precursor solution containing 0.03 M sulfur remained at ≈18% despite aging the precursor solution for over a week. The decline in the J_{sc} of devices fabricated using the sulfur-containing precursor was found to be very small at ≈1 mA cm^{-2}.

Table 2.1 Performance parameters of devices fabricated using precursor solution aged for **(A)** 0 h and **(B)** 72 h with and without 0.03 M elemental sulfur.

A

Elemental sulfur contents	J_{sc} [mA/cm²]	V_{oc} [V]	FF [%]	PCE [%]
0M (Ref.)	23.47	1.08	82.31	20.82
0.03M	23.43	1.08	82.82	20.91

B

Elemental sulfur contents	J_{sc} [mA/cm²]	V_{oc} [V]	FF [%]	PCE [%]
0M (Ref.)	8.72	1.02	52.59	4.67
0.03M	22.28	1.05	81.38	18.99

2.4 Conclusion

In summary, we significantly improved the stability of a perovskite precursor solution upon aging by adding elemental sulfur to it. The stability of the precursor solutions was investigated with respect to aging time by evaluating the performance of the derived PSC and by XRD analyses of the films spin-coated from them. The stability of the precursor solution with aging time is related to the transformation of the α-$FAPbI_3$ phase to the δ-$FAPbI_3$ one due to the reduction of MA present with FA. Sulfur in the precursor solution formed a complex with MA, thus retaining MA in the solution, thereby increasing the stability of the perovskite solution. Although the sulfur added in the precursor solution remained in the perovskite film, the efficiency of the derived PSC did not decrease substantially, while the chemical stability of the PSCs increased. The findings of our study are expected to expand the experimental window for the reproducibility of the high efficiency of the PSC fabrication process and can provide a basic technology for the commercialization of PSCs.

Chapter 3. Highly Efficient and Stable Perovskite Solar Cells

3.1 Efficiency increases of perovskite solar cells

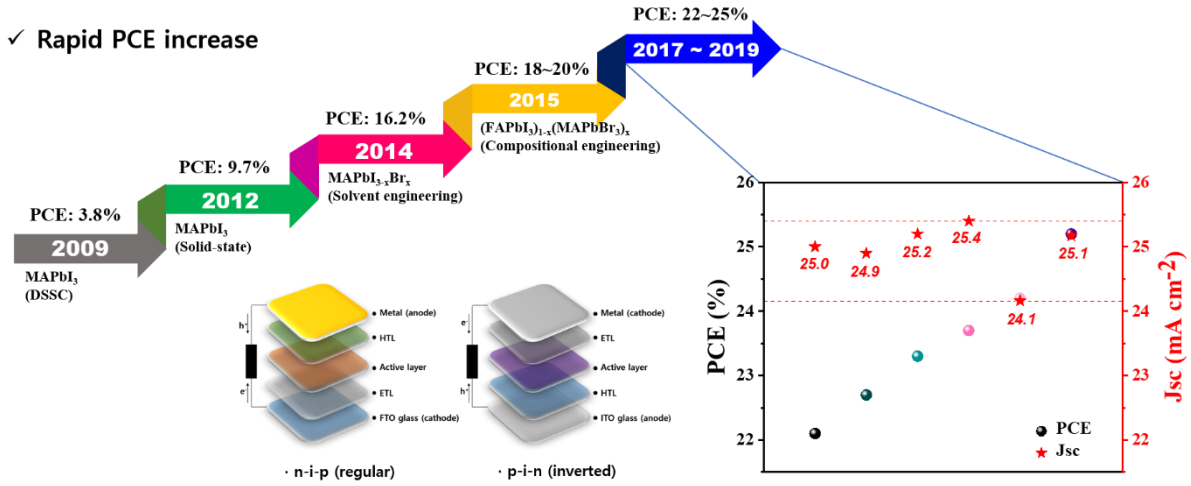

Fig. 3.1 Schematic diagram of the increase in efficiency of perovskite solar cells and perovskite devices structure of n(negative)-i(intrinsic)-p(positive) and p-i-n. And PCE and J_{sc} of certified champion efficiency from 2017 to 2019.

PSCs have increased in efficiency at a very rapid rate in the last decade **(Fig. 3.1)**. In 2009, professor Miyasaka firstly demonstrated 3.8% of efficiency perovskite solar cells with dye-sensitized solar cells (DSSC).[17] Three years later, professor Nam-Gyu Park demonstrated all-solid-state perovskite solar cells with 9% of efficiency.[18] In 2014, efficiency of 16.2% was achieved through solvent-engineering.[19] From this point, the anti-solvent method was widely used to deposit uniform and dense perovskite layer. A year later, 18% and 20% were achieved through compositional engineering using $FAPbI_3$-based perovskites.[20, 21] From here, mixed-cation system was widely used. Thereafter, efficiency increased from 22% to 25.2% over the three years from 2017 to 2019.[21-23] For now, record efficiencies were achieved with n-i-p structure.

3.2 Maintaining bandgap

3.2.1 Shockley-Queisser limit

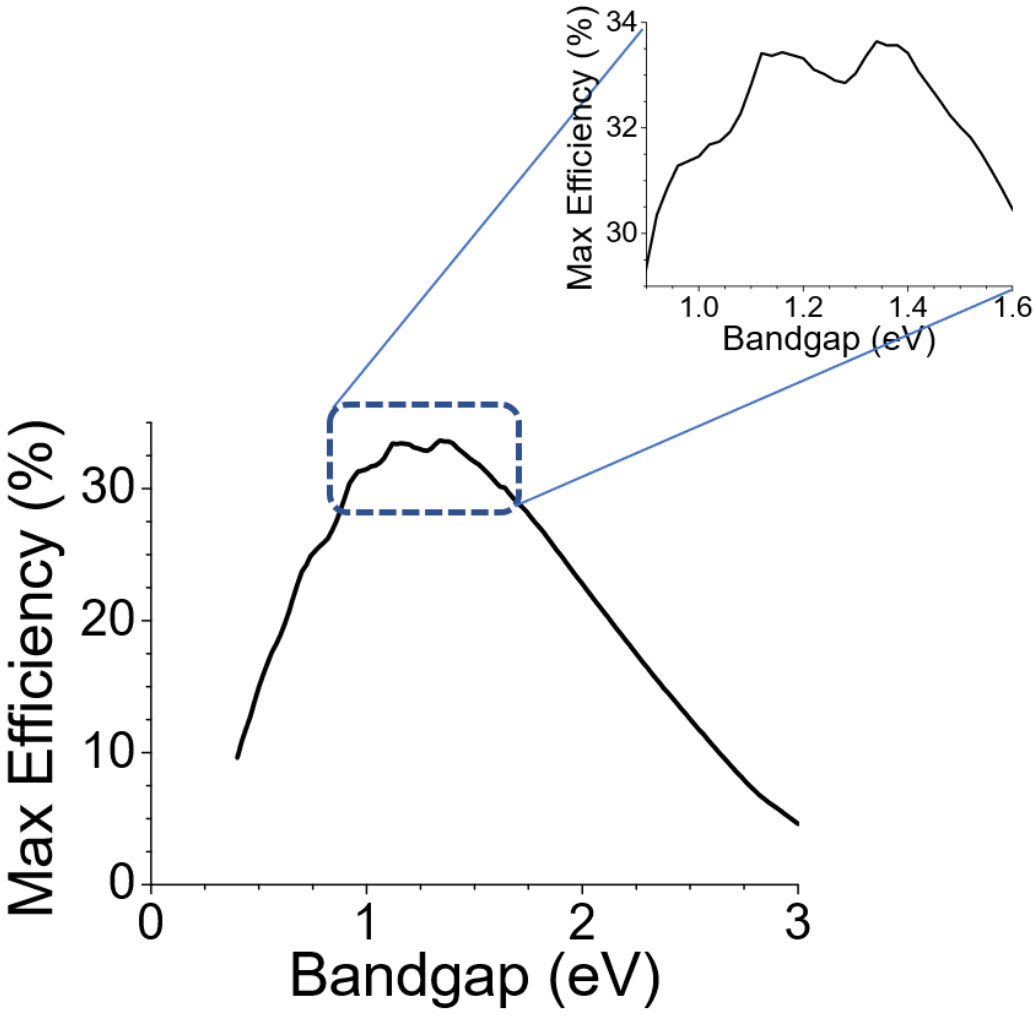

Fig. 3.2 Shockley-Queisser (SQ) limit which present theoretical maximum efficiency of photovoltaic devices depends on bandgap of photo-absorbing material.

In physics, the SQ limit is the maximum theoretical efficiency of a single-junction solar cell to collect power form the cell where the only loss mechanism is radiative recombination in the solar cell.[24] The theoretical maximum efficiency is 33.7% for a solar cell with a bandgap of 1.34 eV under global solar spectra (AM 1.5G) **(Fig. 3.2)**. The bandgaps of lead halide perovskites (LHPs) are wider than the ideal value **(Table 3.1)**. Among the LHPs, bandgap of $FAPbI_3$ is near optimum but phase stabilizer such as $MAPbBr_3$ widen its bandgap.

Table 3.1 The bandgaps of representative LHPs.

	$FAPbI_3$	$MAPbI_3$	$MAPbBr_3$	$CsPbI_3$	$CsPbBr_3$
Bandgap (eV)	1.47-1.53	1.54-1.60	2.20-2.30	1.68-1.74	2.30-2.40

3.2.2 New additive: $MDACl_2$

Efforts to improve the stability of $FAPbI_3$ have focused on mixed cation-anion hybrid LHPs that incorporate several cations, anions, or both, such as the FA_xMA_{1-x} double cation or the $FA_{1-x-y}MA_xCs_y$ triple cation. This incorporation is achieved by the partial replacement of FA^+, MA^+, Rb^+, Cs^+, Br^-, and I^-.[25, 26] Nevertheless, when MA and Br are alloyed in $FAPbI_3$, various problems such as low thermal stability[27] caused by the addition of MA, phase separation[28] caused by the presence of mixed halides, and reduced photon absorption arise, thereby resulting in low current density owing to an undesirable increase in the bandgap. Although the α-$FAPbI_3$ phase without MA can be stabilized by incorporating phenylethylammonium lead iodide[29] through surface functionalization[30] or by using both Rb and Cs,[31] the resulting PCE is still low when compared with that obtained with the use of the FA_xMA_{1-x} double cation. To further increase the PCE by enhancing the photocurrent density resulting from increased light harvesting, a new composition is needed that stabilizes the α-phase while maintaining the inherent bandgap of $FAPbI_3$. The ionic radii and molecular configuration of methylenediammonium [$^+H_3N–CH_2–NH_3^+$ (MDA), 262 picometers (pm), calculated] and FA ($^+H_2N=CH–NH_2$, 256 pm) are comparable except for the valence-state difference **(Fig. 3.3)**. However, MDA has more hydrogen atoms than FA and even MA, which means that it can form a greater number of H bonds with I^-. Thus, MDA could structurally stabilize the α-FAPbI3 in even smaller amounts than does MA.

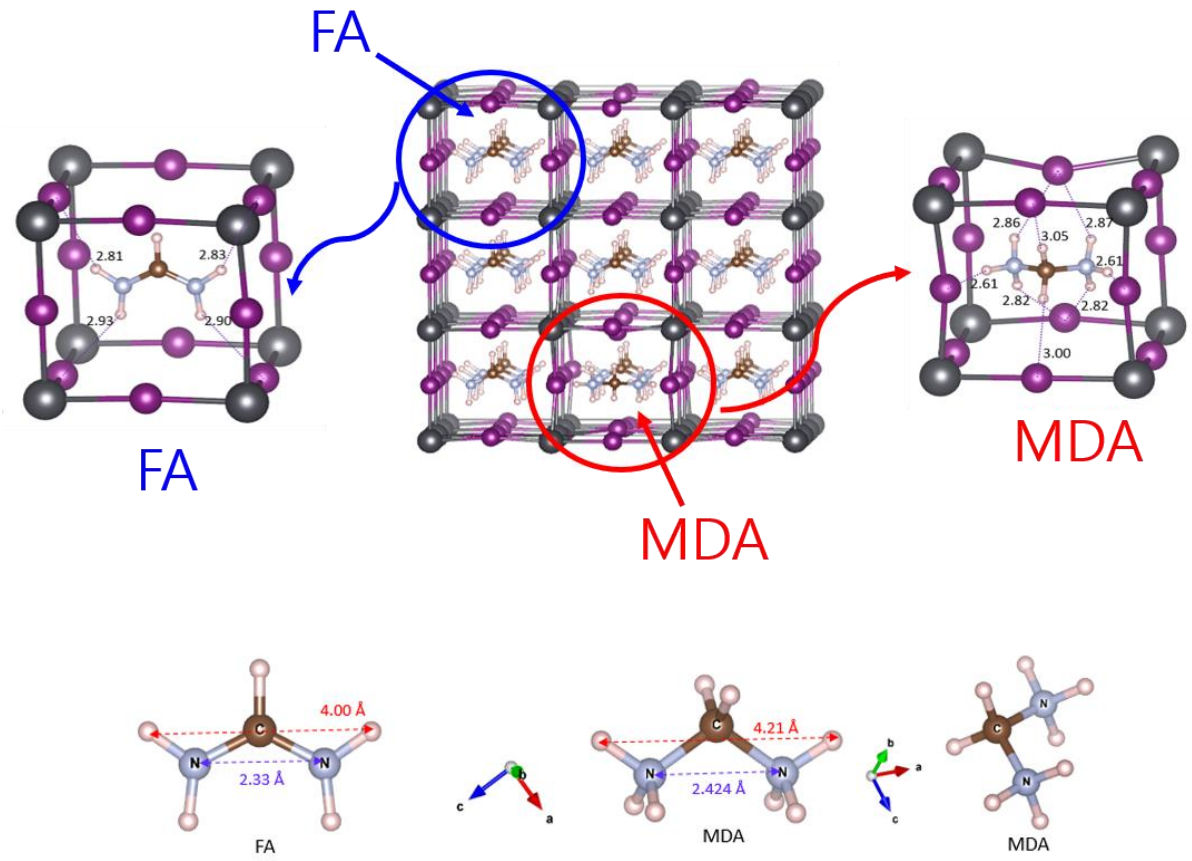

Fig. 3.3 Molecular configuration of FA^+ and MDA^+ and structure relaxation for the electronic band structures of MDA doped $FAPbI_3$.

3.2.3 Results

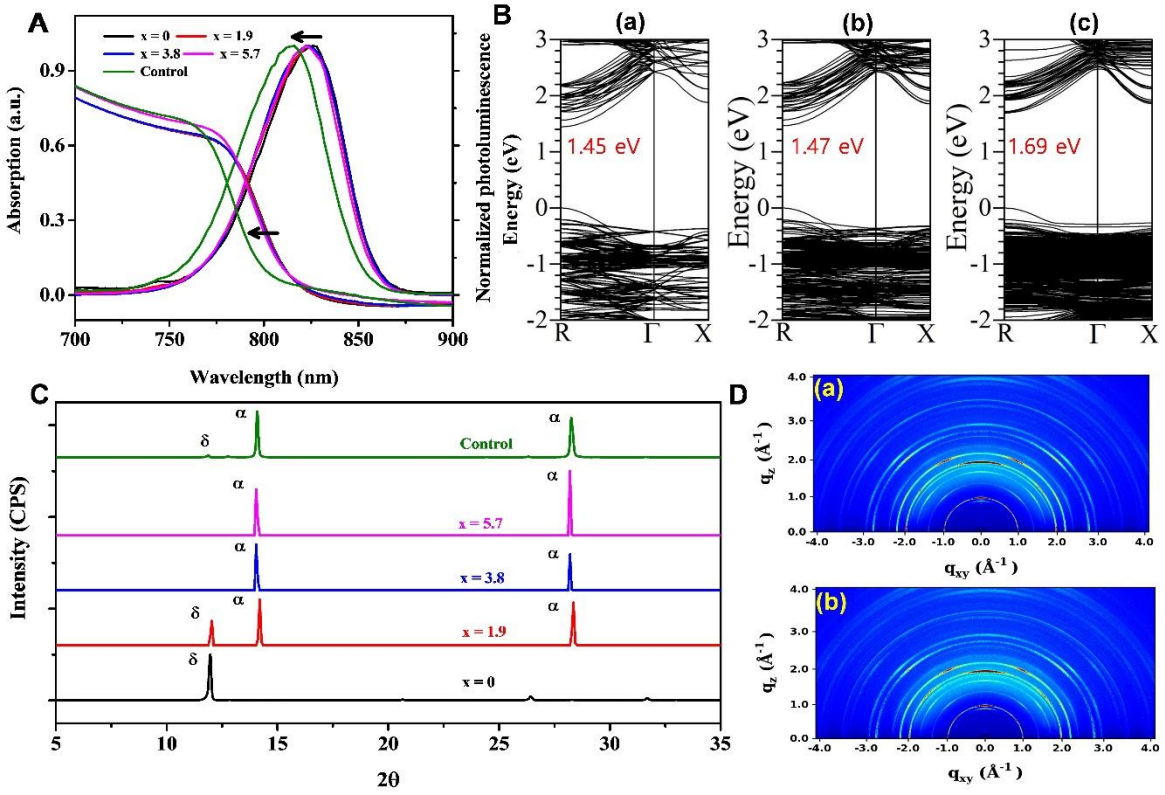

Fig. 3.4 Preparation of $FAPbI_3$:x$MDACl_2$ (x = 0, 1.9, 3.8, and 5.7 mol%). **(A)** Ultraviolet-visible (UV-vis) absorption and photoluminescence (PL) spectra of perovskite layers with different x values. The perovskite layer based on $0.95FAPbI_3/0.05MAPbBr_3$ as control was also investigated. **(B)** Electronic band structures of (a) $FAPbI_3$, (b) representative $FA_{0.926}(V_{FA})_{0.037}MDA_{0.037}PbI_3$, and (c) representative $FA_{0.963}MDA_{0.037}PbI_3(Cl_i)_{0.037}$. The doping amount of 0.037 in the calculation was given by 1/27 (= 0.03704) based on the 3x3x3 supercell for the composition close to the actual experiment. **(C)** X-ray diffraction (XRD) patterns of perovskite prepared with different x values and the control layer exposed to 80% humidity for 24 h after annealing of the coatings of the precursor solution at 150 °C for 10 min. **(D)** Grazing-incidence wide-angle x-ray scattering (GIWAXS) 2D images at full depth of x-ray incident angle for perovskite layers for (a) x = 3.8 mol% and (b) control.

We deposited a thin film of $FAPbI_3$ incorporating $MDACl_2$ with a process similar to that reported previously for state-of-art mixed perovskites[32-35] but adding $MDACl_2$ instead of $MAPbBr_3$. The UV-vis absorption spectra of $FAPbI_3$:x$MDACl_2$ (x = 0, 1.9, 3.8, and 5.7 mol%) slightly blue-shifted with increasing amounts of $MDACl_2$ **(Fig. 3.4A)**. This result is consistent with the corresponding shifts of photoluminescence (PL) emission peaks from 826 nm to 824, 822, and 820 nm, and 816 nm for the

control. The presence of MDA in the perovskite was confirmed by Fourier-transform infrared spectroscopy (FT-IR, **Fig. 3.5**) and nuclear magnetic resonance (NMR, **Fig. 3.6**). Thus, $MDACl_2$ may have been incorporated into the perovskite lattice within the experimental x-value range.

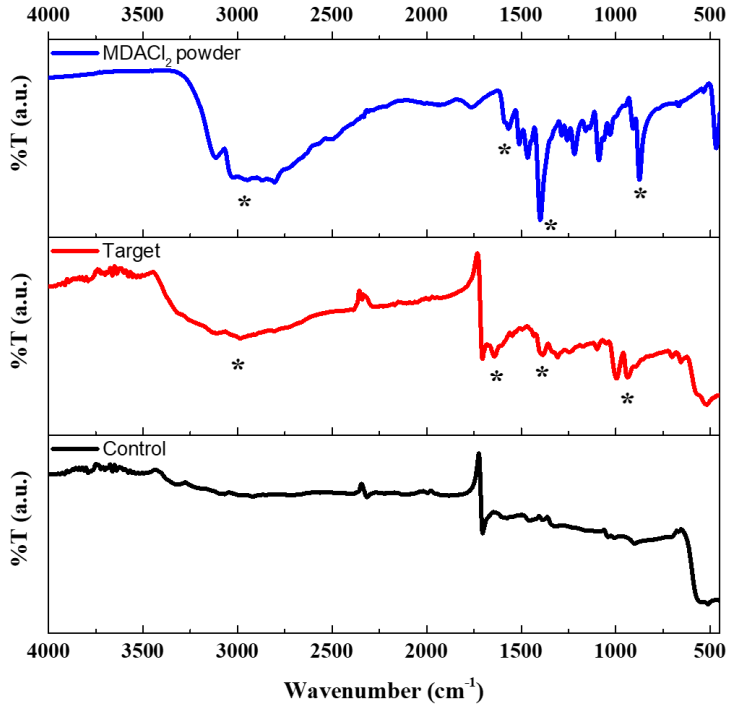

Fig. 3.5 Comparison of Fourier-transform infrared spectroscopy results of $MDACl_2$, target, and control.

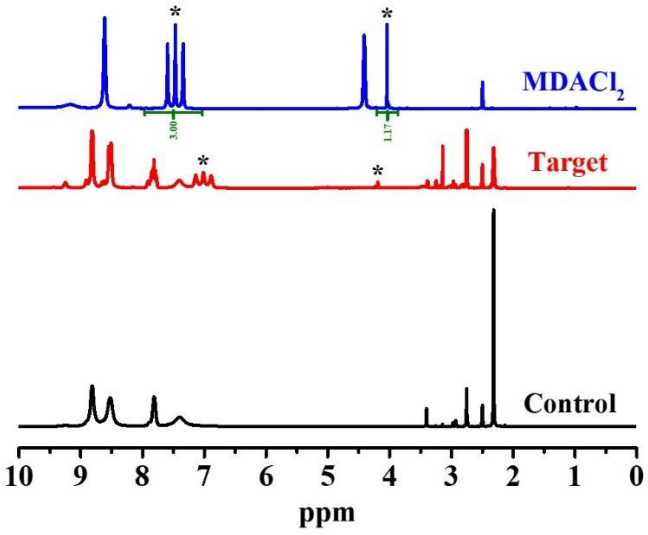

Fig. 3.6 Nuclear magnetic resonance (NMR) spectra of $MDACl_2$, target, and control.

The bandgap changes in $FAPbI_3$ caused by the introduction of $MDACl_2$ were calculated via density functional theory (DFT) and compared for two cases as per eqs. (1) and (2).

$$\text{FA vacancy: } (FA^{+1}_{1-2x}MDA^{+2}_{x})Pb^{2+}I^{-1}_{3}Cl^{-1}_{2x} \rightarrow [(FA^{+1}_{1-2x}MDA^{+2}_{x})Pb^{2+}I^{-1}_{3}] + V_{xFA} + 2xFACl \quad ---(1)$$

$$\text{Cl interstial insertion: } (FA^{+1}_{1-x}MDA^{+2}_{x})Pb^{2+}I^{-1}_{3}Cl^{-1}_{2x} \rightarrow [(FA^{+1}_{1-x}MDA^{+2}_{x})Pb^{2+}I^{-1}_{3}Cl^{-1}_{x}] + Cl_{xi} + xFACl \quad ---(2)$$

Equations (1) and (2) represent compositions that assume the FA cation vacancies and the insertion of Cl^- with a small ionic radius, respectively, upon the addition of $MDACl_2$. The bandgap (1.47 eV) with the FA-vacancy (V_{FA}) composition as per Eq. (1) is slightly greater than that of pristine $FAPbI_3$ (1.45 eV), and the Cl interstitial composition (Cl_i) based on eq. (2) yielded an increased band gap of 1.69 eV **(Fig. 3.4B)**. We expected that the addition of $MDACl_2$ to $FAPbI_3$ would mainly result in FA defects and the possible induction of PL quenching. However, adding 3.8 mol% $MDACl_2$ to $FAPbI_3$ enhanced the PL quantum yield as measured with an integrated sphere but was greatly reduced with further $MDACl_2$ addition. This result implies that the FA defects did not act as deep electron traps. As reported previously,[27] pristine $FAPbI_3$ thin films annealed at high temperatures exhibited a black α-phase that absorbed long-wavelength light. However, the α-phase transitions to the yellow δ-phase within 10 days at room temperature and within 1 day under high-humidity conditions[ref] because the metastable polymorphs stabilized at high temperature are preferably converted back to the thermodynamically stable phase below 120°C.

The structural stabilization of the α-phase in $FAPbI_3$ with added cations can be explained by several factors. First, the α-phase stabilization by smaller cations such as Cs^+ can be understood from the Goldschmidt tolerance factor t approaching 0.9, which is similar to that of $MAPbI_3$, by mixing $FAPbI_3$ (t ~ 1) and $CsPbI_3$ (t ~ 0.8).[36] Second, cation mixing in the A-sites affords entropic stabilization through the resulting entropic gain and small internal energy input to form their solid solution.[26] Third, the stabilization of α-$FAPbI_3$ with MA cations can be explained by the presence of strong H bonds between I^- and H–N groups.[37] The α-$FAPbI_3$ phase can be more easily stabilized when MA, Cs, or both are used with Br^- of small ionic radii, and high-efficiency PSCs are normally fabricated using α-$FAPbI_3$ stabilized by mixed cations and anions.

We expected that MDA could stabilize α-$FAPbI_3$ through the partial replacement of FA sites because MDA has more H groups with an ionic radius similar with that of FA and a stronger ionic interaction of its divalent state. The XRD patterns of $FAPbI_3$:x$MDACl_2$ (x = 0, 1.9, 3.8, and 5.7 mol%) and the control layers exposed to 80% humidity for 24 h after annealing of the coatings of precursor solution at 150 °C for 10 min **(Fig. 3.4C)** show two peaks characteristic of the α-$FAPbI_3$ phase at 14.3° and 28.6° assigned to the (001) and (002) crystal planes, respectively, and one peak at 11.6° corresponding to the δ-phase. After exposure to high humidity for 24 h, pure $FAPbI_3$ completely converted to the δ-phase, and $FAPbI_3$ with 1.9 mol% $MDACl_2$ exhibited a strong phase transition, with the control also exhibiting a certain amount of the δ-phase. In contrast, $FAPbI_3$ incorporating 3.8 and 5.7 mol% of $MDACl_2$ retained the α-phase.

The addition of $MDACl_2$ likely formed FACl or substituted residual $MDACl_2$. However, the final annealed perovskite films did not exhibit any impurity peaks such as those of FACl and $MDACl_2$. This result implies that $MDACl_2$ was successfully incorporated into the $FAPbI_3$ perovskite lattices, and the resulting FACl was eliminated by annealing at 150°C for 10 min, because FACl easily volatilized during heat treatment. The structural phase of $FAPbI_3$ with and without the substitution of the representative 3.8 mol% MDA and presence of other phases such as FACl or $MDACl_2$ was further characterized via grazing-incidence wide-angle x-ray scattering (GIWAXS). In **Fig. 3.4D**, we observed diffraction rings assigned to α-$FAPbI_3$-$(100)_c$, α-$FAPbI_3$-$(200)_c$, α-$FAPbI_3$-$(210)_c$ δ-$FAPbI_3$-$(100)_h$, and PbI_2-$(001)_t$ for the two representative samples. In addition, different crystal orientations of α-$FAPbI_3$, $[100]_c$ and $[200]_c$, were observed as preferential GIWAXS peaks for both samples. The PbI_2 components remaining in both perovskite layers showed similar out-of-plane orientations. The GIWAXS ring patterns of α-$FAPbI_3$:x$MDACl_2$ (x = 0 and 3.8 mol%) did not exhibit appreciable differences, and the fitted azimuthal circular average GIWAXS 1D full spectra were also nearly identical, without showing any peaks related to FACl or $MDACl_2$. This result indicated that MDA is substituted into the $FAPbI_3$ lattice, as estimated from the conventional XRD analysis.

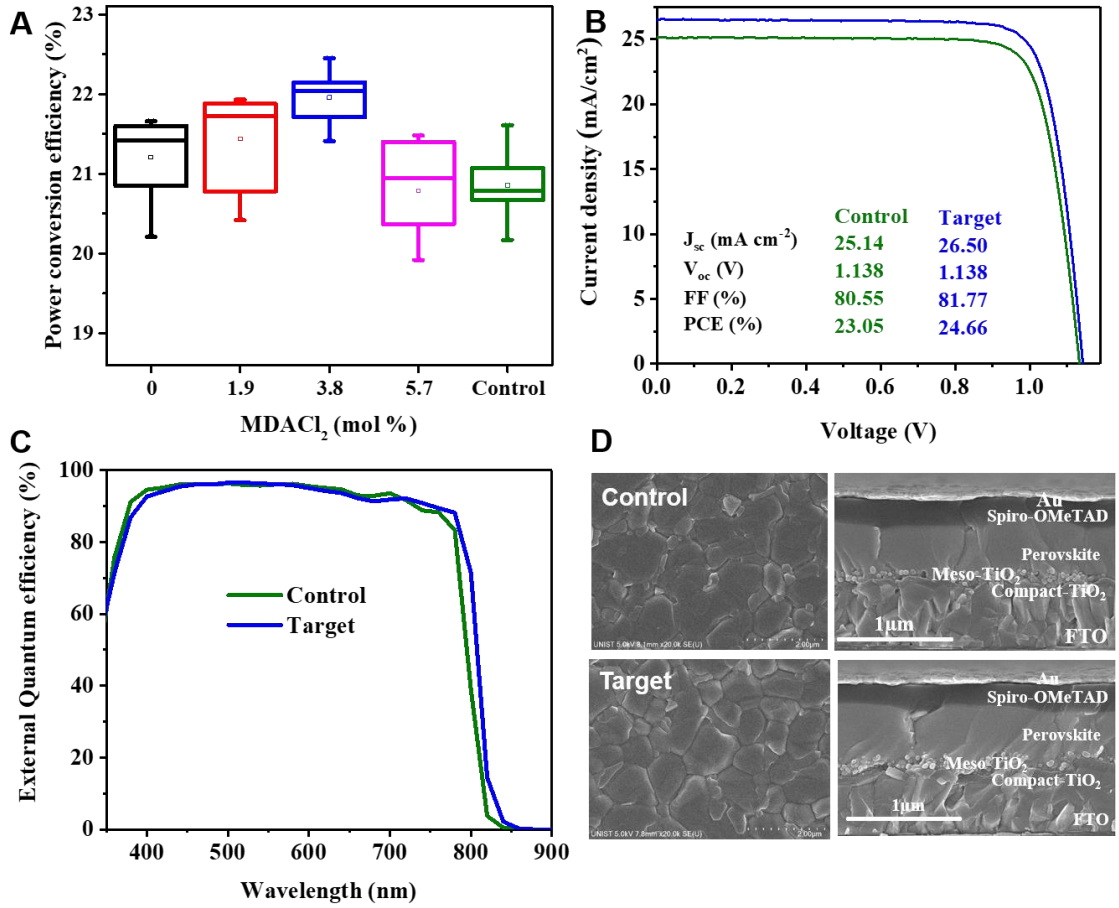

Fig. 3.7 Device performance. (A) Power conversion efficiency of perovskite solar cells fabricated with different x values of $FAPbI_3$:x$MDACl_2$ (x = 0, 1.9, 3.8, and 5.7 mol%) and the control. Comparison of **(B)** J–V curves and **(C)** external quantum efficiency (EQE) between target (x = 0.38 mol%) and control. **(D)** Comparison of surface morphologies and cross-sectional images of target and control acquired with scanning electron microscopy (SEM).

Fig. 3.7A compares the PCE distributions of the PSCs fabricated with $FAPbI_3$:x$MDACl_2$ (x = 0, 1.9, 3.8, and 5.7 mol%) and the control. The average PCE values of the PSCs fabricated with no $MDACl_2$ improved from 22.012 ± 0.51% to 22.46 ± 0.34% for 3.8 mol% $MDACl_2$ mainly from an increase in J_{SC}, while exhibiting similar or greater V_{OC} and FF values **(Fig. 3.8)**. When more $MDACl_2$ (5.7 mol%) was added, the degradation of crystallinity and PL caused the PCE slightly declined from a decrease in both J_{SC} and V_{OC}. The initial PCE of the PSC fabricated without $MDACl_2$ was fairly high[38] but decrease substantially over time because of the α-to-δ-phase transition **(Fig. 3.9)**.

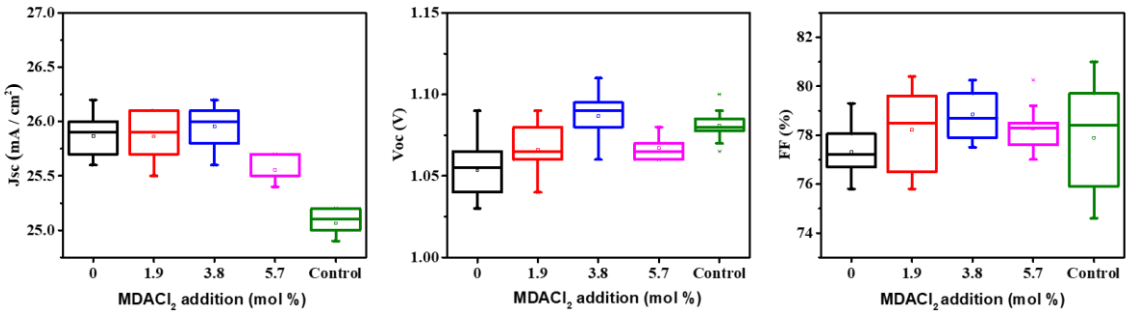

Fig. 3.8 Variation in J_{sc}, V_{oc}, and FF for different x values of $FAPbI_3$:$MDACl_2$ (x = 0, 1.9, 3.8, and 5.7 mol%) and control.

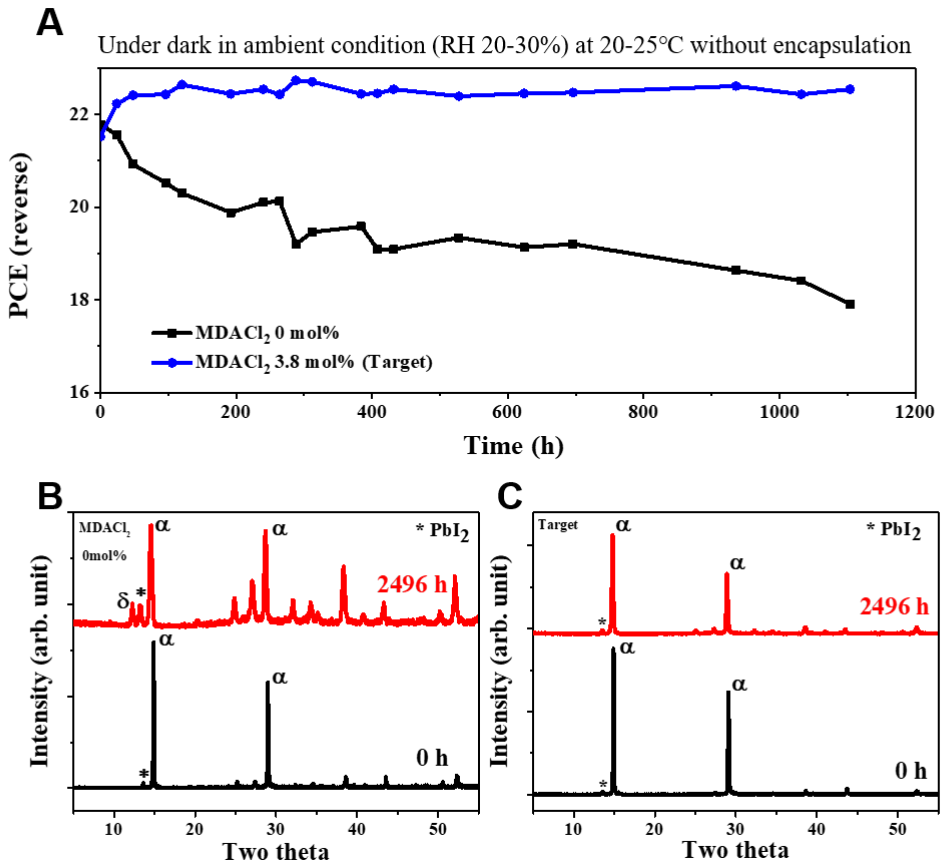

Fig. 3.9 (A) PCE changes in FTO/bl-TiO_2/mp-TiO_2/Perovskites (0, 3.8 mol%)/Spiro-OMeTAD/Au (unencapsulated) measured over time stored under ambient condition (RH 20-30%, 25 ℃) in a dark. **(B)** XRD patterns of perovskite layers after 2500 h of operation time.

Therefore, in terms of efficiency and phase stability, we fixed 3.8 mol% in an appropriate amount, and compared its characteristics with the control. We passivated the surface of the target and control layers by means of previously reported methods.[22] **Fig. 3.7B** compares the J–V characteristics, one of the "best-performing" PSCs fabricated with 3.8 mol% $MDACl_2$ *(denoted as the target)* and the control. The J_{SC}, V_{OC}, and FF values (table S1) calculated from the J–V curves of the target were estimated as 26.50 mA cm^{-2}, 1.14 V, and 81.77%, respectively; these correspond to a PCE of 24.66% under standard AM 1.5 conditions, mainly the result of the very high J_{SC} value. The control exhibited a PCE of 23.05%, with Jsc = 25.14 mA cm^{-2}, V_{OC} = 1.14 V, and FF = 80.55%. As expected, the surface passivation of perovskite layers improved both V_{OC} and FF, but J_{SC} remained almost unchanged, which resulted in the PCE of >24%. The external quantum efficiency (EQE) comparison of the control and target in **Fig. 3.7C** that the efficiency improvement of the PSC with $MDACl_2$ was the result of the expansion of the range of absorption wavelengths.

The improvement in PCE with a suitable amount of MDA meant that the negative influence of V_{FA} defects was compensated by other beneficial factors. Because the PCE of PSCs depends on the surface morphology of the perovskite layers, we compared the surface roughness and grain sizes of the target and the control with scanning electron microscopy (SEM). We found no notable differences of the cross-sectional thickness of the two representative layers, the control, and the target **(Fig. 3.7D)**, so the introduction of $MDACl_2$ into the precursor of $FAPbI_3$ did not affect the features of the perovskite layers. The performance factors for device shown in **Fig. 3.7B**, certified an accredited laboratory (Newport, USA) by means of the quasi-steady-state (QSS) method **(Fig. 3.10)**, a newly established measurement standard for certification, were J_{SC} = 26.1 mA cm^{-2}, V_{OC} = 1.15 V, and FF = 79.0%, which corresponds to a stabilized PCE of 23.73%, the highest reported for devices using mp-TiO_2 as an electrode. Another certified device recorded a very high J_{SC} (26.70 mA cm^{-2}) value, which is the highest reported in $FAPbI_3$-based PSCs, along with V_{OC} = 1.144 V and FF = 77.56%, corresponding to a stabilized PCE value of 23.69%. As per the certification process, the J_{SC} and V_{OC} values obtained from the QSS method were similar with the corresponding ones of the I–V measurements conducted in the reverse-bias mode; however, the FF was reduced.

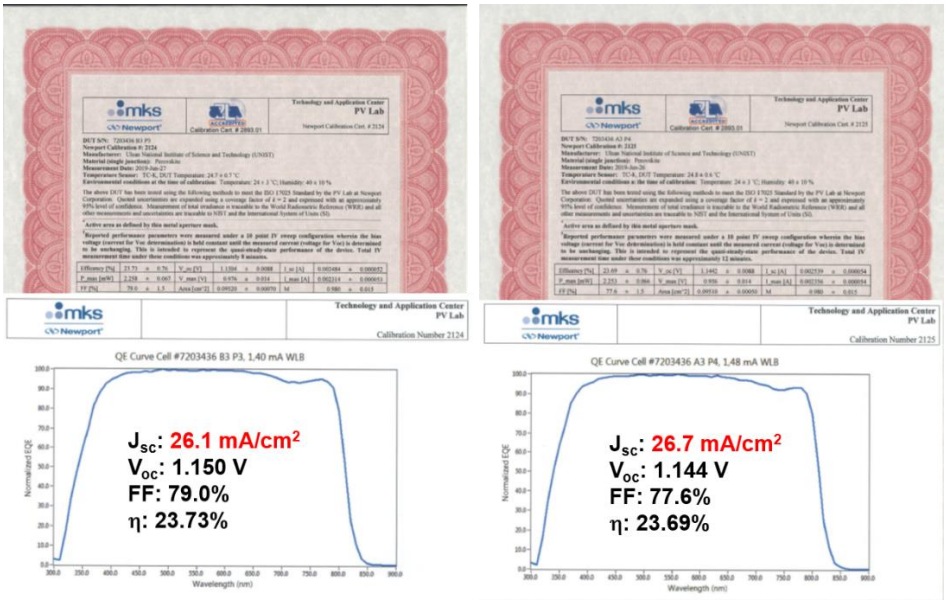

Fig. 3.10 Certified results for the target devices from accredited photovoltaic certification laboratory (Newport, USA).

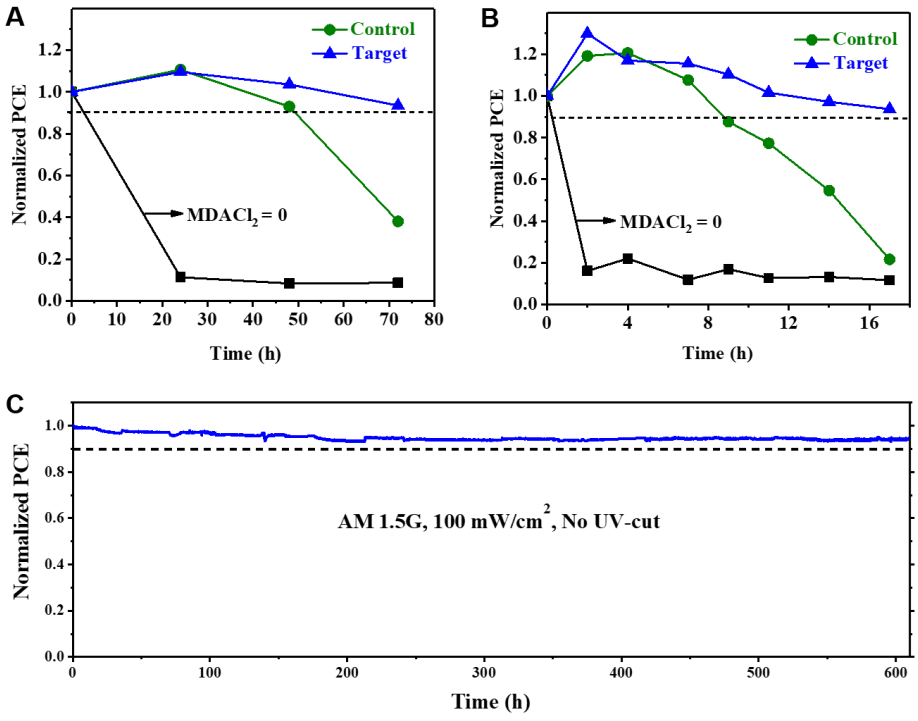

Fig. 3.11 Long-term stability test. Comparison of **(A)** humidity (85% relative humidity (RH), 25°C) and **(B)** thermal (150°C, at ~ 25% RH) stability performances of unencapsulated control and target. **(C)** Maximum power point tracking measured with the encapsulated target device under full solar illumination (AM 1.5G, 100 mW/cm^2 in ambient condition.) without a UV-filter.

We compared the long-term humidity, thermal-, and photo-stability performances of the unencapsulated control and target in **Fig. 3.11**. We used copper phthalocyanine (CuPC) as the hole-transporting material (HTM) to prevent degradation by hygroscopic dopants and spiro-OMeTAD itself at 150°C. The target device exhibited higher humidity stability, retaining > 90% of the initial PCE after 70 h under high humidity (85% relative humidity (RH), 25°C), than the control PCE that reduced to 40% of the initial value **(Fig. 3.11A)**. The thermal stability monitored at 150 °C, at ~ 25% RH **(Fig. 3.11B)** indicates that the control device PCE degraded gradually, reaching <20% of the initial PCE after 17 h, because of MA evaporation. The target device maintained >90% of its initial PCE and exhibited greatly improved thermal stability. In addition, the long-term photo-stability (encapsulation and ambient condition) of the PSC including spiro-OMeTAD as HTM was tested with maximum power point tracking (MPPT) under full solar illumination without UV-filter **(Fig. 3.11C)**. Despite the use of TiO_2 photoelectrode with high photocatalytic effect, the target device exhibits very high photo-stability, maintaining around 90% of its initial PCE (>23.0%) over 600 hours of irradiation. This result can be attributed with both the high concentration of Cl ions in the interface between photoelectrode and perovskite,[39] and the stabilization of α-phase on the $FAPbI_3$ by the $MDACl_2$.

3.3 Relieving unwanted strain

3.3.1 Strain of the perovskite layer

The residual strain in halide perovskites substantially affects the performance of the PSCs by reducing structural stability,[40, 41] increasing the carrier mobility,[42] and suppressing atomic vacancies.[43] Lattice strain was directly related to increased defect concentration and nonradiative recombination, which is associated with the efficiency.[44] Huang et al.[45] reported the reduction of residual strain by thermal-annealing of perovskite films produced by a solution process enhanced the intrinsic stability of the films under illumination by decreasing ion migration. Chen et al.[46] demonstrated that α-$FAPbI_3$ can be stabilized by growing a single crystal on the substrate, and the bandgap and hole mobility also changed when a compressive strain was applied.

Alloyed mixed halide perovskite are non-uniform because of the phase separation through segregation of ions, which causes local lattice mismatch and leads to residual deformation. The efficiency was increased by improving carrier transport and extraction at the interface of the perovskite absorber and hole transport material (HTM) by controlling the vertically strained gradient with flipped annealing method.[46] Xue et al.[47] observed that the stability considerably improved with added compressive strain by using an HTM with a high coefficient of thermal expansion for the perovskite film. Tsai et al.[48] reported improved PSC device performance under continuous light illumination because of the uniform lattice expansion in the perovskite film.

The strain in APbI3 perovskite can also be reduced by substituting some of the Pb^{2+} ions with iso-valent Cd^{2+} ions of a small ionic radius.[43, 49] As a result, both the efficiency and stability improved with the relaxation of the local lattice strain. Similarly, it was shown for mixed $(FASnI_3)_{0.5}(MAPbI_3)_{0.5}$ PSCs, the addition of 2.5 mol% of Cs^+ ions led to the relaxation of the lattice strain, resulting in a lower concentration of defects, which in turn improved efficiency.[50] Therefore, the strain engineering of lead halide perovskites has attracted attention as a method to further improve both the efficiency and stability of PSCs.

To further progress, we modified our composition.[51] Compared with stabilizing α-phase by adding MA^+ or Cs^+ (which have a smaller ionic radius than FA^+), the change in the bandgap is very small, and a high short-circuit current (J_{sc}) was obtained with relatively better stability. Nevertheless, substituting only MDA^{2+} cations with a larger ionic radius **(Fig. 3.12)** or Cs^+ smaller ionic radius than FA^+ can distort Pb-I-Pb bonds by tilting the PbI_6 octahedron. One of the most common strain compensation strategies is to introduce larger and smaller ions together to reduce the local tensile and compressive strain in the perovskite lattice.

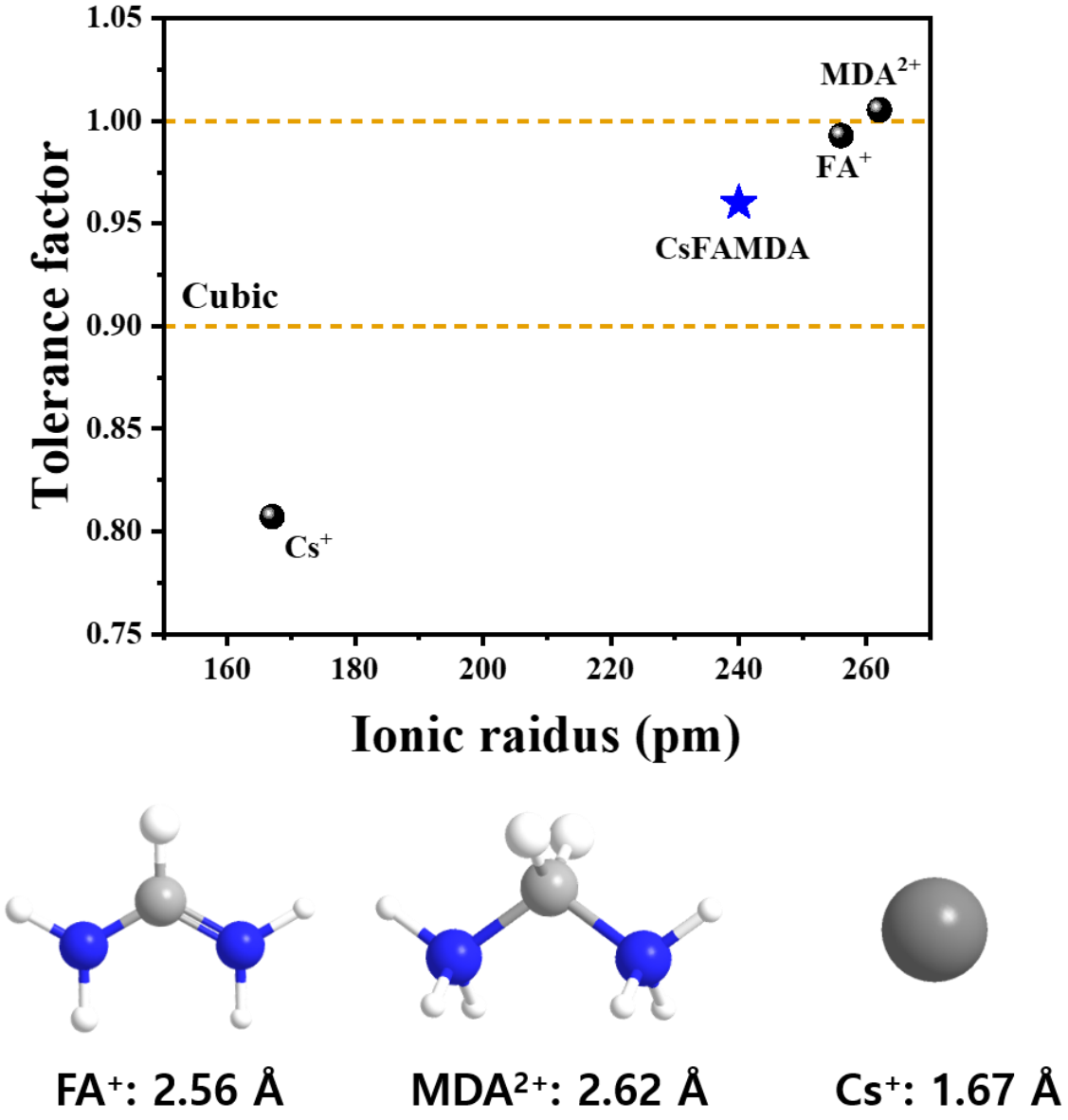

Fig. 3.12 Ionic radius of FA^{+}, MDA^{2+}, and Cs^{+}, and corresponding tolerance factor of $APbI_3$.

3.3.2 Results

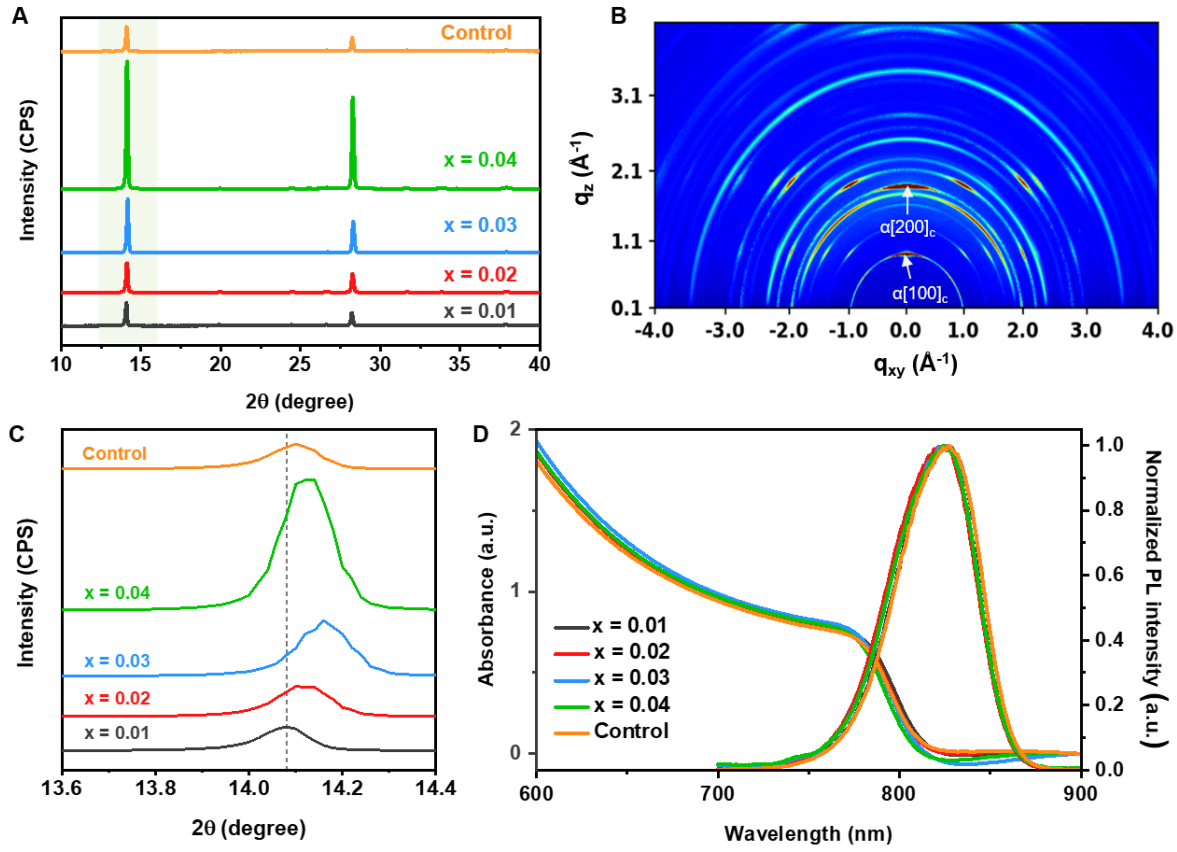

Fig. 3.13 Characterization of perovskite thin films deposited on mp-TiO_2 for the (xMC/$FAPbI_3$) and control perovskite films. (A) XRD patterns of perovskite film, (B) GIWAXS for x = 0.04, (C) magnified (100) diffraction peaks in the region indicated by the green in (A), and (D) UV-vis absorption and normalized PL spectra.

The xMC/$FAPbI_3$ (x = 0.01, 0.02, 0.03, and 0.04 mole fraction) perovskite thin films were deposited by our solvent engineering process[34, 51, 52] using precursor solutions that dissolved the FAI and PbI_2 with the desired number of MDA^{2+} and Cs^+ cations. Here, MC is an abbreviation that means that MDA^{2+} and Cs^+ were mixed in the equimolar amount (e.g., MDA: Cs = 1:1). **Fig. 3.13A** shows the XRD patterns of the samples with different x values for the perovskite thin layers prepared directly on mesoporous-TiO_2 (mp-TiO_2) electron-transporting layer. In the XRD patterns, two dominant peaks could be seen at approximately 14° and 28°, which we assigned to the characteristic (001) and (002) crystal planes of the α-$FAPbI_3$ phase, while no δ-phase appeared at 11.6°.

Interestingly, the diffraction intensity of the two peaks increased, and no new peaks appeared, as x increased. Because crystallographic data usually measured from one-dimensional XRD only provides limited structural information, particularly for highly oriented perovskite films, we obtained two-dimensional grazing-incidence wide-angle x-ray scattering (GIWAXS) patterns to probe changes in the crystallographic orientations of the perovskite film with x. Distinct and relatively strong spots were observed in the ring patterns **(Fig. 3.14A)** as x increased (i.e., increased substitution). The GIWAXS patterns for x = 0.04 **(Fig. 3.13B)**, exhibited a strong diffraction intensity and was similar to x = 0.03 (Fig. S1C), but had slightly greater intensity and appeared more clearly as a mixture of scattered secondary spots and rings. The preferential crystal orientations for α-$FAPbI_3$ were observed out of the plane in the direction $[100]_c$ and $[200]_c$. We concluded that the diffraction intensity increased with increasing x because of the highly oriented crystal domains, and not the improvements in the crystallinity.

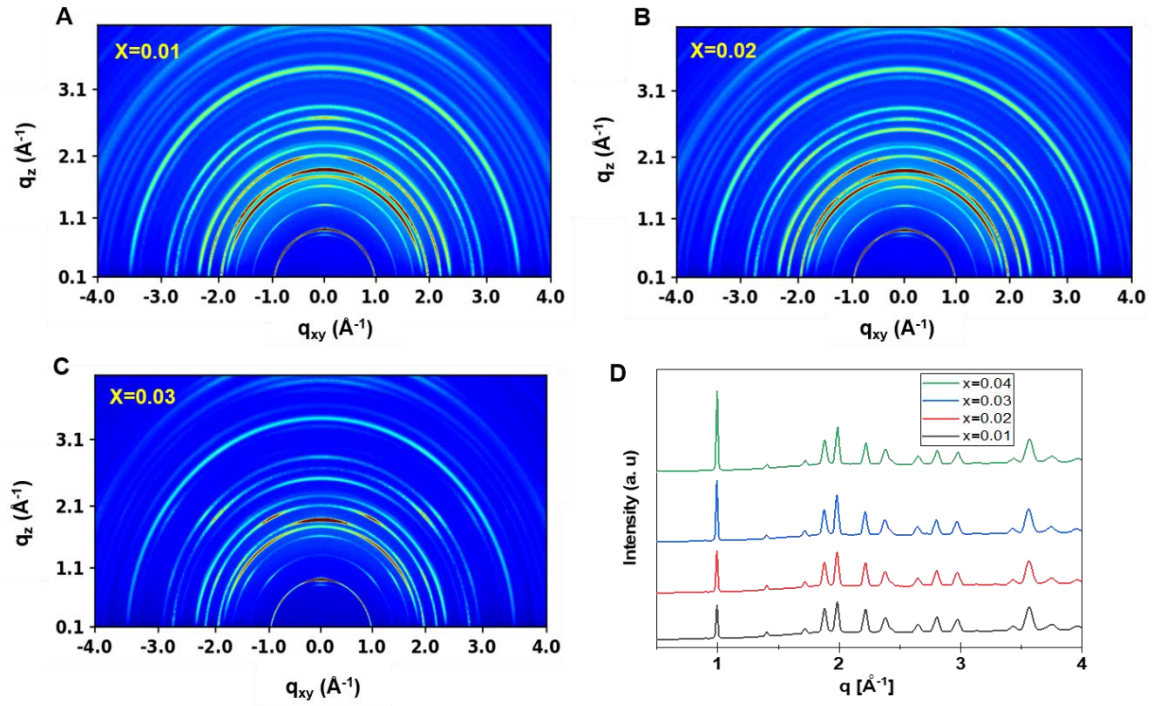

Fig. 3.14 (A)-(C) GIWAXS patterns of thin layers deposited on mp-TiO_2 electrode with different x values in (xMC/$FAPbI_3$) (MC is an abbreviation that means that MDA^{2+} and Cs^+ are mixed in the equimolar fraction) **(D)** Azimuthal circular average fitted from GIWAXS 1D spectra.

In addition, compared with 0.038MDA/$FAPbI_3$ *(denoted as control)*, the peak position at ~14° gradually shifted to higher angles from 14.07° to 14.16° as x increased until x = 0.03, then it slightly decreased to 14.12° at x = 0.04 (Fig. 1C). In the same crystal, because the diffraction angle (2θ) reflected the expansion and contraction of the lattice, the diffraction angle could shift depending on the proportion

of the relatively smaller Cs^+ and larger MDA^{2+} cations to the FA^+ cations. This result suggested that the incorporation of Cs^+ and MDA^{2+} into the lattice of $FAPbI_3$ formed solid-state alloy.

Inferring the deviation from this trend at x = 0.04, we expected the composition of the actual perovskite thin film to differ slightly from the composition of the precursor solution. Nevertheless, the change in optical properties with x was negligible. In **Fig. 3.13D**, UV-vis absorption spectra and normalized PL data with different x mole fraction in $xMC/FAPbI_3$ and control are compared. A slight blue-shift was observed in the absorption onset as x increased, however, the shift was very small compared with the composition in which a single Cs^+ cation is added to pure $FAPbI_3$.[31] The corresponding shifts are consistent with the PL emission peaks from of 826, 825, 825, and 824, and 827 nm for x = 0.01, 0.02, 0.03, 0.04 and the control, respectively.

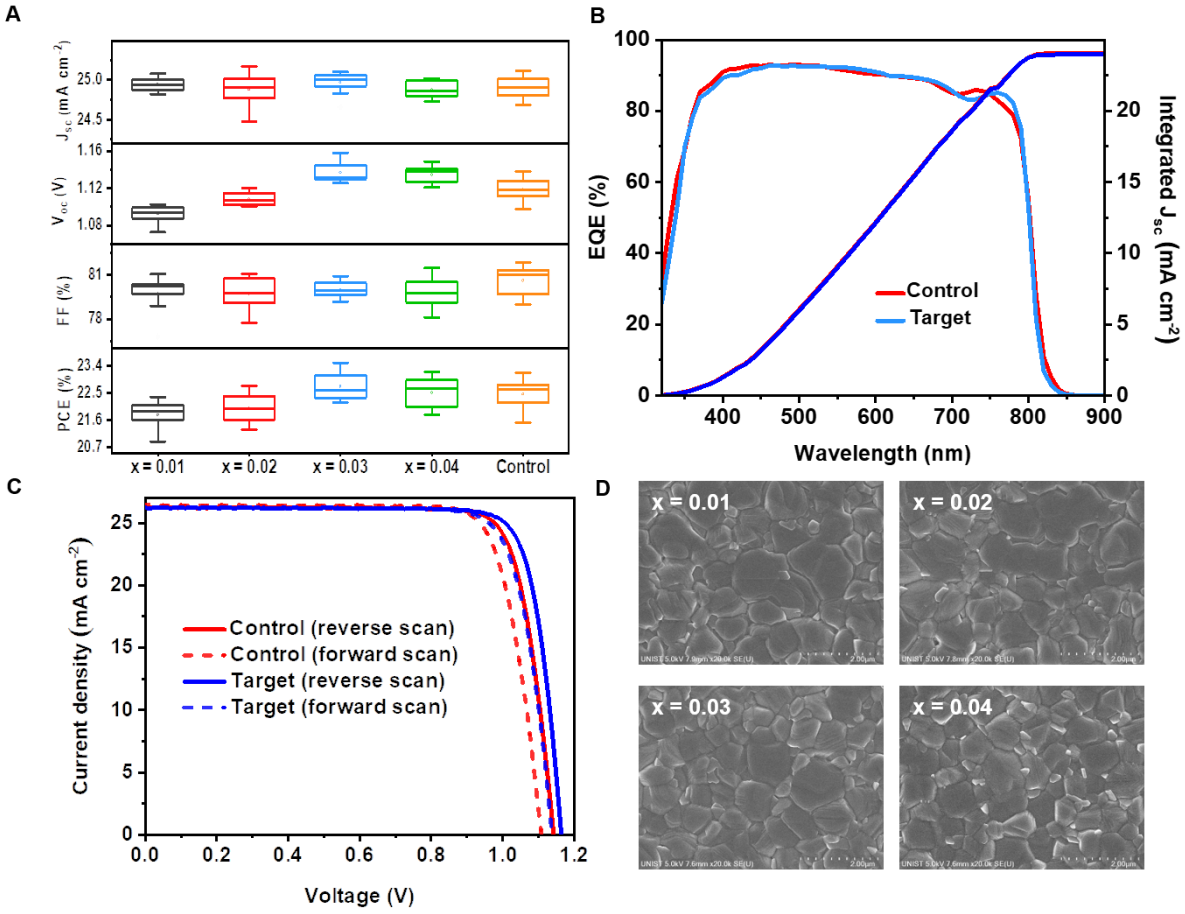

Fig. 3.15 Performance and surface morphologies of PSCs fabricated with x in ($xMC/FAPbI_3$) and control perovskite films. **(A)** J_{sc}, V_{oc}, FF, and PCE statistics of 24 PSCs, **(B)** EQE curves of target and control PSCs, **(C)** J–V curves of target and control PSCs, and **(D)** surface SEM images of perovskite thin layers.

Fig. 3.15 shows the variation in solar cell characteristics with different x in xMC/$FAPbI_3$ (x = 0.01, 0.02, 0.03, and 0.04 mole fraction) and control. The devices comprised multiple layers, glass/fluorine doped tin oxide (FTO)/compact-TiO_2/thin mp-TiO_2/perovskite/2,2',7,7'-Tetrakis[N,N-di(4-methoxyphenyl)amino]-9,9'-spirobifluorene (Spiro-OMeTAD)/Au. To confirm the effect of co-substitution of MDA^{2+} and Cs^+ on solar cell performance, at least 24 devices in each category were fabricated and evaluated in one experiment **(Fig. 3.15A)**. The statistical distribution of factors such as J_{sc}, open-circuit voltage (V_{oc}), and fill factor (FF) determining power conversion efficiency (PCE) showed that a relatively better performance was noticed for x = 0.03 *(denoted as target)* with a narrow distribution of J_{sc}, V_{oc}, FF, and PCE and an average PCE of 22.72 ± 0.45%.

In general, when the composition or coating process of the perovskite thin film is changed, the surface morphology may change and in turn change the efficiency. Thus, we imaged the surface morphology with the x in xMC/$FAPbI_3$ (x = 0.01, 0.02, 0.03, and 0.04 mole fraction) and the control films by top-view SEM images **(Fig. 3.15D)**. Regardless of the amounts of additives, all films showed a similar grain size without apparent pinholes on the surface. These results indicate that the incorporation with small amounts of Cs^+ and MDA^{2+} cations did not affect the morphological features of the perovskite layers, such as grain sizes and surface roughness.

For simplicity, the control and target were compared to find out why the efficiency improved by substituting the same amount of Cs^+ and MDA^{2+} in $FAPbI_3$. **Fig. 3.15B** shows the external quantum efficiency (EQE) spectra for one of the representative control and target devices. The EQE onset of the target is slightly blue-shifted, which was consistent with the tuned bandgap **(Fig. 3.13D)**. Nevertheless, as can be seen in the integrated J_{sc} **(Fig 3.15B)**, this small blue shift in the bandgap was not appreciable. The similarities in J_{sc} implied that there was no substantial difference in the charge collection in the two comparison groups.

The J-V characteristics of the best-performing control and target devices in a reverse and forward bias sweep with antireflective coatings on the device surface are compared in **Fig. 3.15C**. The J_{sc}, V_{oc}, and FF values calculated from the J-V curve of the target were 26.23 mA cm^{-2}, 1.168 V, and 82.15%, respectively; these factors correspond to a PCE of 25.17 % under standard air mass (AM) 1.5 conditions, whereas the control exhibited a PCE of 24.48 % with J_{sc} = 26.25 mA cm^{-2}, V_{oc} = 1.138 V, and FF = 81.95%. The PCE of the target devices shown in **Fig. 3.15C** was certified by an accredited laboratory (Newport, USA) using quasi-steady-state (QSS) method. The stabilized PCE measured by QSS was 24.37% with J_{sc} = 26.17 mA cm^{-2}, V_{oc} = 1.162 V, and FF = 80.13% for the small cell **(Fig. 3.16A)**, and 21.63% for the large cell (1x1 cm^2, **Fig. 3.16B**). Within the scope of this study, the effect of compositional changes on J_{sc} was very limited, and most efficiency improvements were from an

increase in V_{oc}. As noted earlier, because control and target devices have almost the same bandgap, surface morphology, and thickness, the large increase in V_{oc} (low V_{oc} loss) arose from the changes inside the crystalline perovskites. The V_{oc} loss for x and control occurred at x = 0.03.

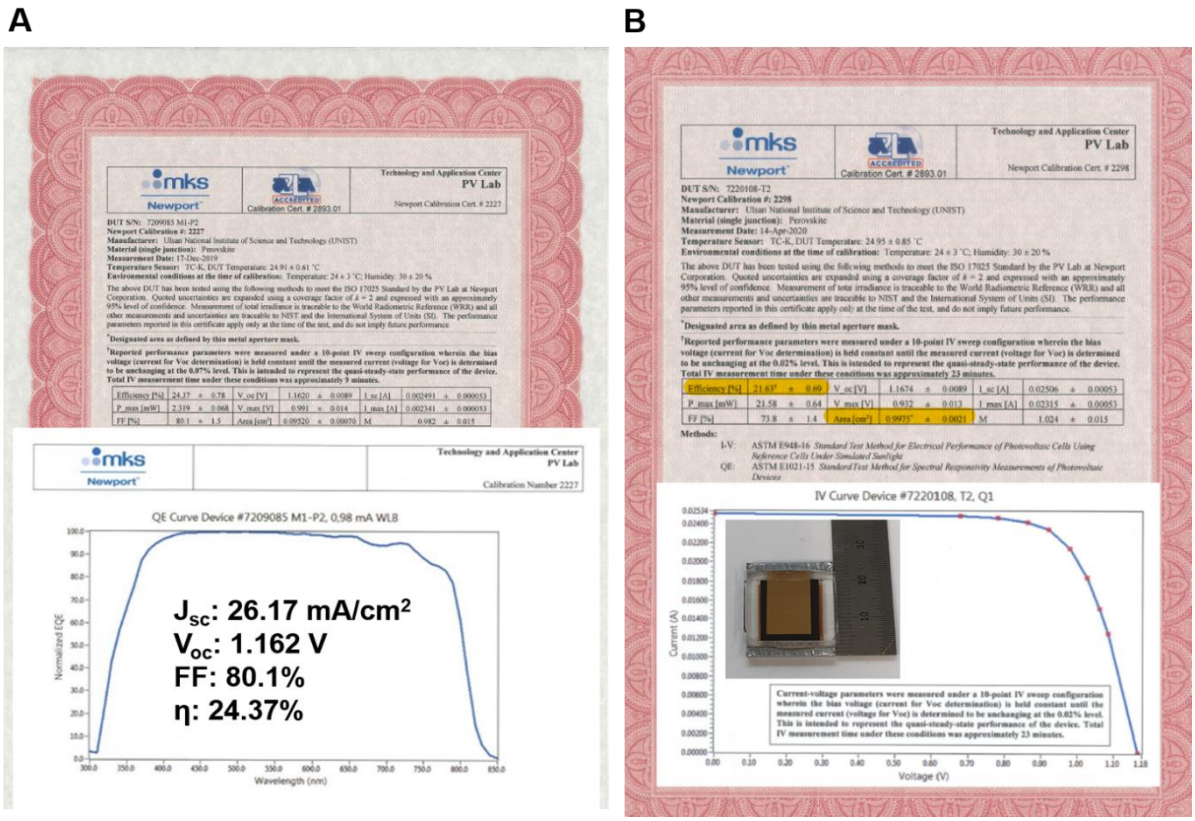

Fig. 3.16 Certified result from accredited photovoltaic certification laboratory (Newport, USA) for **(A)** the small unit device and **(B)** large device (1x1 cm^2).

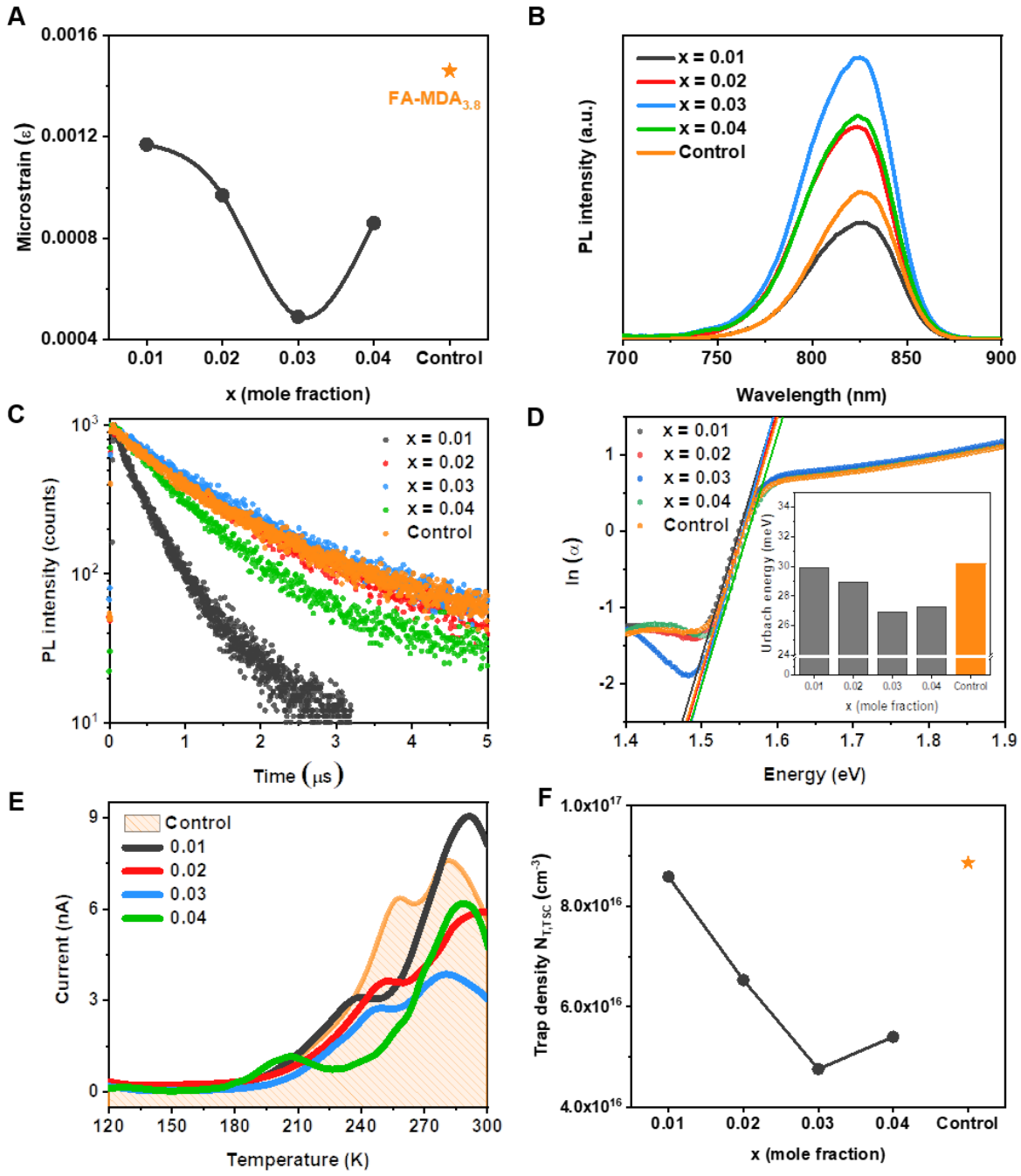

Fig. 3.17 Defect analysis of perovskite films deposited with x in (xMC/FAPbI$_3$) and control. (A) Residual strain calculated in perovskites consisting of FTO/mp-TiO$_2$/perovskite. **(B)** Steady-state photoluminescence and **(C)** time-resolved photoluminescence spectra of films deposited on glass. **(D)** Urbach energy calculated in perovskites consisting of FTO/mp-TiO$_2$/perovskite, **(E)** thermally stimulated current spectra, and **(F)** trap density.

Generally, V_{oc}-loss is directly related to reduction in defect concentration and nonradiative losses.[53, 54] In this regard, there have been many reports that lattice strain in perovskites increases defect concentrations and nonradiative recombination.[55] We estimated the variation in lattice strain of perovskite films with x in xMC/$FAPbI_3$ using the Williamson−Hall (WH) plot (individual plots with x are displayed in **Fig. 3.18**) from the XRD patterns of **Fig. 3.13A**. As can be seen in **Fig. 3.17A**, the strain decreased as x increased from 0.01 to 0.03, and then increased again at 0.04. Here, WH method considers the broadening of the peak as a function of the diffraction angle, which is assumed to be the combined effect of broadening induced by both the crystalline size and strain.[56] Furthermore, the strain of perovskite films can also be attributed from the preferred crystalline phase and oriented domain boundaries etc. When the mole fraction of MDA and Cs incorporated in $FAPbI_3$ was 3:3, the lowest strain appeared. This result proposes that 3:3 substitution of Cs^+ and MDA^{2+} in $FAPbI_3$ effectively mitigated the lattice strain in the perovskite structure **(Fig. 3.19)**. Thus, reducing the strain of the lattice minimized defect centers or traps that can capture charge carriers and negatively impact solar cell performance.

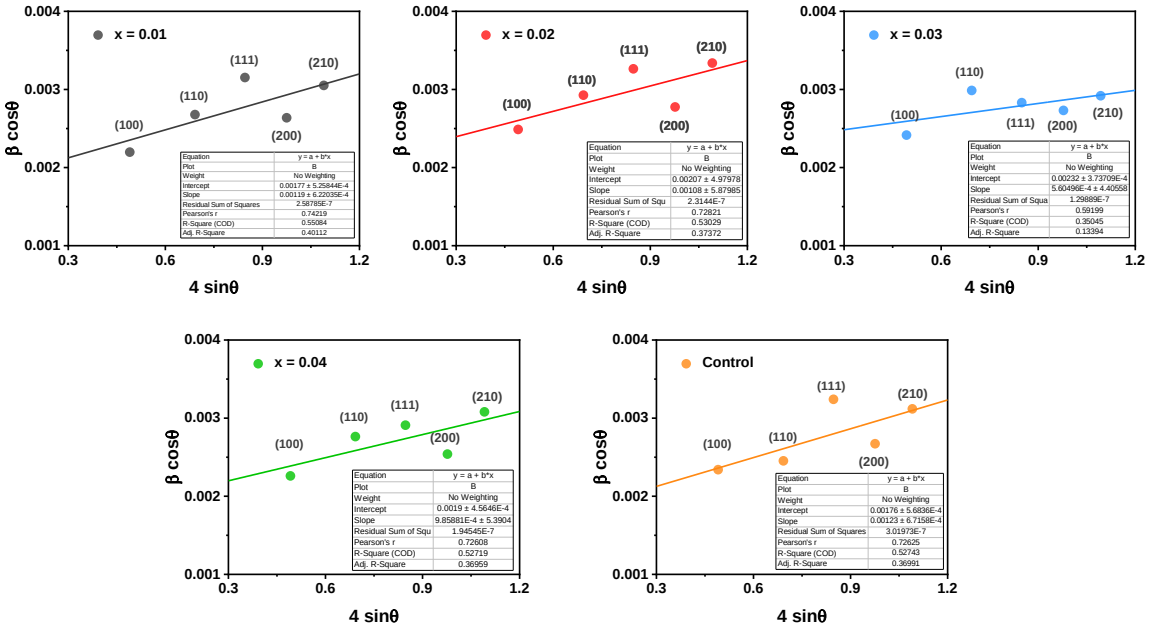

Fig. 3.18 Williamson−Hall plots with different x values in (xMC/$FAPbI_3$) (here MC is an abbreviation that means that MDA^{2+} and Cs^+ are mixed in the equimolar fraction) and control.

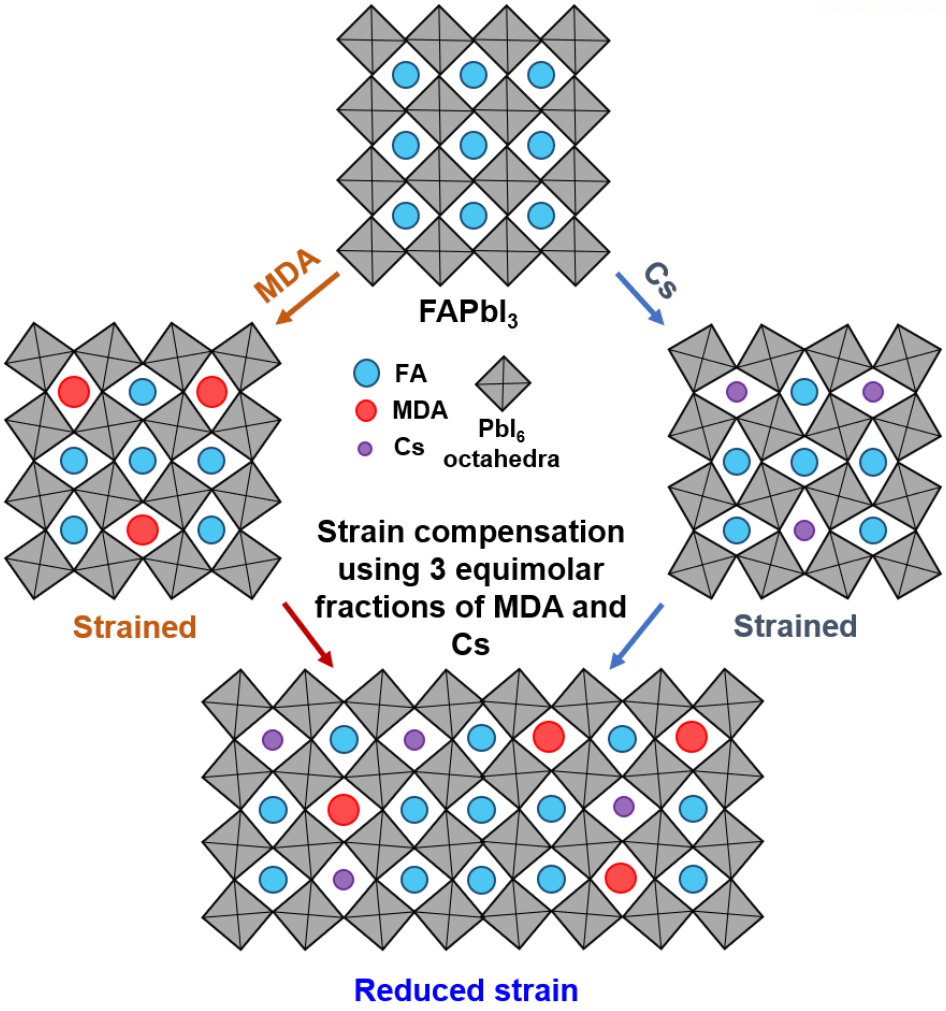

Fig. 3.19 Schematic illustration of the proposed distribution by incorporating the 3:3 equimolar faction of MDA and Cs cations within the perovskite crystal for compensating the lattice strain induced by difference between the radius of FA, MDA and Cs.

Steady-state PL and time-resolved photoluminescence (TRPL) measurements were carried out to investigate the nonradiative carrier recombination of the perovskite thin films with different x (xMC/$FAPbI_3$) and control. **Fig. 3.17B** displays PL spectra for the thin perovskite layers deposited on glass substrate. The addition of equal amounts of Cs^+ and MDA^{2+} increased the PL intensity; the intensity maximized at x = 0.03 and then decreased again at x = 0.04. Under the same conditions, an increase in PL intensity implied a decrease in non-radioactive recombination. For a more quantitative comparison of charge recombination, TRPL was measured using time-correlated single photon counting (TCSPC) under low-intensity pulsed excitation, for which decay dynamics mostly reflect nonradiative trap-assisted recombination. From the PL decay curves in **Fig. 3.17C**, the carrier lifetime values were obtained by using the following biexponential equation: $Y = A_1\exp(-t/\tau_1) + A_2\exp(-t/\tau_2)$, where τ_1 and τ_2

denote the fast and slow decay time and are related to the trap-assisted non-radiative recombination processes and radiative, respectively. Both τ_1 and τ_2 at x = 0.03 are the longest, including control. This increased lifetime was consistent with the reduction of lattice strain, indicating that the relaxation of the strain suppressed nonradiative recombination by reducing the number of trap states.

Changes in the lattice strain can also affect the Urbach energy (E_u). A lower E_u of the perovskite film indicates a higher structural quality of the film, as well as a lower voltage loss between V_{oc} and the bandgap voltage**. Fig. 3.17D** shows E_u for the perovskite films calculated from UV-vis absorption spectra with the following equation: $\alpha = \alpha_0 \exp(h\nu/E_u)$, where α is absorption coefficient and $h\nu$ is photon energy. The E_u of the control and target films were 30.18 and 26.88 meV, respectively **(Fig. 3.17D)**. Interestingly, the change in E_u of $FA_{1-3x}MC_xPbI_3$ perovskite films shows a similar trend with the change in the micro-strain of the films. This result implies that the lattice strain is closely related to the trap states in the perovskite films.

To further understand the total quantity and energetic levels of the trap states, thermally stimulated current (TSC) analysis was performed in complete devices. **Fig. 3.17E** presents the TSC spectra for temperatures from 120 to 300 K for ($xMC/FAPbI_3$) (x = 0.01, 0.02, 0.03, and 0.04 mole fraction)-based PSCs compared with the control device. The TSC signal could be integrated to estimate the lower limit of trap densities over the elapsed time according to the equation:

$$\int_{signal} I_{TSC} dt \leq eN_{T,TSC}Vol$$

where $N_{T,TSC}$ is the trap density, e is the elementary charge, and Vol is the volume of the perovskite layer [57, 58]. The trap density, $N_{T,TSC}$ of the control device (8.86×10^{16} cm^{-3}) was the highest, which indicates that the strain in the perovskite structure induced an increase in defects. The trap density decreases in the ($xMC/FAPbI_3$) devices from x = 0.01 to x = 0.03, where it was smallest (4.76×10^{16} cm^{-3}), and then increased at x = 4 **(Fig. 3.17F)**.

To extract the activation energy of the trap states, the slope of the initial rise of the TSC current, which was attributed to the start of trap release, in the Arrhenius plot for each condition was fitted to the following equation:

$$I_{TSC} \propto exp\left(-\frac{E_A}{k_B T}\right)$$

where E_A, k_B, and T are the activation energy, Boltzmann constant, and temperature, respectively.[59] For the control device, trap states with an activation energy E_{A1} = 150 meV were estimated **(Fig. 3.20)**. For

x = 0.01, a higher activation energy (224 meV) was observed, but it was remarkably reduced at x = 0.02 (131 meV) and x = 0.03 (130 meV), and then rapidly increased to 272 meV at x = 0.04. A higher activation energy indicates traps formed deeper in the bandgap, which promotes nonradiative recombination. At very low temperatures < 250 K, the activation energy E_{A2} of x = 0.03 (169 meV) was slightly lower than that of the control (183 meV); however, it is speculated that the E_{A1} value is more critical to real operational conditions, which are greater than room temperature (298 K). The defect analysis, PL, TCSPC, Urbach energy, and TSC results were in good agreement with the changes in the lattice strain of the (xMC/$FAPbI_3$) (x = 0.01, 0.02, 0.03, and 0.04 mole fraction) perovskites, which implies that the enhanced device performance with improved V_{oc} was closely related to defect passivation induced by the strain relaxation of the perovskite structure.

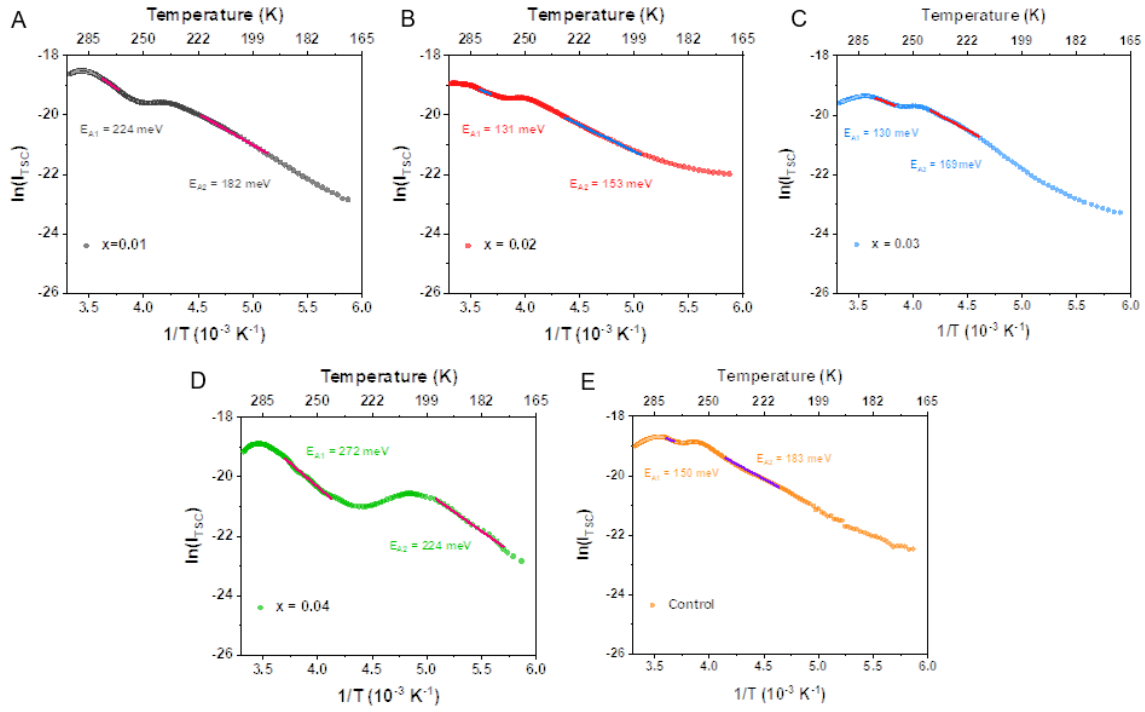

Fig. 3.20 Arrhenius plot with different x values in (xMC/$FAPbI_3$) (here MC is an abbreviation that means that MDA^{2+} and Cs^+ are mixed in the equimolar fraction).

3.4 Conclusion

In the primary work, we proposed and evaluated a novel type of phase-pure α-$FAPbI_3$ perovskite for solar cell operation via incorporating a small amount of $MDACl_2$ into $FAPbI_3$. The divalent cation MDA stabilizes the phase of $FAPbI_3$ with negligible bandgap tuning, which affords unprecedented J_{SC} values in the $FAPbI_3$ devices, which in turn exhibit superior humidity and thermal stability performances relative to our control sample ($FAPbI_3$ stabilized by $MAPbBr_3$). As a result, we were able to fabricate solar-cell devices with efficiencies >24% (certified stabilized efficiency of 23.7%) exhibiting stable high-humidity operation and good thermal stability (retention of more than 90% of the initial PCE after 70 h exposure to high humidity (85% RH and 25 °C) after annealing at 150 °C for 20 h). The origin of both the PCE and stability improvements upon the addition of a suitable amount of $MDACl_2$ can be attributed to (i) increased α-phase stability due to an increase in the numbers and strength of intermolecular N−H···I hydrogen bonds between divalent MDA and the Pb−I lattice, (ii) reduction in lattice strain reflected by the change in the Goldschmidt tolerance factor because of the presence of vacant FA cations, and (iii) increased thermal stability due to the presence of smaller interstitial Cl^- ions in the $FAPbI_3$ lattice.

For further progress, we modified our composition via doping of small amount of Cs^+ ion to the MDA doped $FAPbI_3$. We incorporated the same molar ratio of two cations (Cs^+ and MDA^{2+}) to stabilize the α-phase of the $FAPbI_3$ perovskite. The optimized amount of Cs^+ and MDA^{2+} reduced the lattice strain and trap densities, which resulted in enhanced V_{oc} and reproducible PCEs. The best performing PSC showed a PCE > 25% (24.4% certified) for the small device. In addition, the relatively uniform and low strain perovskite film made it possible to achieve the highest reported efficiency of 21.63% PCE over a large area (1x1 cm^2). Unencapsulated devices retained 90% of their initial efficiency after 1000 h under ambient conditions.

Chapter 4. Wide-bandgap Perovskites

4.1 Candidates for wide-bandgap perovskites

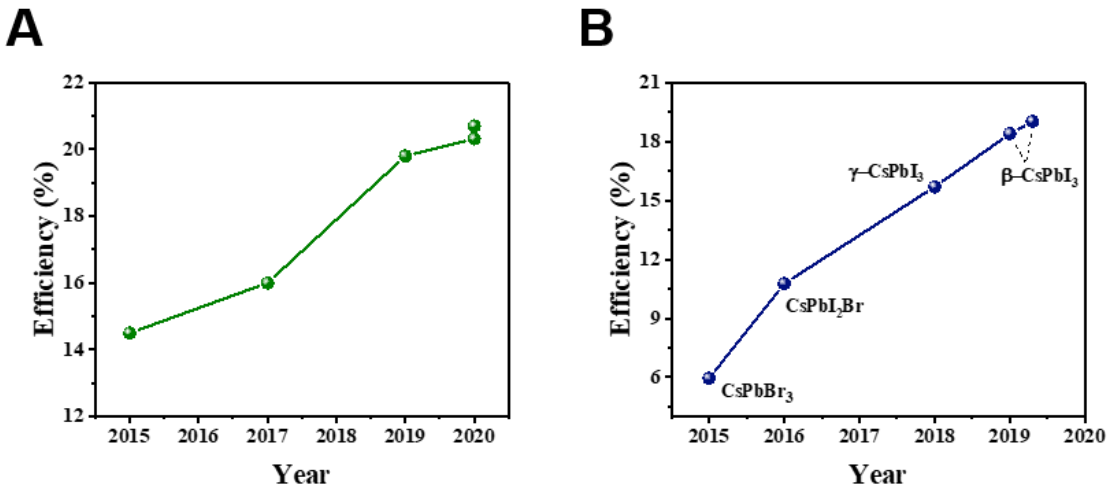

Fig. 4.1 Efficiency increases of **(A)** mixed-halide wide-bandgap perovskites (MHWPs) and **(B)** inorganic perovskites.

Wide-bandgap perovskites with bandgaps in the range from 1.65 eV–1.75 eV are used in tandem with silicon (Si)[25] or low-bandgap perovskites-based solar cells.[60] State-of-the-art wide-bandgap perovskites can be classified as mixed-halide wide-bandgap perovskites (MHWPs)[61, 62] and all-inorganic perovskites.[63] The power conversion efficiency (PCE) of MHWPs with Br/I-alloyed bandgaps is relatively high; however, halide segregation owing to the Br-I mixture tends to cause poor photostability.[64] Furthermore, state-of-the-art levels of MHWPs show increased photo stability with over 20%. Kim et al.[65] achieved a PCE of 20.7% by anion-engineering the composition of the $(FA_{0.65}MA_{0.2}Cs_{0.15})Pb(I_{0.8}Br_{0.2})_3$ perovskite (FA and MA denote formamidinium and methylammonium, respectively) and Xu et al.[62] achieved a PCE of 20.3% using Cl^- ion doping via the addition of $MAPbCl_3$ to the $FA_{0.75}Cs_{0.25}Pb(I_{0.8}Br_{0.2})_3$ perovskite.[66] However, these perovskites contained considerable amounts of MA^+ cations, which caused poor thermal stability, and still lack of operational stability data under full sunlight irradiation.

As an alternative to MHWPs, all-inorganic cesium lead triiodide ($CsPbI_3$) has recently attracted the attention of researchers owing to its high thermal stability, lack of halide segregation, anti-solvent free synthesis process, and high potential possibilities for efficiency improvement **(Fig. 4.1)**. $CsPbI_3$ presents various phases, such as α, β, γ, and δ, depending on the temperature or experimental conditions used to

fabricate it.[67, 68] Among them, the β-phase presents the suitable bandgap of 1.68–1.70 eV which renders it appropriate for tandem use.[69] Recently, Wang et al.[70] reported the use of dimethylammonium iodide (DMAI) during the relatively low-temperature synthesis of β-$CsPbI_3$ and achieved the high PCE of 19.03% in a dry box under very accurately controlled humidity (<10% RH) conditions. Nevertheless, the thus-obtained $CsPbI_3$ thin film still contained many pinholes and was less efficient than the organic cation-based mixed-halide lead perovskite with similar bandgap. Controlling crystallization process of perovskite materials greatly affects their surface morphology.[71, 72] The solvent-engineering[19] (or anti-solvent) method is the most commonly used approach to obtain highly dense, pinhole-free, and uniform-surface perovskite films. The dropwise addition of anti-solvents, such as toluene, chlorobenzene, and diethyl ether, during spin-coating is widely used despite the difficulties encountered during the practical process. However, even when methyl acetate, which has been reported as an effective anti-solvent for the fabrication of γ-$CsPbI_3$,[73] was used, the resulting performance is still significantly low. Moreover, the use of methyl acetate for the formation of other $CsPbI_3$ phases has not been explored in detail.

4.2 Improving morphology of $CsPbI_3$

4.2.1 Morphologies of $CsPbI_3$

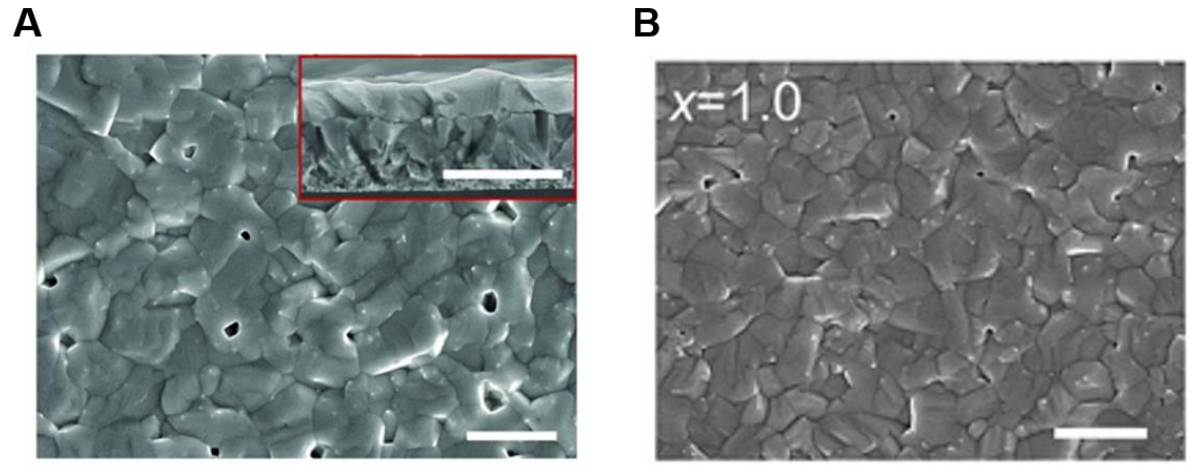

Fig. 4.2 SEM surface morphology images of β-$CsPbI_3$ with efficiency of **(A)** 18.4% *Copyright © 2019, Copyright © 2019 The Authors, some rights reserved; exclusive licensee American Association for the Advancement of Science.* and **(B)** 19.03% *© 2019 Wiley-VCH Verlag GmbH & Co. KGaA, Weinheim*

Recently efficiency of β-$CsPbI_3$ is increased rapidly reaching ~19%. Despite relatively high efficiency compared to similar bandgap of MHWPs, the morphology is poor **(Fig. 4.2)**. As, surface morphology of photo-absorbing layer greatly affect photovoltaic performance, to further improvement of efficiency, we need to improve surface morphology without compromising other factors such as bandgap.

Generally, halide PSCs with excellent surface morphology and remarkable crystallinity can be obtained by fine-tuning the intermediate state before high temperature annealing for crystallization. Therefore, not only the formation but also the removal of the intermediate phase at the appropriate time is considered critical for obtaining uniform and dense perovskite layers, particularly when anti-solvents are not used. Studies on the use of additives, such as acids,[74, 75] polymers,[76, 77] metal or organic halide salts,[78] and two-dimensional (2D) materials[29] for triggering changes in the intermediate phase have been conducted recently or are in progress. The effect of methylammonium chloride (MACl) on the intermediate phases of perovskite materials of various compositions is complex; however, typically, the use of MACl during the synthesis of perovskite films results in films with superior quality.[79, 80] Moreover, several research groups fabricated compact and uniform perovskite layers using anti-solvent-free approaches utilizing MACl. Fengxian et al.[81] induced homogeneous and vertical recrystallization by depositing MACl on a δ-$FAPbI_3$ layer, and Wang et al.[82] prepared monolayer-like perovskite films using the combined coordination effects of MACl with of methylammonium acetate and PbI_2 in the absence of anti-solvents. Xu et al.[83] added HI to the reaction mixture 2D-to-three-dimensional (3D) conversion of perovskites and obtained uniform and highly compact perovskite layers without using anti-solvents. In addition to the formation of halide perovskite thin films with uniform and dense surfaces, surface passivation has been demonstrated to be an important strategy for the fabrication of efficient and stable perovskite solar cells.

4.2.2 Results

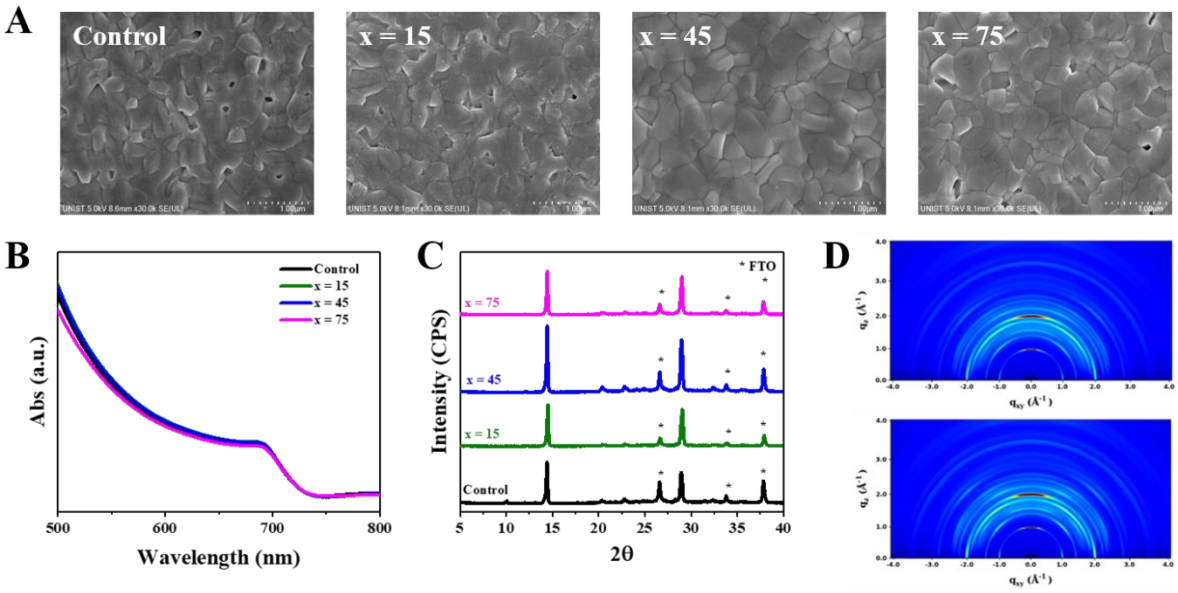

Fig. 4.3 Characterization of $CsPbI_3$ films without (control) and with MACl second treatment according to the concentration of MACl (15, 45, and 75 mM) in IPA. **(A)** SEM images, **(B)** UV-vis absorption spectra, **(C)** XRD patterns, and **(D)** GIWAXS of $CsPbI_3$ layer with (above) without (below) MACl second treatment.

$CsPbI_3$ perovskite thin films *(hereinafter referred to as the control)* were deposited under ambient-air conditions with the relative humidity (RH) 15 % to 30 % utilizing the same method used to fabricate the state-of-the-art β-$CsPbI_3$ perovskite.[69] As reported by Wang et al.[69] and illustrated by the top-view scanning electron microscopy (SEM) images of the control **(Fig. 4.3A)**, the thus obtained thin film presented poor surface morphology with multiple pinholes.

Thus, we attempted to enhance the properties of this thin film by introducing MACl into it using the "sequential dripping of MACl solution" *(denoted as SDMS)* method, which is illustrated in **Fig. 4.4A**. This method was adopted because the solubility of MACl in the CsI-, PbI_2-, and DMAI-containing perovskite precursor solution was considerably low. The highest concentration of MACl in the perovskite precursor solution was 30 mM, and the solution became cloudy when the concentration of MACl exceeded 45 mM **(Fig. 4.4B)**. However, MACl dissolved well in isopropyl alcohol (IPA) at concentrations up to 135 mM, and the solution became slightly cloudy at the concentration of 180 mM **(Fig. 4.4C)**.

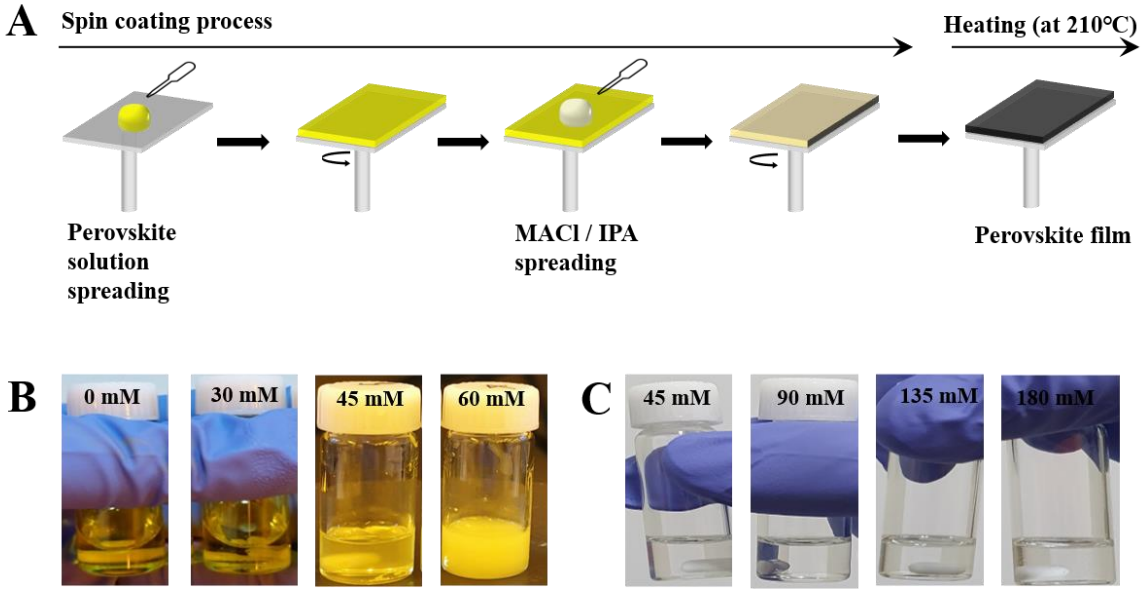

Fig. 4.4 (A) Schematic diagram of SDMS. Solubility of **(B)** MACl in $CsPbI_3$ precursor solution and **(C)** MACl in IPA.

Subsequently, we determined whether the SDMS method modified the bandgap of $CsPbI_3$ using 15, 45, and 75 mM MACl solutions in IPA, and the obtained specimens were labelled $CsPbI_3$/xMACl (x = 15, 45, and 75 mM). The UV–vis absorption spectra **(Fig. 4.3B)** of the control and $CsPbI_3$/xMACl samples confirmed that the bandgap of $CsPbI_3$ was not changed by the SDMS, probably owing to the complete removal of MACl after 5 min of heat treatment at 210 °C. The absorption edges of the control and $CsPbI_3$/xMACl were located at approximately 730 nm, and this value was consistent with the theoretically simulated bandgap of β-$CsPbI_3$.[69] The specific peaks of β-$CsPbI_3$ were present in the X-ray diffraction (XRD) patterns of all as-annealed $CsPbI_3$/xMACl film samples **(Fig. 4.3C)**. The characteristic peaks of β-$CsPbI_3$ were present in the XRD patterns of all as-annealed $CsPbI_3$/xMACl film samples **(Fig. 4.3C)**. The crystallinity of $CsPbI_3$/45MACl was slightly higher than those of the other film samples, but still comparable. The structural phases of $CsPbI_3$/45MACl obtained with and without the SDMS and the structures of MACl or other $CsPbI_3$ phases were further characterized using grazing-incidence wide-angle X-ray scattering (GIWAXS). The GIWAXS ring patterns of the (110) and (220) planes of β-$CsPbI_3$[69] were not significantly different **(Fig. 4.3D)**. These results indicated that the SDMS did not change the structure of $CsPbI_3$ and that MACl was fully eliminated during the annealing process, as estimated using the conventional XRD analyses. The SDMS did not affect the crystal structure and bandgap of $CsPbI_3$/xMACl; however, it caused significant changes in the surface morphology of the $CsPbI_3$/xMACl films.

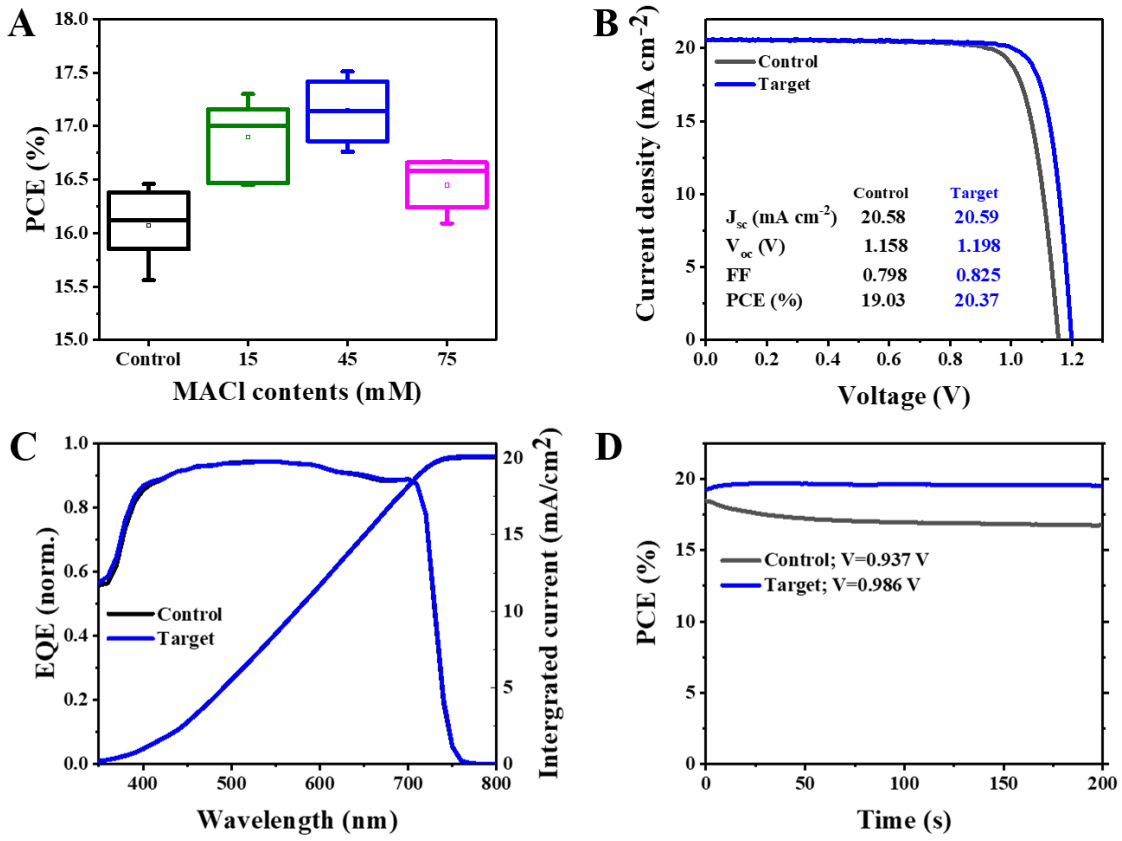

Fig. 4.5 The performance of solar cells. **(A)** PCE distribution of $CsPbI_3$/xMACl (x= 15, 45, and 75 Mm) and the control. **(B)** J-V curves, **(C)** EQE spectra, and **(D)** steady-state power output of the control and target.

The surface morphology of the perovskite layers greatly affects the photovoltaic performance, and particularly the V_{oc} and fill factor (FF). Therefore, we fabricated PSCs to see the effect of this morphology improvement on efficiency. The PSCs comprised multiple layers as follows: glass/fluorine doped tin oxide (FTO)/compact-TiO_2/perovskite/2,2',7,7'-tetrakis[N,N-di(4-methoxyphenyl)amino]-9,9'-spirobifluorene (spiro-OMeTAD)/Au. The PCE distributions of the PSCs fabricated using the control and $CsPbI_3$/xMACl (x = 15, 45, and 75 mM) perovskite films are depicted in **Fig. 4.5A**. The average PCEs of the PSCs fabricated using $CsPbI_3$ and $CsPbI_3$/xMACl perovskites increased from 16.07 ± 0.37% for the control to 16.89 ± 0.23% for $CsPbI_3$/15MACl and 17.15 ± 0.28% for $CsPbI_3$/45MACl.

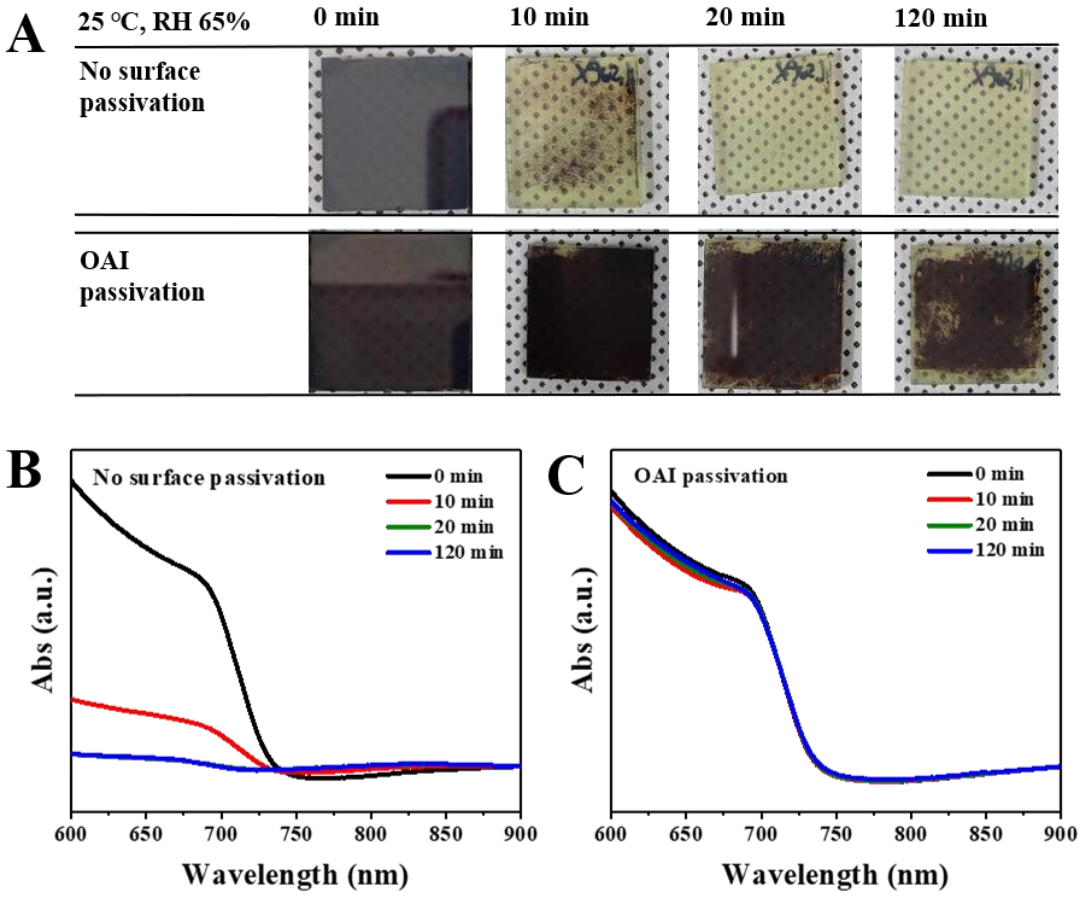

Fig. 4.6 Humidity stability tests at 25 ℃ and RH 65% with and without OAI passivation. **(A)** Photographic images, UV-vis absorption spectra of **(B)** without and **(C)** with OAI passivation.

We have previously reported a relatively stable PSC with the PCE of 22.9%,[84] which was ascribed to the reduced interfacial defects between perovskite and hole-transporting material, and resistance to humidity of octylammonium iodide (OAI). This surface passivation-induced increase in PCE can be used for $CsPbI_3$-[69, 85] and $FAPbI_3$-based systems.[22, 84] We adopted OAI as the surface passivation material owing to its hydrophobicity and positive effect on the PCE of the fabricated PSCs. **Fig. 4.6** depicts the change of photographs and UV–vis absorption spectra the perovskite layer with and without OAI treatment, stored in humid condition (25 °C and RH 65%). The control film was previously reported to be very susceptible to humidity and degraded after 10 min.[69] This fragile stability can negatively affect the efficiency of the fabricated PSCs. By contrast, the control treated with OAI maintained its original absorption for up to 120 min owing to its increased hydrophobicity. As expected, the passivation of the perovskite layer with OAI not only improved the stability but also the performance of the fabricated PSCs. **Fig. 4.5B** illustrates the J–V characteristics of one of the best performing PSCs fabricated using the control and $CsPbI_3$/45MACl perovskite *(hereafter target)*. Surface passivation by

OAI significantly improved the PCE of $CsPbI_3$ regardless of SDMS, as consistent with previously reported results.[84] The J_{sc}, V_{oc}, and FF values calculated from the J–V curves of the target were estimated to be 20.59 mA cm^{-2}, 1.198 V, and 0.825, respectively, and corresponded to a PCE of 20.37% under standard air mass (AM) 1.5 G conditions. In comparison, the PCE, J_{sc}, V_{oc}, and FF of the control were 19.03%, 20.58 mA cm^{-2}, 1.158 V, and 0.798, respectively. This means that although the surface passivation by OAI brought a greater efficiency improvement than SDMS, the effect by SDMS is still very effective. For these champion devices, a large increase in PCE was achieved using the synergism of SDMS and surface passivation, which significantly increased V_{oc}, as expected. However, the best-performing PSC fabricated using a $CsPbI_3$ layer that did not undergo SDMS presented low FF and V_{oc} values, as illustrated in **Fig. 4.5A**. No notable differences were observed in the shapes of the external quantum efficiencies (EQEs) of the control and target **(Fig. 4.5C)**. However, a slight difference between the integrated J_{sc} values of the target (20.12 mA cm^{-2}) and control (20.05 mA cm^{-2}) was observed; this was in agreement with the observed J–V characteristics. The difference between the J_{sc} values of the PSCs obtained using the passivated control and target layers was smaller than that between the J_{sc} values of the PSCs obtained using the control and target in the absence of a passivation layer, and this was ascribed to the improved stability achieved via OAI surface passivation.

We also measured the steady-state power output of one of the best-performing PSCs for 200 s at a set voltage in the vicinity of the MPP obtained from the peak of the J–V curves **(Fig. 4.5D)**. The initial PCE of the PSC featuring the control was 18.46%, which was intermediate between the reverse and forward scan values of the control; however, after 200 s, the PCE decreased to 16.75%. Conversely, the initial PCE of the target was 19.26%, which was the median of the reverse and forward scan values of the target, however, this PCE increased to 19.54% after 200 s. Therefore, the PCE of the PSC featuring the target was more stable than that of the PSC featuring the control.

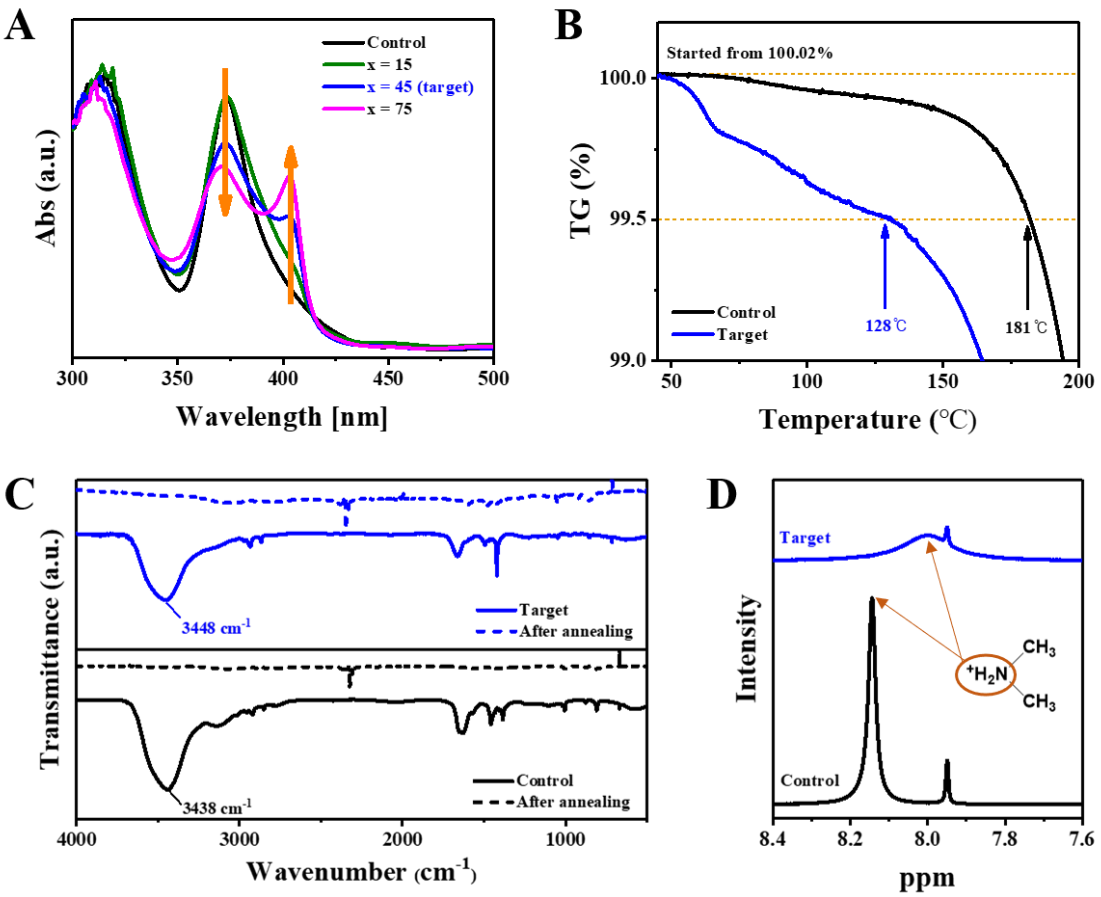

Fig. 4.7 Characterization of intermediate phases. **(A)** UV-vis absorption spectra from as-deposited substrate of $CsPbI_3$/xMACl (x= 15, 45, and 75 mM) and control. **(B)** TGA curves of the control and target. **(C)** FT-IR spectra before (solid line) and after (dotted line) annealing for the control and target. **(D)** H-NMR spectra obtained from intermediate state of the control and target.

To better understand the origin of the improvement induced by the SDMS, we first tested whether the SDMS onto the already-formed $CsPbI_3$ films could positively affect their morphology. The intermediate state affects the formation of the thin film; therefore, the addition of HI to the $CsPbI_3$ precursor solution can significantly lower the annealing temperature α-$CsPbI_3$.[86] $HPbI_3$ was reported to play an important role as the main intermediate state.[87] Hence, to further understand the mechanism behind improving the morphology of perovskites via the SDMS, we focused on the intermediate phase of $CsPbI_3$. To analyze the properties of intermediate state, which is the phase that forms immediately prior to the formation of the $CsPbI_3$ layer, we used UV–vis absorption spectroscopy **(Fig. 4.7A)**. To mimic the environment used during the fabrication of PSCs, we obtained the UV–vis spectra of perovskite films deposited onto FTO/c-TiO_2 substrates. The UV–vis spectrum of the control presented a single peak at approximately 370 nm, which indicated the formation of DMA-Cs-PbI_2 as the intermediate state.[70, 88] However, after

the SDMS, the intensity of the 370 nm peak started to decrease and that of a new peak at approximately 400 nm, which could be ascribed to the CsI -PbI_2-MACl intermediate state, started to increase as the amount of used MACl was increased. Furthermore, the thermogravimetric analysis (TGA) results of the control and target revealed that the sublimation of DMAI started at 90 °C for the control sample, and volatile products, such as residual IPA and MACl, in the target sample started to evaporate at approximately 54 °C **(Fig. 4.7B)**. Moreover, we noticed that the total weights of the control and target decreased by 0.5% at 128 and 181 °C, respectively. These results indicated that the sublimation of DMAI was facilitated by the addition of MACl. Furthermore, these results suggested that the SDMS accelerated the crystallization process, which represents the transition from the intermediate to the final $CsPbI_3$ phase. This phenomenon was also observed when the colour of the coated $CsPbI_3$/xMACl films changed during their heat treatment at 210 °C **(Fig. 4.8)**.

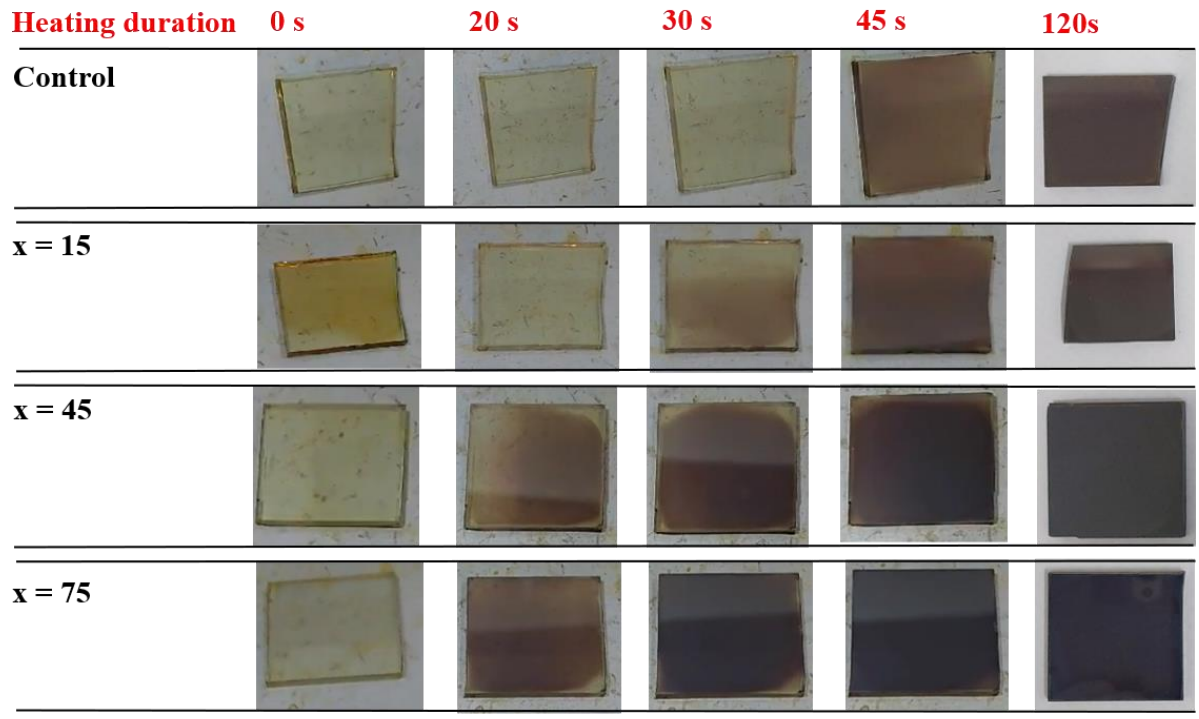

Fig. 4.8 Photographic images of substrates during heat treatment at 210 °C for $CsPbI_3$/xMACl (x= 15, 45, and 75 mM) and the control.

As the control film started to crystallize, its color changed from clear to black after 45 s. As observed, the control film started to crystallize by turning from clear to black after 45 s. Moreover, the rate of crystallization of the $CsPbI_3$/xMACl films increased with increasing amount of MACl, as follows: crystallization began at 30 s for the $CsPbI_3$/15MACl film and after less than 20 s for the $CsPbI_3$/45MACl and $CsPbI_3$/75MACl films. We believe that the fast crystallization of perovskite films could facilitate the formation of uniform and pinhole-less surface morphologies by reducing the exposure of the films to defect-inducing factors such as O_2 or humidity. To elucidate the intermediate phase-induced crystallization, we compared the Fourier-transform infrared (FT-IR) and ^{1}H nuclear magnetic resonance (^{1}H-NMR) spectra of the control and target samples. The N–H stretching, N–H bending, and C–H bending modes were distinctly observed in the FT-IR spectra of both samples **(Fig. 4.7C)** and confirmed the coordination of the DMA^+ ions in the intermediate state. By comparing the FT-IR spectra of the annealed perovskite layer (dotted line) with the solid line, we confirmed that the final $CsPbI_3$ layer was formed via the sublimation of DMA^+ in the intermediate state. On analyzing the N–H stretching mode, we determined that the typical N–H stretching peak of DMAI at 3480 cm^{-1},[89] has shifted to 3438 and 3448 cm^{-1} for the control and target samples, respectively. The increase in the wavenumber of the N–H stretching mode after the MACl treatment indicates that the stretching mode of N–H became stronger as the interactions between DMA^+ and PbI_3^- weakened. The interference of the interactions at the intermediate state and resulting weakened coordination attributed to the MACl treatment were further confirmed using ^{1}H-NMR analyses **(Fig. 4.7D)**. The ^{1}H-NMR signal of the resonance of protons around the N atoms shifted from 8.14 to 8.00 ppm and broadened after the SDMS.[90] This up-field shift could be attributed to the formation of the new intermediate phase by the introduction of MACl, which weakened the interactions between DMA^+ and PbI_3^- and induced the higher electron density of the N-adjacent protons. Therefore, the experimental results indicated that the SDMS accelerated the sublimation of DMAI by interrupting the coordination of the intermediate state. This resulted in simultaneous and fast crystallization, thereby leading to an improvement in the morphology of the perovskite layers.

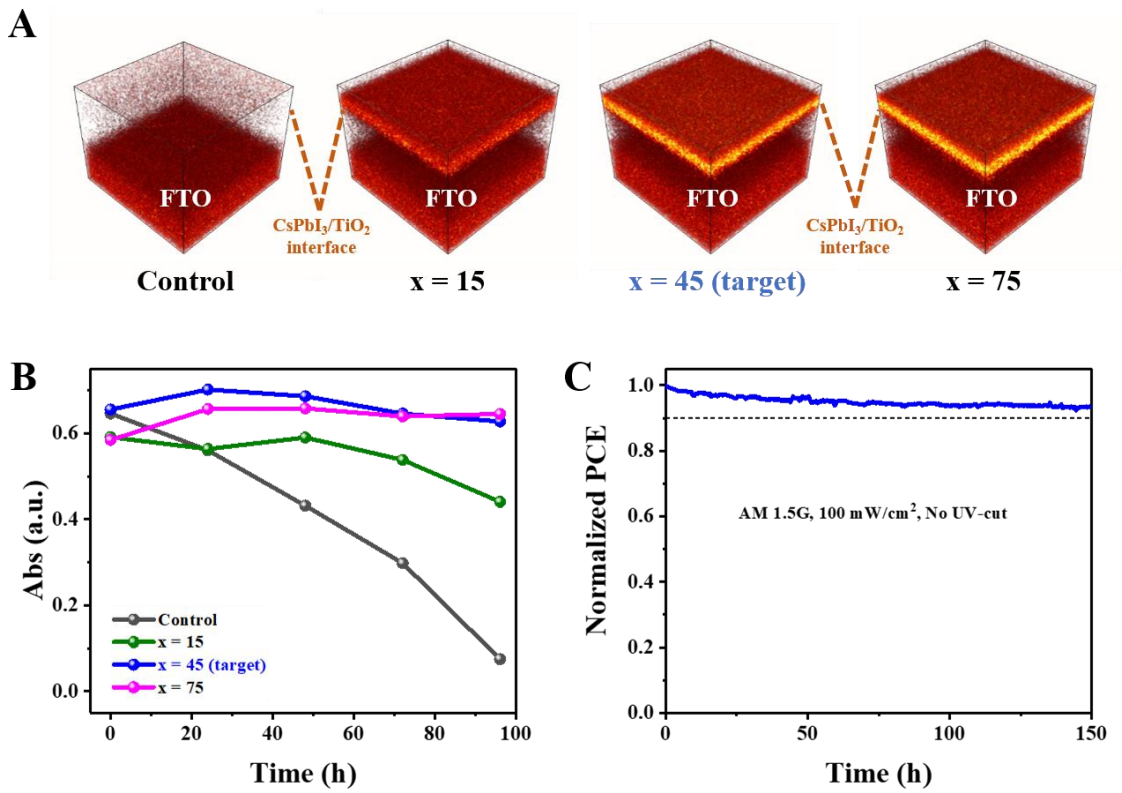

Fig. 4.9 Stability tests. **(A)** ToF-SIMS targeting Cl^- within FTO/bl-TiO_2/perovskite of $CsPbI_3$/xMACl (x= 15, 45, and 75 mM) and the control. **(B)** UV-vis absorbance at 600 nm as a function of exposure time in 20-30 RH% at 85 °C of $CsPbI_3$/xMACl (x= 15, 45, and 75 mM) and the control. **(C)** Maximum power point measured with the encapsulated target device under continuous full solar illumination (at 100 mW cm^{-2} without UV-cut) at ambient air.

Moreover, we investigated whether residual Cl^- ions were present in the perovskite layer using time-of-flight secondary ion mass spectrometry (ToF-SIMS), even though MACl is known to be volatile and evaporated after annealing even at relatively low temperatures.[91] The Cl^- ions are presented in yellow in the TOF-SIMS profiles of the $CsPbI_3$ layers deposited on c-TiO_2 substrates **(Fig. 4.9A)**. The presence of Cl^- was not observed in the ToF-SIMS profile of the control sample but was detected in the TOF-SIMS profiles of the $CsPbI_3$/xMACl films. The amount of residual Cl^- ions appeared to be proportional to x with saturation at $x \geq 45$, and the Cl^- ions were mainly present at the perovskite/TiO_2 interface. These Cl^- ions remaining at the perovskite/TiO_2 interface are expected to contribute to the surface passivation of the perovskite

The phase stability of the perovskite films was analyzed by measuring their absorbance at 600 nm as a function of the exposure time under 20–30% RH at 85 °C (without encapsulation), and the results are presented in **Fig 4.7B**. The absorbance of the control sample decreased significantly with increasing

exposure time; however, only a minor decrease in the absorbance of the $CsPbI_3$/15MACl sample was observed after 72 h. In contrast, the absorbances of the target and $CsPbI_3$/75MACl samples did not change even after 96 h of exposure. These data indicate that the residual Cl^- ion content strongly affected the stability of $CsPbI_3$. We also tested the long-term operational stability of the encapsulated devices under continuous light irradiation at the MPP under ambient conditions (100 mW cm^{-2} without UV-cut). The PSC featuring the target film presented fine operational stability and maintained over 90% of its initial PCE over 150 h of irradiation **(Fig. 4C)**.

4.3 Conclusion

We improved the morphology of $CsPbI_3$ perovskite films by controlling the intermediate state via SDMS. MACl facilitated the removal of DMAI from the intermediate phase, which allowed the fast crystallization of the $CsPbI_3$ perovskite. An intermediate phase-induced crystallization mechanism for improving the surface morphology of $CsPbI_3$ was proposed. The effect combined with optimal SDMS and OAI passivation allowed us to fabricate $CsPbI_3$-based PSCs, which exhibited excellent and stabilized PCEs of 20.37% and 19.5%, respectively. Furthermore, the presence of residual Cl^- ions in the perovskite films improved the stability of $CsPbI_3$. We believe that these strategies to improve the surface morphology and long-term stability of perovskites could be widely used for the construction of $CsPbI_3$-based PSCs and Si tandem solar cells in the future.

Chapter 5. Summary, Future Perspectives and References

5.1 Summary

(i) In terms of perovskite precursor solution, elemental sulfur stabilized the solution by coordination with the MA cation inhibiting the deprotonation of MA ion.

(ii) For highly efficient PSCs, phase stabilizer that minimize the change in inherent bandgap of α-$FAPbI_3$ was investigated.

(ii-1) By doping $MDACl_2$, the bandgap of α-$FAPbI_3$ was fully utilized to obtain a J_{sc} of over 26 mA cm^{-2} (certified PCE: 23.7%)

(ii-2) By incorporating Cs^+ into MDA-doped $FAPbI_3$, micro-strain was relaxed to reduce defects resulting in a certified PCE of 24.37%

(iii) The morphology of $CsPbI_3$, which is a wide-bandgap perovskite that can be used as top-cell of tandem device, has been improved via MACl post-treatment achieving an efficiency of over 20%.

5.2 Future perspectives

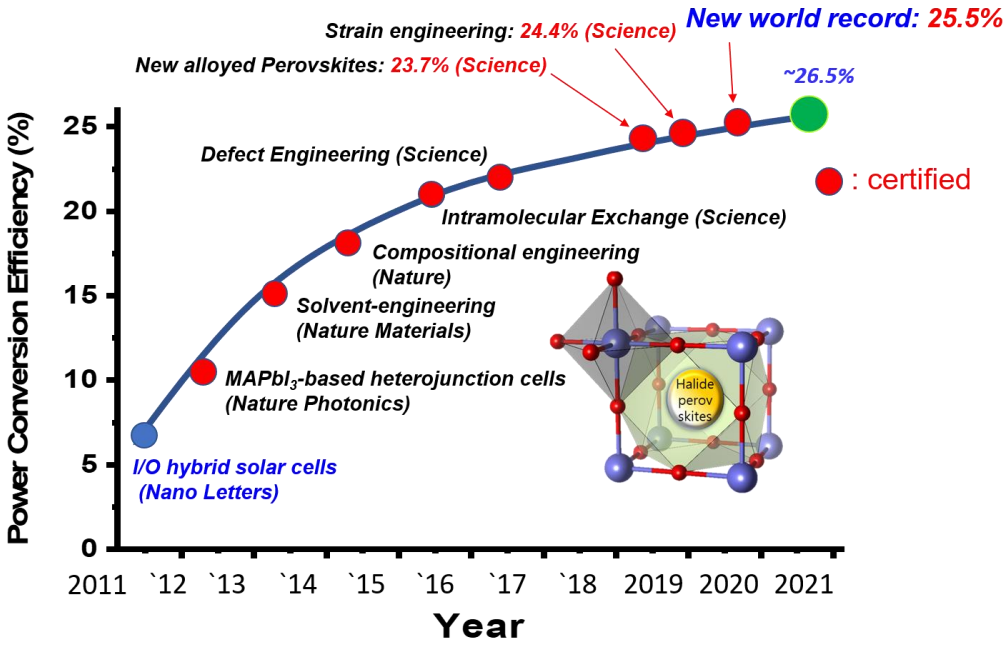

Fig. 5.1 Schematic diagram of the increase in PSCs efficiency achieved by our group (Prof. Sang Il Seok group at UNIST).

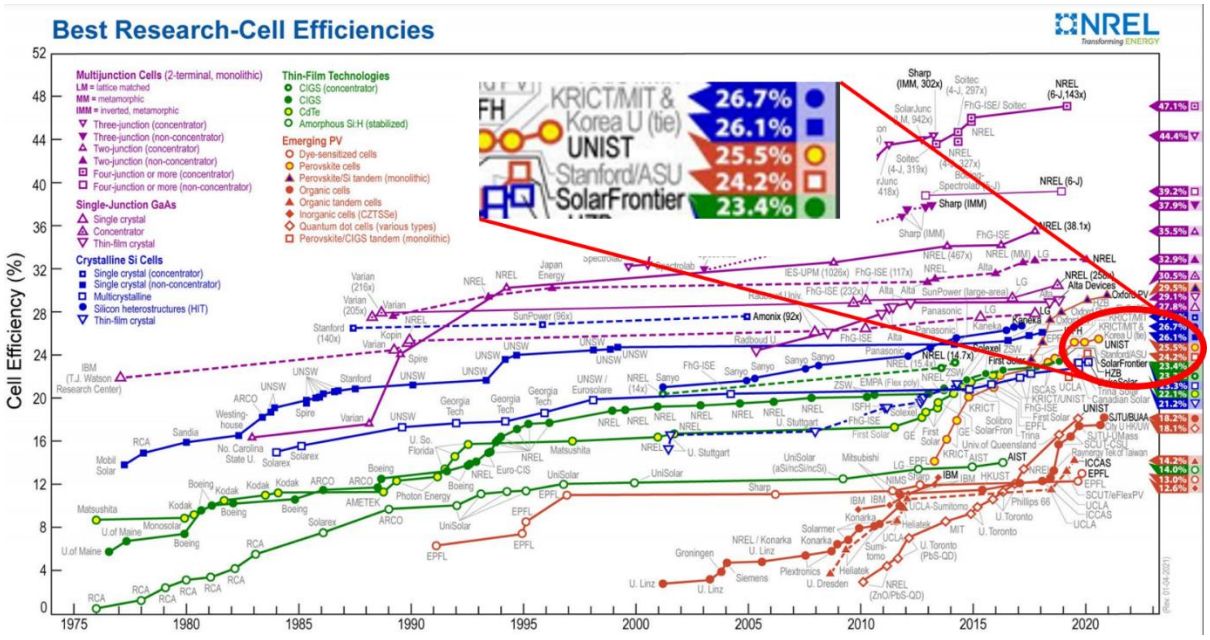

Fig. 5.2 National Renewable Energy Laboratory (NREL) chart for the best research-cell efficiencies (reviewed 04. Jan, 2021).

Our group is one of the pioneers of PSCs and have contributed greatly to the development of PSCs technologies and reported our results to high impact journals many times **(Fig. 5.1)**. Furthermore, one of my manuscript under evaluation is about the efficiency of 25.5% single-junction PSCs which is currently included in the prestigious NREL chart for the record efficiency **(Fig. 5.2)**. I believe that PSCs can achieve over 26% of efficiency which is higher than efficiency of single crystalline silicon solar cells in near future.

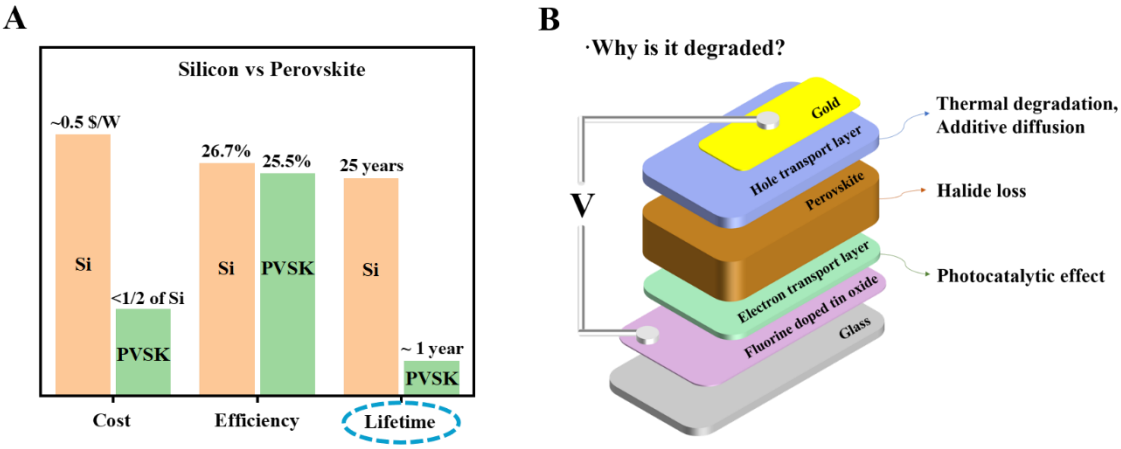

Fig. 5.3 (A) Cost, efficiency, and lifetime comparison of silicon (Si) and perovskite (PVSK) solar cells. **(B)** Schematic diagram of a perovskite solar cell and possible degradation inducing factors.

However, PSCs lack stability, which is one of the most important factors for commercialization, compared to silicon **(Fig. 5.3A)**. While the lifetime of silicon solar cells is about 25 years, PSCs have not yet demonstrated a lifetime of more than one year. Highly efficient PSCs (>23% PCE) demonstrate less than 1000 h of operational stability.[23, 51, 92] Improvements to stability are thus critical for the commercialization of flexible and inexpensive PSCs to contribute to solar energy deployment goals.

There are several factors that limit the stability of the multi-layered perovskite solar cell **(Fig. 5.3B)**. **(i) Photocatalytic effect of electron transport layer (ETL):** Titanium dioxide (TiO_2) has been widely used as an ETL for efficient PSCs.[32, 35, 51, 92] However, TiO_2 is a typical photocatalyst material with high photoactivity property. Thus, under continuous solar illumination, it can degrade perovskite layer. To replace TiO_2, many metal oxide ETL candidates are studied such as SnO_2,[22] Zn_2SnO_4,[93] La-$BaSnO_3$,[94] and ZnO.[95] However, other metal oxide-based PSCs show relatively lower efficiency. For efficient PSCs with long-term photostability, we must develop methods to suppress the photocatalytic effect of TiO_2 or improve other ETL-based PSCs performances. **(ii) Halide diffusion of perovskite:** Efficient PSCs are mainly fabricated with iodide(I^-)-based perovskite materials with broader solar-light

absorption through narrower bandgaps. However, iodide can be released from the perovskite and escape the device, forming mobile halide vacancies and defects.[96] These halide defects form deep traps, inducing nonradiative recombination which significantly reduce the photovoltaic performance over time. To suppress halide vacancies, binding energy of perovskite material should be increased by compositional modification or interface of the perovskite layer should be modified. **(iii) Thermal degradation and additive diffusion of hole transport layer (HTL):** 2,2',7,7'- tetrakis[N,N-di(4-methoxyphenyl)amino]- 9,9'-spirobifluorene (Spiro-OMeTAD) is commonly used as HTL for efficient PSCs. However, it is thermally unstable with low glass transition temperature (T_g) of approximately 120 °C. Furthermore, it needs many additives to increase hole conductivity. To solve this issue, other HTL candidates such as CuSCN [97] and copper phthalocyanine (CuPc) [98] or additive-free HTL have been studied, but the performance is still significantly low. This is mainly due to energy mismatch between the perovskite and HTL, which can be improved via interface engineering. Perovskite/HTL interface modification can improve the efficiency and stability by surface passivating the perovskite layer and suppressing additive diffusion and acting as electron blocking layer.

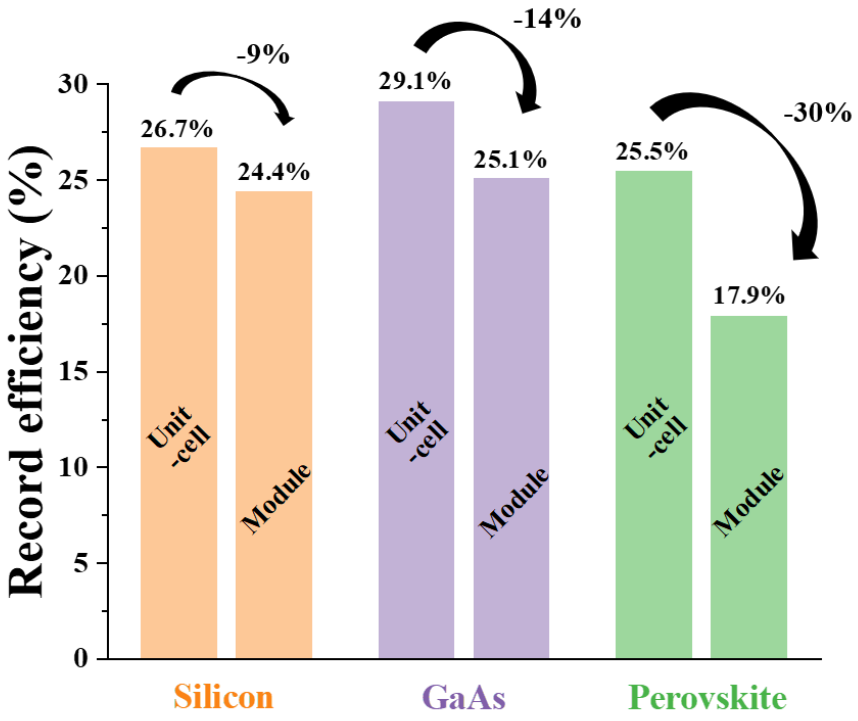

Fig. 5.4 A comparison of record unit-cell and module efficiencies of silicon, GaAs, perovskite solar cells.

In general, perovskite layer in high-performance PSCs is deposited by so-called anti-solvent method to make dense and uniform surface. However, it cannot be adopted to large-area solar cells which afforded in real application. Thus, PSCs shows significant decreases in module device compared to unit-cell **(Fig. 5.4)**.

To commercialize PSCs, such problems must be solved. First, when long-term stability is secured and it is modularized, that is, a large area, the decrease in efficiency should not appear significantly. If so, since PSCs have many advantages over silicon solar cells, it is expected that various used and commercialization as next-generation solar cells will be possible in the future.

5.3 References

1. Richard Perez, M. P., A fundamental look at supply side energy reserves for the planet. *IEA/SHC Solar Update* **2009,** *62*, 4-6.
2. https://ourworldindata.org/energy.
3. https://www.irena.org/publications/2020/Jun/Renewable-Power-Costs-in-2019.
4. https://www.nrel.gov/pv/cell-efficiency.html.
5. Radicchi, E.; Mosconi, E.; Elisei, F.; Nunzi, F.; De Angelis, F., Understanding the Solution Chemistry of Lead Halide Perovskites Precursors. *ACS Applied Energy Materials* **2019,** *2* (5), 3400-3409.
6. Boonmongkolras, P.; Kim, D.; Alhabshi, Esra M.; Gereige, I.; Shin, B., Understanding effects of precursor solution aging in triple cation lead perovskite. *RSC Advances* **2018,** *8* (38), 21551-21557.
7. Dou, B.; Wheeler, L. M.; Christians, J. A.; Moore, D. T.; Harvey, S. P.; Berry, J. J.; Barnes, F. S.; Shaheen, S. E.; van Hest, M. F. A. M., Degradation of Highly Alloyed Metal Halide Perovskite Precursor Inks: Mechanism and Storage Solutions. *ACS Energy Letters* **2018,** *3* (4), 979-985.
8. Nayak, P. K.; Moore, D. T.; Wenger, B.; Nayak, S.; Haghighirad, A. A.; Fineberg, A.; Noel, N. K.; Reid, O. G.; Rumbles, G.; Kukura, P.; Vincent, K. A.; Snaith, H. J., Mechanism for rapid growth of organic–inorganic halide perovskite crystals. *Nature Communications* **2016,** *7* (1), 13303.
9. Noel, N. K.; Habisreutinger, S. N.; Wenger, B.; Klug, M. T.; Hörantner, M. T.; Johnston, M. B.; Nicholas, R. J.; Moore, D. T.; Snaith, H. J., A low viscosity, low boiling point, clean solvent system for the rapid crystallisation of highly specular perovskite films. *Energy & Environmental Science* **2017,** *10* (1), 145-152.
10. Meyer, B., Elemental sulfur. *Chemical Reviews* **1976,** *76* (3), 367-388.
11. Han, D.-H.; Kim, B.-S.; Choi, S.-J.; Jung, Y.; Kwak, J.; Park, S.-M., Time-Resolved In Situ Spectroelectrochemical Study on Reduction of Sulfur in N,N[sup ′]-Dimethylformamide. *Journal of The Electrochemical Society* **2004,** *151* (9), E283.
12. Kim, B. S.; Park, S. M., In Situ Spectroelectrochemical Studies on the Reduction of Sulfur in Dimethyl Sulfoxide Solutions. *Journal of The Electrochemical Society* **1993,** *140* (1), 115-122.
13. Davis, R. E.; Nakshbendi, H. F., Sulfur in Amine Solvents. *Journal of the American Chemical Society* **1962,** *84* (11), 2085-2090.
14. Wang, C.; Chen, H.; Dong, W.; Ge, J.; Lu, W.; Wu, X.; Guo, L.; Chen, L., Sulfur–amine chemistry-based synthesis of multi-walled carbon nanotube–sulfur composites for high performance Li–S batteries. *Chemical Communications* **2014,** *50* (10), 1202-1204.
15. Thomson, J. W.; Nagashima, K.; Macdonald, P. M.; Ozin, G. A., From Sulfur−Amine Solutions to Metal Sulfide Nanocrystals: Peering into the Oleylamine−Sulfur Black Box. *Journal of the American Chemical Society* **2011,** *133* (13), 5036-5041.
16. Qin, M.; Cao, J.; Zhang, T.; Mai, J.; Lau, T.-K.; Zhou, S.; Zhou, Y.; Wang, J.; Hsu, Y.-J.; Zhao, N.; Xu, J.; Zhan, X.; Lu, X., Fused-Ring Electron Acceptor ITIC-Th: A Novel Stabilizer for Halide Perovskite Precursor Solution. **2018,** *8* (18), 1703399.
17. Kojima, A.; Teshima, K.; Shirai, Y.; Miyasaka, T., Organometal Halide Perovskites as Visible-Light Sensitizers for Photovoltaic Cells. *Journal of the American Chemical Society* **2009,** *131* (17), 6050-6051.
18. Kim, H.-S.; Lee, C.-R.; Im, J.-H.; Lee, K.-B.; Moehl, T.; Marchioro, A.; Moon, S.-J.; Humphry-Baker, R.; Yum, J.-H.; Moser, J. E.; Grätzel, M.; Park, N.-G., Lead Iodide Perovskite Sensitized All-Solid-State Submicron Thin Film Mesoscopic Solar Cell with Efficiency Exceeding 9%. *Scientific Reports* **2012,** *2* (1), 591.
19. Jeon, N. J.; Noh, J. H.; Kim, Y. C.; Yang, W. S.; Ryu, S.; Seok, S. I., Solvent engineering for high-performance inorganic–organic hybrid perovskite solar cells. *Nature Materials*

2014, *13* (9), 897-903.
20. Jeon, N. J.; Noh, J. H.; Yang, W. S.; Kim, Y. C.; Ryu, S.; Seo, J.; Seok, S. I., Compositional engineering of perovskite materials for high-performance solar cells. *Nature* **2015,** *517* (7535), 476-480.
21. Yang, W. S.; Noh, J. H.; Jeon, N. J.; Kim, Y. C.; Ryu, S.; Seo, J.; Seok, S. I., High-performance photovoltaic perovskite layers fabricated through intramolecular exchange. **2015,** *348* (6240), 1234-1237.
22. Jiang, Q.; Zhao, Y.; Zhang, X.; Yang, X.; Chen, Y.; Chu, Z.; Ye, Q.; Li, X.; Yin, Z.; You, J., Surface passivation of perovskite film for efficient solar cells. *Nature Photonics* **2019,** *13* (7), 460-466.
23. Yoo, J. J.; Seo, G.; Chua, M. R.; Park, T. G.; Lu, Y.; Rotermund, F.; Kim, Y.-K.; Moon, C. S.; Jeon, N. J.; Correa-Baena, J.-P.; Bulović, V.; Shin, S. S.; Bawendi, M. G.; Seo, J., Efficient perovskite solar cells via improved carrier management. *Nature* **2021,** *590* (7847), 587-593.
24. Shockley, W.; Queisser, H. J., Detailed Balance Limit of Efficiency of p-n Junction Solar Cells. **1961,** *32* (3), 510-519.
25. McMeekin, D. P.; Sadoughi, G.; Rehman, W.; Eperon, G. E.; Saliba, M.; Hörantner, M. T.; Haghighirad, A.; Sakai, N.; Korte, L.; Rech, B.; Johnston, M. B.; Herz, L. M.; Snaith, H. J., A mixed-cation lead mixed-halide perovskite absorber for tandem solar cells. **2016,** *351* (6269), 151-155.
26. Saliba, M.; Matsui, T.; Seo, J.-Y.; Domanski, K.; Correa-Baena, J.-P.; Nazeeruddin, M. K.; Zakeeruddin, S. M.; Tress, W.; Abate, A.; Hagfeldt, A.; Grätzel, M., Cesium-containing triple cation perovskite solar cells: improved stability, reproducibility and high efficiency. *Energy & Environmental Science* **2016,** *9* (6), 1989-1997.
27. Smecca, E.; Numata, Y.; Deretzis, I.; Pellegrino, G.; Boninelli, S.; Miyasaka, T.; La Magna, A.; Alberti, A., Stability of solution-processed MAPbI3 and FAPbI3 layers. *Physical Chemistry Chemical Physics* **2016,** *18* (19), 13413-13422.
28. Hoke, E. T.; Slotcavage, D. J.; Dohner, E. R.; Bowring, A. R.; Karunadasa, H. I.; McGehee, M. D., Reversible photo-induced trap formation in mixed-halide hybrid perovskites for photovoltaics. *Chemical Science* **2015,** *6* (1), 613-617.
29. Lee, J.-W.; Dai, Z.; Han, T.-H.; Choi, C.; Chang, S.-Y.; Lee, S.-J.; De Marco, N.; Zhao, H.; Sun, P.; Huang, Y.; Yang, Y., 2D perovskite stabilized phase-pure formamidinium perovskite solar cells. *Nature Communications* **2018,** *9* (1), 3021.
30. Fu, Y.; Wu, T.; Wang, J.; Zhai, J.; Shearer, M. J.; Zhao, Y.; Hamers, R. J.; Kan, E.; Deng, K.; Zhu, X. Y.; Jin, S., Stabilization of the Metastable Lead Iodide Perovskite Phase via Surface Functionalization. *Nano Letters* **2017,** *17* (7), 4405-4414.
31. Turren-Cruz, S.-H.; Hagfeldt, A.; Saliba, M., Methylammonium-free, high-performance, and stable perovskite solar cells on a planar architecture. **2018,** *362* (6413), 449-453.
32. Jung, E. H.; Jeon, N. J.; Park, E. Y.; Moon, C. S.; Shin, T. J.; Yang, T.-Y.; Noh, J. H.; Seo, J., Efficient, stable and scalable perovskite solar cells using poly(3-hexylthiophene). *Nature* **2019,** *567* (7749), 511-515.
33. Yoo, J. J.; Wieghold, S.; Sponseller, M. C.; Chua, M. R.; Bertram, S. N.; Hartono, N. T. P.; Tresback, J. S.; Hansen, E. C.; Correa-Baena, J.-P.; Bulović, V.; Buonassisi, T.; Shin, S. S.; Bawendi, M. G., An interface stabilized perovskite solar cell with high stabilized efficiency and low voltage loss. *Energy & Environmental Science* **2019,** *12* (7), 2192-2199.
34. Jeon, N. J.; Noh, J. H.; Yang, W. S.; Kim, Y. C.; Ryu, S.; Seo, J.; Seok, S. I., Compositional engineering of perovskite materials for high-performance solar cells. *Nature* **2015,** *517*, 476.
35. Jeon, N. J.; Na, H.; Jung, E. H.; Yang, T.-Y.; Lee, Y. G.; Kim, G.; Shin, H.-W.; Il Seok, S.; Lee, J.; Seo, J., A fluorene-terminated hole-transporting material for highly efficient and stable perovskite solar cells. *Nature Energy* **2018,** *3* (8), 682-689.
36. Li, Z.; Yang, M.; Park, J.-S.; Wei, S.-H.; Berry, J. J.; Zhu, K., Stabilizing Perovskite Structures by Tuning Tolerance Factor: Formation of Formamidinium and Cesium Lead Iodide Solid-

State Alloys. *Chemistry of Materials* **2016,** *28* (1), 284-292.
37. Binek, A.; Hanusch, F. C.; Docampo, P.; Bein, T., Stabilization of the Trigonal High-Temperature Phase of Formamidinium Lead Iodide. *The journal of physical chemistry letters* **2015,** *6* (7), 1249-53.
38. Kim, M.; Kim, G.-H.; Lee, T. K.; Choi, I. W.; Choi, H. W.; Jo, Y.; Yoon, Y. J.; Kim, J. W.; Lee, J.; Huh, D.; Lee, H.; Kwak, S. K.; Kim, J. Y.; Kim, D. S., Methylammonium Chloride Induces Intermediate Phase Stabilization for Efficient Perovskite Solar Cells. *Joule* **2019**.
39. Tan, H.; Jain, A.; Voznyy, O.; Lan, X.; García de Arquer, F. P.; Fan, J. Z.; Quintero-Bermudez, R.; Yuan, M.; Zhang, B.; Zhao, Y.; Fan, F.; Li, P.; Quan, L. N.; Zhao, Y.; Lu, Z.-H.; Yang, Z.; Hoogland, S.; Sargent, E. H., Efficient and stable solution-processed planar perovskite solar cells via contact passivation. **2017,** *355* (6326), 722-726.
40. Zheng, X.; Wu, C.; Jha, S. K.; Li, Z.; Zhu, K.; Priya, S., Improved Phase Stability of Formamidinium Lead Triiodide Perovskite by Strain Relaxation. *ACS Energy Letters* **2016,** *1* (5), 1014-1020.
41. Chen, Y.; Lei, Y.; Li, Y.; Yu, Y.; Cai, J.; Chiu, M.-H.; Rao, R.; Gu, Y.; Wang, C.; Choi, W.; Hu, H.; Wang, C.; Li, Y.; Song, J.; Zhang, J.; Qi, B.; Lin, M.; Zhang, Z.; Islam, A. E.; Maruyama, B.; Dayeh, S.; Li, L.-J.; Yang, K.; Lo, Y.-H.; Xu, S., Strain engineering and epitaxial stabilization of halide perovskites. *Nature* **2020,** *577* (7789), 209-215.
42. Nishimura, K.; Hirotani, D.; Kamarudin, M. A.; Shen, Q.; Toyoda, T.; Iikubo, S.; Minemoto, T.; Yoshino, K.; Hayase, S., Relationship between Lattice Strain and Efficiency for Sn-Perovskite Solar Cells. *ACS Applied Materials & Interfaces* **2019,** *11* (34), 31105-31110.
43. Saidaminov, M. I.; Kim, J.; Jain, A.; Quintero-Bermudez, R.; Tan, H.; Long, G.; Tan, F.; Johnston, A.; Zhao, Y.; Voznyy, O.; Sargent, E. H., Suppression of atomic vacancies via incorporation of isovalent small ions to increase the stability of halide perovskite solar cells in ambient air. *Nature Energy* **2018,** *3* (8), 648-654.
44. Jones, T. W.; Osherov, A.; Alsari, M.; Sponseller, M.; Duck, B. C.; Jung, Y.-K.; Settens, C.; Niroui, F.; Brenes, R.; Stan, C. V.; Li, Y.; Abdi-Jalebi, M.; Tamura, N.; Macdonald, J. E.; Burghammer, M.; Friend, R. H.; Bulović, V.; Walsh, A.; Wilson, G. J.; Lilliu, S.; Stranks, S. D., Lattice strain causes non-radiative losses in halide perovskites. *Energy & Environmental Science* **2019,** *12* (2), 596-606.
45. Zhao, J.; Deng, Y.; Wei, H.; Zheng, X.; Yu, Z.; Shao, Y.; Shield, J. E.; Huang, J., Strained hybrid perovskite thin films and their impact on the intrinsic stability of perovskite solar cells. **2017,** *3* (11), eaao5616.
46. Zhu, C.; Niu, X.; Fu, Y.; Li, N.; Hu, C.; Chen, Y.; He, X.; Na, G.; Liu, P.; Zai, H.; Ge, Y.; Lu, Y.; Ke, X.; Bai, Y.; Yang, S.; Chen, P.; Li, Y.; Sui, M.; Zhang, L.; Zhou, H.; Chen, Q., Strain engineering in perovskite solar cells and its impacts on carrier dynamics. *Nature Communications* **2019,** *10* (1), 815.
47. Xue, D.-J.; Hou, Y.; Liu, S.-C.; Wei, M.; Chen, B.; Huang, Z.; Li, Z.; Sun, B.; Proppe, A. H.; Dong, Y.; Saidaminov, M. I.; Kelley, S. O.; Hu, J.-S.; Sargent, E. H., Regulating strain in perovskite thin films through charge-transport layers. *Nature Communications* **2020,** *11* (1), 1514.
48. Tsai, H.; Asadpour, R.; Blancon, J.-C.; Stoumpos, C. C.; Durand, O.; Strzalka, J. W.; Chen, B.; Verduzco, R.; Ajayan, P. M.; Tretiak, S.; Even, J.; Alam, M. A.; Kanatzidis, M. G.; Nie, W.; Mohite, A. D., Light-induced lattice expansion leads to high-efficiency perovskite solar cells. **2018,** *360* (6384), 67-70.
49. Wang, H.; Zhu, C.; Liu, L.; Ma, S.; Liu, P.; Wu, J.; Shi, C.; Du, Q.; Hao, Y.; Xiang, S.; Chen, H.; Chen, P.; Bai, Y.; Zhou, H.; Li, Y.; Chen, Q., Interfacial Residual Stress Relaxation in Perovskite Solar Cells with Improved Stability. **2019,** *31* (48), 1904408.
50. Kapil, G.; Bessho, T.; Ng, C. H.; Hamada, K.; Pandey, M.; Kamarudin, M. A.; Hirotani, D.; Kinoshita, T.; Minemoto, T.; Shen, Q.; Toyoda, T.; Murakami, T. N.; Segawa, H.; Hayase, S., Strain Relaxation and Light Management in Tin–Lead Perovskite Solar Cells to Achieve High Efficiencies. *ACS Energy Letters* **2019,** *4* (8), 1991-1998.

51. Min, H.; Kim, M.; Lee, S.-U.; Kim, H.; Kim, G.; Choi, K.; Lee, J. H.; Seok, S. I., Efficient, stable solar cells by using inherent bandgap of α-phase formamidinium lead iodide. **2019,** *366* (6466), 749-753.
52. Jeon, N. J.; Noh, J. H.; Kim, Y. C.; Yang, W. S.; Ryu, S.; Seok, S. I., Solvent engineering for high-performance inorganic–organic hybrid perovskite solar cells. *Nature Materials* **2014,** *13*, 897.
53. Liao, J.-F.; Wu, W.-Q.; Zhong, J.-X.; Jiang, Y.; Wang, L.; Kuang, D.-B., Enhanced efficacy of defect passivation and charge extraction for efficient perovskite photovoltaics with a small open circuit voltage loss. *Journal of Materials Chemistry A* **2019,** *7* (15), 9025-9033.
54. Leijtens, T.; Eperon, G. E.; Barker, A. J.; Grancini, G.; Zhang, W.; Ball, J. M.; Kandada, A. R. S.; Snaith, H. J.; Petrozza, A., Carrier trapping and recombination: the role of defect physics in enhancing the open circuit voltage of metal halide perovskite solar cells. *Energy & Environmental Science* **2016,** *9* (11), 3472-3481.
55. Wang, J. T.-W.; Wang, Z.; Pathak, S.; Zhang, W.; deQuilettes, D. W.; Wisnivesky-Rocca-Rivarola, F.; Huang, J.; Nayak, P. K.; Patel, J. B.; Mohd Yusof, H. A.; Vaynzof, Y.; Zhu, R.; Ramirez, I.; Zhang, J.; Ducati, C.; Grovenor, C.; Johnston, M. B.; Ginger, D. S.; Nicholas, R. J.; Snaith, H. J., Efficient perovskite solar cells by metal ion doping. *Energy & Environmental Science* **2016,** *9* (9), 2892-2901.
56. Pelleg, J.; Elish, E.; Mogilyanski, D., Evaluation of average domain size and microstrain in a silicide film by the Williamson-Hall method. *Metallurgical and Materials Transactions A* **2005,** *36* (11), 3187-3194.
57. Gordillo, G.; Otálora, C. A.; Reinoso, M. A., Erratum: "Trap center study in hybrid organic-inorganic perovskite using thermally stimulated current (TSC) analysis" [J. Appl. Phys. 122, 075304 (2017)]. *Journal of Applied Physics* **2017,** *122* (17), 179902.
58. Hu, Y.; Hutter, E. M.; Rieder, P.; Grill, I.; Hanisch, J.; Aygüler, M. F.; Hufnagel, A. G.; Handloser, M.; Bein, T.; Hartschuh, A.; Tvingstedt, K.; Dyakonov, V.; Baumann, A.; Savenije, T. J.; Petrus, M. L.; Docampo, P., Understanding the Role of Cesium and Rubidium Additives in Perovskite Solar Cells: Trap States, Charge Transport, and Recombination. *Advanced Energy Materials* **2018,** *8* (16), 1703057.
59. Garlick, G. F. J.; Gibson, A. F., The Electron Trap Mechanism of Luminescence in Sulphide and Silicate Phosphors. *Proceedings of the Physical Society* **1948,** *60* (6), 574-590.
60. Eperon, G. E.; Leijtens, T.; Bush, K. A.; Prasanna, R.; Green, T.; Wang, J. T.-W.; McMeekin, D. P.; Volonakis, G.; Milot, R. L.; May, R.; Palmstrom, A.; Slotcavage, D. J.; Belisle, R. A.; Patel, J. B.; Parrott, E. S.; Sutton, R. J.; Ma, W.; Moghadam, F.; Conings, B.; Babayigit, A.; Boyen, H.-G.; Bent, S.; Giustino, F.; Herz, L. M.; Johnston, M. B.; McGehee, M. D.; Snaith, H. J., Perovskite-perovskite tandem photovoltaics with optimized band gaps. **2016,** *354* (6314), 861-865.
61. Hou, Y.; Aydin, E.; De Bastiani, M.; Xiao, C.; Isikgor, F. H.; Xue, D.-J.; Chen, B.; Chen, H.; Bahrami, B.; Chowdhury, A. H.; Johnston, A.; Baek, S.-W.; Huang, Z.; Wei, M.; Dong, Y.; Troughton, J.; Jalmood, R.; Mirabelli, A. J.; Allen, T. G.; Van Kerschaver, E.; Saidaminov, M. I.; Baran, D.; Qiao, Q.; Zhu, K.; De Wolf, S.; Sargent, E. H., Efficient tandem solar cells with solution-processed perovskite on textured crystalline silicon. **2020,** *367* (6482), 1135-1140.
62. Xu, J.; Boyd, C. C.; Yu, Z. J.; Palmstrom, A. F.; Witter, D. J.; Larson, B. W.; France, R. M.; Werner, J.; Harvey, S. P.; Wolf, E. J.; Weigand, W.; Manzoor, S.; van Hest, M. F. A. M.; Berry, J. J.; Luther, J. M.; Holman, Z. C.; McGehee, M. D., Triple-halide wide–band gap perovskites with suppressed phase segregation for efficient tandems. **2020,** *367* (6482), 1097-1104.
63. Liu, C.; Yang, Y.; Xia, X.; Ding, Y.; Arain, Z.; An, S.; Liu, X.; Cristina, R. C.; Dai, S.; Nazeeruddin, M. K., Soft Template-Controlled Growth of High-Quality CsPbI3 Films for Efficient and Stable Solar Cells. **2020,** *10* (9), 1903751.
64. Draguta, S.; Sharia, O.; Yoon, S. J.; Brennan, M. C.; Morozov, Y. V.; Manser, J. M.; Kamat, P. V.; Schneider, W. F.; Kuno, M., Rationalizing the light-induced phase separation of mixed

halide organic-inorganic perovskites. *Nature Communications* **2017,** *8* (1).
65. Kim, D.; Jung, H. J.; Park, I. J.; Larson, B. W.; Dunfield, S. P.; Xiao, C.; Kim, J.; Tong, J.; Boonmongkolras, P.; Ji, S. G.; Zhang, F.; Pae, S. R.; Kim, M.; Kang, S. B.; Dravid, V.; Berry, J. J.; Kim, J. Y.; Zhu, K.; Kim, D. H.; Shin, B., Efficient, stable silicon tandem cells enabled by anion-engineered wide-bandgap perovskites. **2020,** *368* (6487), 155-160.
66. Xu, J.; Boyd, C. C.; Yu, Z. J.; Palmstrom, A. F.; Witter, D. J.; Larson, B. W.; France, R. M.; Werner, J.; Harvey, S. P.; Wolf, E. J.; Weigand, W.; Manzoor, S.; van Hest, M. F. A. M.; Berry, J. J.; Luther, J. M.; Holman, Z. C.; McGehee, M. D., Triple-halide wide–band gap perovskites with suppressed phase segregation for efficient tandems. *Science* **2020,** *367* (6482), 1097-1104.
67. Sutton, R. J.; Filip, M. R.; Haghighirad, A. A.; Sakai, N.; Wenger, B.; Giustino, F.; Snaith, H. J., Cubic or Orthorhombic? Revealing the Crystal Structure of Metastable Black-Phase CsPbI3 by Theory and Experiment. *ACS Energy Letters* **2018,** *3* (8), 1787-1794.
68. Marronnier, A.; Roma, G.; Boyer-Richard, S.; Pedesseau, L.; Jancu, J.-M.; Bonnassieux, Y.; Katan, C.; Stoumpos, C. C.; Kanatzidis, M. G.; Even, J., Anharmonicity and Disorder in the Black Phases of Cesium Lead Iodide Used for Stable Inorganic Perovskite Solar Cells. *ACS Nano* **2018,** *12* (4), 3477-3486.
69. Wang, Y.; Dar, M. I.; Ono, L. K.; Zhang, T.; Kan, M.; Li, Y.; Zhang, L.; Wang, X.; Yang, Y.; Gao, X.; Qi, Y.; Grätzel, M.; Zhao, Y., Thermodynamically stabilized β-CsPbI₃–based perovskite solar cells with efficiencies >18%. **2019,** *365* (6453), 591-595.
70. Wang, Y.; Liu, X.; Zhang, T.; Wang, X.; Kan, M.; Shi, J.; Zhao, Y., The Role of Dimethylammonium Iodide in CsPbI3 Perovskite Fabrication: Additive or Dopant? **2019,** *58* (46), 16691-16696.
71. Salim, T.; Sun, S.; Abe, Y.; Krishna, A.; Grimsdale, A. C.; Lam, Y. M., Perovskite-based solar cells: impact of morphology and device architecture on device performance. *Journal of Materials Chemistry A* **2015,** *3* (17), 8943-8969.
72. McMeekin, D. P.; Wang, Z.; Rehman, W.; Pulvirenti, F.; Patel, J. B.; Noel, N. K.; Johnston, M. B.; Marder, S. R.; Herz, L. M.; Snaith, H. J., Crystallization Kinetics and Morphology Control of Formamidinium–Cesium Mixed-Cation Lead Mixed-Halide Perovskite via Tunability of the Colloidal Precursor Solution. **2017,** *29* (29), 1607039.
73. Moot, T.; Marshall, A. R.; Wheeler, L. M.; Habisreutinger, S. N.; Schloemer, T. H.; Boyd, C. C.; Dikova, D. R.; Pach, G. F.; Hazarika, A.; McGehee, M. D.; Snaith, H. J.; Luther, J. M., CsI-Antisolvent Adduct Formation in All-Inorganic Metal Halide Perovskites. **2020,** *10* (9), 1903365.
74. Huang, J.; Wang, M.; Ding, L.; Yang, Z.; Zhang, K., Hydrobromic acid assisted crystallization of MAPbI3−xClx for enhanced power conversion efficiency in perovskite solar cells. *RSC Advances* **2016,** *6* (61), 55720-55725.
75. Heo, J. H.; Song, D. H.; Han, H. J.; Kim, S. Y.; Kim, J. H.; Kim, D.; Shin, H. W.; Ahn, T. K.; Wolf, C.; Lee, T.-W.; Im, S. H., Planar CH3NH3PbI3 Perovskite Solar Cells with Constant 17.2% Average Power Conversion Efficiency Irrespective of the Scan Rate. **2015,** *27* (22), 3424-3430.
76. Chang, C.-Y.; Chu, C.-Y.; Huang, Y.-C.; Huang, C.-W.; Chang, S.-Y.; Chen, C.-A.; Chao, C.-Y.; Su, W.-F., Tuning Perovskite Morphology by Polymer Additive for High Efficiency Solar Cell. *ACS Applied Materials & Interfaces* **2015,** *7* (8), 4955-4961.
77. Zhao, Y.; Wei, J.; Li, H.; Yan, Y.; Zhou, W.; Yu, D.; Zhao, Q., A polymer scaffold for self-healing perovskite solar cells. *Nature Communications* **2016,** *7*.
78. Boopathi, K. M.; Mohan, R.; Huang, T.-Y.; Budiawan, W.; Lin, M.-Y.; Lee, C.-H.; Ho, K.-C.; Chu, C.-W., Synergistic improvements in stability and performance of lead iodide perovskite solar cells incorporating salt additives. *Journal of Materials Chemistry A* **2016,** *4* (5), 1591-1597.
79. Zhao, Y.; Zhu, K., CH3NH3Cl-Assisted One-Step Solution Growth of CH3NH3PbI3: Structure, Charge-Carrier Dynamics, and Photovoltaic Properties of Perovskite Solar Cells. *The Journal*

of Physical Chemistry C **2014,** *118* (18), 9412-9418.
80. Dong, Q.; Yuan, Y.; Shao, Y.; Fang, Y.; Wang, Q.; Huang, J., Abnormal crystal growth in CH3NH3PbI3-xClx using a multi-cycle solution coating process. *Energy and Environmental Science* **2015,** *8* (8), 2464-2470.
81. Xie, F.; Chen, C.-C.; Wu, Y.; Li, X.; Cai, M.; Liu, X.; Yang, X.; Han, L., Vertical recrystallization for highly efficient and stable formamidinium-based inverted-structure perovskite solar cells. *Energy & Environmental Science* **2017,** *10* (9), 1942-1949.
82. Wang, M.; Li, B.; Siffalovic, P.; Chen, L. C.; Cao, G.; Tian, J., Monolayer-like hybrid halide perovskite films prepared by additive engineering without antisolvents for solar cells. *Journal of Materials Chemistry A* **2018,** *6* (31), 15386-15394.
83. Xu, X.; Li, Z.; Zhu, L.; Zheng, H.; Liu, G.; Hayat, T.; Alsaedi, A.; Zhang, X.; Huang, Y.; Pan, X., Large-grained formamidinium-based films via a 2D–3D conversion mechanism for high-performance perovskite solar cells without anti-solvent. *Journal of Materials Chemistry A* **2019,** *7* (3), 1341-1348.
84. Kim, H.; Lee, S.-U.; Lee, D. Y.; Paik, M. J.; Na, H.; Lee, J.; Seok, S. I., Optimal Interfacial Engineering with Different Length of Alkylammonium Halide for Efficient and Stable Perovskite Solar Cells. **2019,** *9* (47), 1902740.
85. Li, B.; Zhang, Y.; Fu, L.; Yu, T.; Zhou, S.; Zhang, L.; Yin, L., Surface passivation engineering strategy to fully-inorganic cubic CsPbI3 perovskites for high-performance solar cells. *Nature Communications* **2018,** *9* (1).
86. Eperon, G. E.; Paternò, G. M.; Sutton, R. J.; Zampetti, A.; Haghighirad, A. A.; Cacialli, F.; Snaith, H. J., Inorganic caesium lead iodide perovskite solar cells. *Journal of Materials Chemistry A* **2015,** *3* (39), 19688-19695.
87. Xiang, S.; Fu, Z.; Li, W.; Wei, Y.; Liu, J.; Liu, H.; Zhu, L.; Zhang, R.; Chen, H., Highly Air-Stable Carbon-Based α-CsPbI3 Perovskite Solar Cells with a Broadened Optical Spectrum. *ACS Energy Letters* **2018,** *3* (8), 1824-1831.
88. Bian, H.; Wang, H.; Li, Z.; Zhou, F.; Xu, Y.; Zhang, H.; Wang, Q.; Ding, L.; Liu, S.; Jin, Z., Unveiling the Effects of Hydrolysis-Derived DMAI/DMAPbIx Intermediate Compound on the Performance of CsPbI3 Solar Cells. **2020,** *7* (9), 1902868.
89. Pei, Y.; Liu, Y.; Li, F.; Bai, S.; Jian, X.; Liu, M., Unveiling Property of Hydrolysis-Derived DMAPbI3 for Perovskite Devices: Composition Engineering, Defect Mitigation, and Stability Optimization. *iScience* **2019,** *15*, 165-172.
90. Bian, H.; Wang, H.; Li, Z.; Zhou, F.; Xu, Y.; Zhang, H.; Wang, Q.; Ding, L.; Liu, S.; Jin, Z., Unveiling the Effects of Hydrolysis-Derived DMAI/DMAPbIx Intermediate Compound on the Performance of CsPbI3 Solar Cells. *Advanced Science* **2020,** *7* (9), 1902868.
91. Kim, M.; Kim, G.-H.; Lee, T. K.; Choi, I. W.; Choi, H. W.; Jo, Y.; Yoon, Y. J.; Kim, J. W.; Lee, J.; Huh, D.; Lee, H.; Kwak, S. K.; Kim, J. Y.; Kim, D. S., Methylammonium Chloride Induces Intermediate Phase Stabilization for Efficient Perovskite Solar Cells. *Joule* **2019,** *3* (9), 2179-2192.
92. Kim, G.; Min, H.; Lee, K. S.; Lee, D. Y.; Yoon, S. M.; Seok, S. I., Impact of strain relaxation on performance of α-formamidinium lead iodide perovskite solar cells. **2020,** *370* (6512), 108-112.
93. Shin, S. S.; Yang, W. S.; Noh, J. H.; Suk, J. H.; Jeon, N. J.; Park, J. H.; Kim, J. S.; Seong, W. M.; Seok, S. I., High-performance flexible perovskite solar cells exploiting Zn2SnO4 prepared in solution below 100 °C. *Nature Communications* **2015,** *6* (1), 7410.
94. Shin, S. S.; Yeom, E. J.; Yang, W. S.; Hur, S.; Kim, M. G.; Im, J.; Seo, J.; Noh, J. H.; Seok, S. I., Colloidally prepared La-doped BaSnO₃ electrodes for efficient, photostable perovskite solar cells. **2017,** *356* (6334), 167-171.
95. Zhang, P.; Wu, J.; Zhang, T.; Wang, Y.; Liu, D.; Chen, H.; Ji, L.; Liu, C.; Ahmad, W.; Chen, Z. D.; Li, S., Perovskite Solar Cells with ZnO Electron-Transporting Materials. **2018,** *30* (3), 1703737.
96. Zhao, L.; Tian, H.; Silver, S. H.; Kahn, A.; Ren, T.-L.; Rand, B. P., Ultrasensitive

Heterojunctions of Graphene and 2D Perovskites Reveal Spontaneous Iodide Loss. *Joule* **2018,** *2* (10), 2133-2144.

97. Arora, N.; Dar, M. I.; Hinderhofer, A.; Pellet, N.; Schreiber, F.; Zakeeruddin, S. M.; Grätzel, M., Perovskite solar cells with CuSCN hole extraction layers yield stabilized efficiencies greater than 20%. **2017,** *358* (6364), 768-771.

98. Kim, Y. C.; Yang, T. Y.; Jeon, N. J.; Im, J.; Jang, S.; Shin, T. J.; Shin, H. W.; Kim, S.; Lee, E.; Kim, S.; Noh, J. H.; Seok, S. I.; Seo, J., Engineering interface structures between lead halide perovskite and copper phthalocyanine for efficient and stable perovskite solar cells. *Energy & Environmental Science* **2017,** *10* (10), 2109-2116.